2010

Investigating Fabrication Methods For Micro Single-Chamber Solid Oxide Fuel Cells

Man Yang
North Carolina Agricultural and Technical State University

INVESTIGATING FABRICATION METHODS FOR MICRO SINGLE-CHAMBER SOLID OXIDE FUEL CELLS

by

Man Yang

A dissertation submitted to the graduate faculty
in partial fulfillment of the requirements for the degree of
DOCTOR OF PHILOSOPHY

Department: Industrial and System Engineering
Major: Production Systems
Major Professor: Dr. Salil Desai

North Carolina A&T State University
Greensboro, North Carolina
2010

ABSTRACT

Yang, Man, INVESTIGATING FABRICATION METHODS FOR MICRO SINGLE-CHAMBER SOLID OXIDE FUEL CELLS. **(Major Advisor: Salil Desai)**, North Carolina Agricultural and Technical State University.

A Solid Oxide Fuel Cell (SOFC) is a green energy technology that offers a cleaner and efficient alternative to fossil fuels. The efficiency and utility of SOFCs can be enhanced by fabricating miniaturized component structures within the fuel cell footprint. This research focuses on the microfabrication of parallel-connected inter-digitized design of micro single chamber SOFC (μ-SC-SOFCs). In this dissertation, candidate micro/nano fabrication techniques to precisely fabricate micro patterns on planar substrates have been studied. These include EBL, soft lithography, photolithography, and direct-writing. After analyzing preliminary results, two combinational approaches were further investigated. The first method involves the combination of the photolithography and pulse laser deposition (PLD) process. The second method combines direct-writing technique with photolithography. The combination of direct-writing and photolithography is a novel method for fabricating micro SC-SOFC with multilayer electrolyte/electrode structures that will increase SOFC efficiency.

To understand and optimize the direct-write process, the cathode electrode slurry was investigated. In the initial research the effects of dispersant on LSCF slurry rheology was studied. Further, the effects of solid loading and binder concentrations on the cathode electrode dimensions, microstructure and resistance were evaluated. Finally, process

parameters for direct-writing technology (extrusion pressure, nozzle speed, stand-off distance) were studied.

School of Graduate Studies
North Carolina Agricultural and Technical State University

This is to certify that the Doctoral Dissertation of

Man Yang

has met the dissertation requirements of
North Carolina Agricultural and Technical State University

Greensboro, North Carolina
2010

Approved by:

Dr. Salil Desai Major Professor	Dr. Zhigang Xu Co-Advisor
Dr. Paul Stanfield Committee member Department Chairperson	Dr. Jagannathan Sankar Committee member
Dr. Zhichao Li Committee member	Dr. Alan Letton Interim Associate Vice Chancellor for Research and Graduate Dean

BIOGRAPHICAL SKETCH

Man Yang received her master's degree in Industrial Engineering at the University of Pittsburgh in Aug, 2007. She is the recipient (2 times) of the Wadaran L. Kennedy Scholar (4.0 GPA) Award from North Carolina A&T State University. In 2009 she received the "Outstanding Research Assistant" award from the Industrial and System Engineering Department. Since 2007, she is researching the fabrication of novel micro-nano size single chamber solid oxide fuel cells towards her doctoral degree.

ACKNOWLEDGEMENT

I owe my deepest gratitude to my advisor, Dr. Salil Desai, and co–advisor, Dr. Zhigang Xu, for their guidance, unwavering support, encouragement and above all their friendly attitude. In particular, Dr. Xu familiarized me with this research area and introduced me to several equipments. Without their guidance and persistent assistance this dissertation would not have been possible.

In addition, I would like to take this opportunity to express deep sense of gratitude to everyone who helped me during my dissertation. Specifically, Dr. Sergey N. Yarmolenko for guidance with the Zeiss microscope for profile imaging; Prof. Steve Oneyear for instruction with the use of CNN equipment for machining test samples; my group mate, Taye Esho, for data collection.

I would like to thank Dr. Jag Sankar, Director - Office of Naval Research and the Center for Advanced Materials and Smart Structures for facility and financial support towards this project. In addition, I am thankful to the Department of Industrial and Systems Engineering and specifically, Drs. Stanfield and Li for agreeing to serve on my Ph.D. committee.

Finally, words alone cannot express the thanks I owe to Feng Feng, my husband, for his encouragement and assistance.

TABLE OF CONTENTS

LIST OF FIGURES

FIGURES **PAGE**

LIST OF TABLES

TABLES **PAGE**

NOMENCLATURE

μ-SC-SOFCs	Micro - Single Chamber–Solid Oxide Fuel Cells
3D	Three Dimensions
AFC	Alkaline Fuel Cell
CGO	Gadolinia Doped Ceria
CNC	Computer Numerical Control
CP	Microcontact Printing
DSC	Differential Scanning Calorimetry
EBL	Electron Beam Lithography
EDS	Energy Disperse Spectrum
LSCF	La0.6Sr0.2Fe0.8Co0.2O3-δ
LSGM	Cobalt doped Lanthanum Gallate
LSM	Strontium Doped Lanthanum Manganite
MCFC	Molten Carbonate Fuel Cell
MEMS	Micro-electromechanical System
MIMIC	Micromolding in Capillaries
MS	Magnetron Sputtering
PAFC	Phosphoric Acid Fuel Cell
PDMS	Polydimethylsiloxane
PEMFC	Proton Exchange Membrane Fuel Cell

PLD	Pulse Laser Deposition
PMMA	Methyl Methacrylate
PVB	Polyvinyl Butyral
SDC	Samaria Doped Ceria
SEM	Scanning Electron Microscopy
SOFC	Solid Oxide Fuel Cell
TM	Microtransfer Molding
TGA	Thermo Gravimetric Analysis
VD	Vapor Deposition
XRD	X-ray Diffraction
YSZ	Yttria-Stabilized Zirconia

CHAPTER 1

Introduction

The dramatic technological advances coupled with global economic development, social progress, and rapid population growth has increased human demands for energy. As a result, the Earth's limited fossil energy resources have increasingly depleted. Independent studies have shown that based on the current rates of output, global oil reserves would last around 40 years, natural gas reserves for 65 years, and coal deposits some 200 years [1; 2]. Moreover, various problems arise during the oil production, transmission, and use, specifically, the global greenhouse effect. This has serious implications to human and animal life. It is estimated that the lack of alternative energy source will jeopardize human survival [1; 3].

Given the gravity of the situation, renewed efforts are in place for new alternative green energy. Green energy, green technology and green industries, etc. have become eminent topics in the 21st century. At present, there are various green ways to generate power, such as solar power, wind power, hydropower, nuclear power, etc. However, these power generation methods have different shortcomings or limitations. For instance, hydropower and wind power have constraints by topography. Thermal power has the problem of environmental pollution and greenhouse effect; solar energy meets the challenges on energy conversion, application, and storage technology; nuclear energy also has security concerns and nuclear waste disposal problem. In addition, these are

coupled with centralized power systems, long-distance transmission of electricity, which may also result in substantial loss of power. When these centralized power systems are non-operational, it can affect the electricity requirements of a huge number of households.

As a new generation of the green energy, fuel cells are gaining prominence. The idea of generating electricity through an electrochemical process was proposed by Sir William Grove in 1839 [4]. Grove was familiar with the principle of electrolysis whereby electrical energy can be used to split a water molecule into its constituents. Grove believed that it should be possible to reverse this electrolysis process, that is, reacting hydrogen with oxygen to generate electricity and water. This led to the invention of the gas battery cell. Grove's cell was considered to be only of academic interest. Later, toward the end of the nineteenth century, Ludwig Mond and Charles Langer [5] in 1889 researched gas batteries to increase efficiency. They came up with a cell consisting of platinum/gold foil electrodes with an unglazed earthenware electrolyte. They named this fuel cell [6].

As a green energy technology, fuel cells have the potential to use less fuel than competing technologies without or less pollution emissions. There are also many reasons why fuel cells might be useful in specific environments, such as the high quality of electricity generated or their quiet operation. In additions, fuel cells can be used as a distributed source. Unlike wind, hydropower or solar power, the power from fuel cells may not be transported for a long distance.

1.1. General Principle of Fuel Cell

A fuel cell is an electrochemical device that converts chemical energy directly into electrical energy. As long as the constant supply of fuel is provided, fuel cells are able to continue to output power. Typical fuels used are hydrogen, methanol, ethanol, natural gas or other hydrocarbons, the oxidant can be oxygen, and the by products are heat, water or less carbon dioxide [7].

In general, every fuel cell has three components, two electrodes, one positive (anode), one negative (cathode) and electrolyte. The reactions that produce electricity take place at the electrodes. Fuel, typically hydrogen H_2 is fed to and oxidized at the anode. Oxidant, typically air is fed to the cathode where the oxygen component is reduced and electrons travel in the external circuit from anode to cathode. The electrolyte between anode and cathode provides the electronic insulation and allows the conduction of ions. Electrolyte carries electrically charged particles (ions) from one electrode to the other and finally completes the circuit. Sometimes the catalyst is needed to accelerate the reactions at the electrodes. The overall reaction of a H_2/O_2 fuel cell can be written as follows [8]:

$$H_2 + \frac{1}{2}O_2 \rightarrow H_2O \tag{1.1}$$

1.2. Classification of Fuel Cell

According to the different types of the electrolytes, fuel cells can be categorized as alkaline fuel cell, phosphoric acid fuel cell, molten carbonate fuel cell, polymer

membrane (ionomer), proton exchange membrane fuel cell (PEMFC) , solid oxide fuel cell (SOFC) [9].

1) Alkaline fuel cell (AFC)

Alkaline fuel cells (AFC) are one of the most developed technologies and have been used since the mid-1960s by NASA in the Apollo and Space Shuttle programs. The fuel cells on board these spacecraft provide electrical power for on-board systems, as well as drinking water. AFCs are among the most efficient in generating electricity at nearly 70%.

Alkaline fuel cells use an electrolyte that is a water-based solution of potassium hydroxide (KOH) retained in a porous stabilized matrix. The concentration of KOH can be varied with the fuel cell operating temperature, which ranges from 65°C to 220°C. The charge carrier for an AFC is the hydroxyl ion (OH^-) that migrates from the cathode to the anode where they react with hydrogen to produce water and electrons. Water formed at the anode migrates back to the cathode to regenerate hydroxyl ions.

One characteristic of AFCs is that they are very sensitive to CO_2 that may be present in the fuel or air. The CO_2 reacts with the electrolyte, poisoning it rapidly, and severely degrading the fuel cell performance. AFC must be run on pure hydrogen and oxygen. Therefore, AFC are not being considered for automobile application.

2) Phosphoric acid fuel cell (PAFC)

Phosphoric acid fuel cells (PAFC) were the first fuel cells to be commercialized. Developed in the mid-1960s and field-tested since the 1970s, they have improved significantly in stability, performance, and cost. Such characteristics have made the

PAFC a good candidate for early stationary applications. The PAFC uses phosphoric acid (H_3PO_4) as an electrolyte. The ionic conductivity of phosphoric acid is low at low temperatures, so PAFCs are operated at the upper end of the range 150°C - 200°C.

The charge carrier is the hydrogen ion (H^+, proton). This is similar to the PEFC where the hydrogen introduced at the anode is split into its protons and electrons. The protons migrate through the electrolyte and combine with the oxygen, usually from air, at the cathode to form water. The electrons are routed through an external circuit where they can perform useful work. This set of reactions in the fuel cell produces electricity and the by-product is heat. The PAFC operates at greater than 40% efficiency in generating electricity. When operating in cogeneration applications, the overall efficiency is approximately 85%. In addition, CO_2 does not affect the electrolyte or cell performance and can therefore be easily operated with reformed fossil fuel.

3) Molten carbonate fuel cell (MCFC)

Molten carbonate fuel cells (MCFC) are in the class of high-temperature fuel cells. The operating temperature is about 650°C. This kind of fuel cell has high efficiency. The higher operating temperature allows them to use natural gas directly without the need for a fuel processor and have also been used with low-Btu fuel gas from industrial processes, other sources and fuels. Developed in the mid 1960s, improvements have been made in fabrication methods, performance, and endurance.

4) Proton Exchange Membrane Fuel Cell (PEMFC)

PEM fuel cells are believed to be the best type of fuel cells as a vehicular power source to eventually replace gasoline and diesel internal combustion engines. First used

in the 1960s for the NASA Gemini program, PEM fuel cells are currently being developed and demonstrated for systems ranging from 1W to 2kW. PEM fuel cells use a solid polymer membrane (a thin plastic film) as the electrolyte. This polymer is permeable to protons when it is saturated with water, but it does not conduct electrons.

The fuel for the PEMFC is hydrogen and the charge carrier is the hydrogen ion (proton). At the anode, the hydrogen molecule is split into hydrogen ions (protons) and electrons. The hydrogen ions permeate across the electrolyte to the cathode while the electrons flow through an external circuit and produce electric power. Oxygen, usually in the form of air, is supplied to the cathode and combines with the electrons and the hydrogen ions to produce water.

Compared to other types of fuel cells, PEM fuel cells generate more power for a given volume or weight of fuel cell. The standard equilibrium voltage of PEMFCs operating at 80°C is 1.17 V [8]. This high-power density characteristic makes them compact and lightweight. In addition, the operating temperature is less than 100°C, which allows rapid start-up. These traits and the ability to rapidly change power output are some of the characteristics that make the PEMFC the top candidate for automotive power applications.

Other advantages result from the electrolyte being a solid material. Compared to a liquid, the sealing of the anode and cathode gases is simpler with a solid electrolyte, and therefore, less expensive to manufacture. The solid electrolyte is also more immune to difficulties with orientation and has fewer problems with corrosion, compared to many of the other electrolytes, thus leading to a longer cell and stack life.

One of the disadvantages of the PEMFC for some applications is that the operating temperature is low. Temperatures near 100ºC are not high enough to perform useful cogeneration. In addition, since the electrolyte is required to be saturated with water to operate optimally, careful control of the moisture of the anode and cathode streams is important.

5) Solid Oxide Fuel Cell (SOFC)

Solid Oxide Fuel Cells are currently the highest-temperature fuel cells in development and can be operated over a wide temperature range from 600ºC-1000°C allowing a number of fuels to be used. For high temperature operations, the electrolyte is a solid ceramic material (solid oxide) that is conductive to oxygen ions (O^{2-}). The operating efficiency in generating electricity is among the highest of the fuel cells at about 60%. Furthermore, the high operating temperature allows cogeneration applications to create high-pressure steam that can be used in many applications. Figure1.1 shows the working principle of a SOFC. Electrochemical reactions occur simultaneously on both sides of the electrolyte. On the anode side, hydrogen is adsorbed and ionized; the electrons are removed by the connection to the electrical load where the electrical work is used. On the cathode side, oxygen is adsorbed and ionized by picking up the arriving electrons (1.2). The oxide ion travels through the electrolyte to the anode (1.3). Further the hydrogen ions (Protons) and the oxide ion form a molecule of water (1.4).

$$O_2 + 4e^- \rightarrow 2O^{2-} \quad (1.2)$$

$$H_2 \rightarrow 2H^+ + 2e^- \quad (1.3)$$

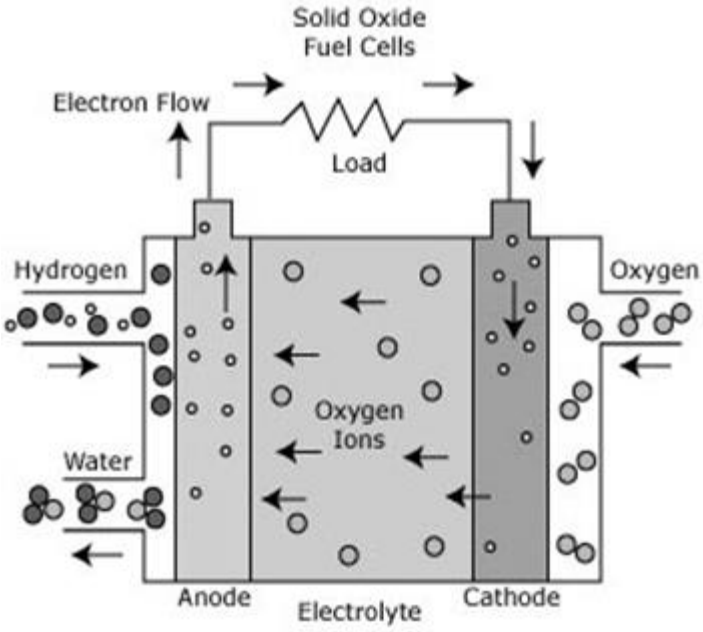

Figure 1.1. Electrochemistry of SOFC [1]

$$2H^{+} + \frac{1}{2}O^{2-} \rightarrow H_2O \qquad (1.4)$$

One advantage of SOFC is that hydrogen and carbon dioxide are used as fuel in the cell. This means that SOFC can use many common hydrocarbon fuels such as natural gas, diesel, gasoline and alcohol without the need to reform the fuel into pure hydrogen. In addition, SOFCs have a potentially lower cost due to the absence of precious metals, compared to PEMFC and PAFC which use platinum as a catalyst. Some other fuel cell types use liquid electrolytes, similar to battery acid, which can have a corrosive effect on components. Since SOFC use single piece solid-state ceramic cells, they are easier to maintain due to the lack of liquid based corrosion [10]. However, SOFC's system power

density is lower than PEMFC. Due to higher operating temperatures, the lead time to output power is longer. Moreover, the component's thermal stresses in may damage the fuel cell.

In general the underlying principle for the operation of fuel cell is the same, but each works differently based on the type of electrolyte used. The different types of electrolyte used for the different fuel cells, their operating temperatures, applications and their advantages and disadvantages are compared in Table 1.1.

1.3. Micro Fuel Cell

With the development of the micro-electromechanical systems (MEMS) and portable electronic devices, there is an emerging need for microelectrochemical energy conversion and storage devices such as batteries, fuel cells, and electrochemical capacitors. These are particularly attractive to power portable electronic devices and integrated sensor and communication microsystems. This is because i) electrochemical energy systems that directly convert chemical to electrical energy have inherent advantages of higher efficiencies, in comparison to heat and internal combustion engines. ii) the volumetric energy densities of electrochemical systems can be among the highest in comparison to other energy systems [11] and iii) they have an added benefit of having low-vibration, minimum or no air pollution and low noise operation.

Recent research has led to the development of the micro size single chamber solid oxide fuel cell (μ-SC-SOFC). In this approach electrodes are micropatterned closer together thereby reducing the ohmic losses at the electrolyte. The use of the

microfabrication techniques for SC-SOFC can potentially allow for fabrication of the multiple fuel cell units connected in combination of series or parallel connections. This architecture can allow an increase in the voltage, current, and total power of the entire assembly.

This dissertation focuses on investigating fabrication methods of inter-digitized design of μ-SC-SOFCs. Chapter 2 introduces the state-of-the-art in SC-SOFC and alternative manufacturing processes. Chapter 3 presents the fabrication design and alternative fabricating processes conducted in this research. Chapter 4 presents the preliminary results of experiments of these alternative processes. Based on these results, the direct writing process was studied further. Chapter 5 focuses on the effect of the dispersant on the LSCF slurry rheology. Chapter 6 focuses on evaluating the effect of LSCF slurry solid loading and binder concentration. Chapter 7 focuses on understanding the direct writing process parameters.

Table 1.1. Comparison of fuel cell technologies [12]

Fuel Cell Type	Common Electrolyte	Operating Temperature	System Output	Electrical Efficiency	Combined Heat and Power (CHP) Efficiency	Applications	Advantages
Polymer Electrolyte Membrane (PEM)*	Solid organic polymer poly-perfluorosulfonic acid	50 - 100°C 122 - 212°F	<1kW – 250kW	53-58% (transportation) 25-35% (stationary)	70-90% (low-grade waste heat)	▪ Backup power ▪ Portable power ▪ Small distributed generation ▪ Transportation ▪ Specialty vehicles	▪ Solid electrolyte reduces corrosion & electrolyte management problems ▪ Low temperature ▪ Quick start-up
Alkaline (AFC)	Aqueous solution of potassium hydroxide soaked in a matrix	90 - 100°C 194 - 212°F	10kW – 100kW	60%	>80% (low-grade waste heat)	▪ Military ▪ Space	▪ Cathode reaction faster in alkaline electrolyte, leads to higher performance ▪ Can use a variety of catalysts
Phosphoric Acid (PAFC)	Liquid phosphoric acid soaked in a matrix	150 - 200°C 302 - 392°F	50kW – 1MW (250kW module typical)	>40%	>85%	▪ Distributed generation	▪ Higher overall efficiency with CHP ▪ Increased tolerance to impurities in hydrogen
Molten Carbonate (MCFC)	Liquid solution of lithium, sodium, and/or potassium carbonates, soaked in a matrix	600 - 700°C 1112 - 1292°F	<1kW – 1MW (250kW module typical)	45-47%	>80%	▪ Electric utility ▪ Large distributed generation	▪ High efficiency ▪ Fuel flexibility ▪ Can use a variety of catalysts ▪ Suitable for CHP
Solid Oxide (SOFC)	Yttria stabilized zirconia	600 - 1000°C 1202 - 1832°F	<1kW – 3MW	35-43%	<90%	▪ Auxiliary power ▪ Electric utility ▪ Large distributed generation	▪ High efficiency ▪ Fuel flexibility ▪ Can use a variety of catalysts ▪ Solid electrolyte reduces electrolyte management problems ▪ Suitable for CHP ▪ Hybrid/GT cycle

**Direct Methanol Fuel Cells (DMFC) are a subset of PEM typically used for small portable power applications with a size range of about a subwatt to 100W and operating at 60 - 90°C.*

CHAPTER 2

Literature Review

Solid oxide fuel cell (SOFC) is a promising clean energy source for the future SOFCs directly converts electrochemical energy to electricity with higher conversion efficiency and with low emissions.

2.1. Operating Principle of SOFC

SOFCs have been in development since the late 1950s and have two configurations that are being investigated which include the planar (flat panel) and tubular. The charge carriers in the SOFC are the oxygen ions (O^{2-}). At the cathode, the oxygen molecules from the air are split into oxygen ions with the addition of four electrons. In chapter 1, the basic operating principle of solid oxide fuel cell (SOFC) was stated. The operating principle of SOFC technology is founded on electro ceramics which are advanced materials that exhibit unusual electrical properties. These ceramic materials are fast ion conductors but poor electron conductors. The oxygen ions are conducted through the electrolyte and combined with hydrogen at the anode, releasing four electrons. The electrons travel an external circuit providing electric power and producing a by-product which is heat. In contrast to other types of the fuel cells, SOFCs operate at relatively high temperatures, which enable the use various hydrocarbon fuels without external reformer and expensive noble metals. Hydrocarbon fuels need pre-reforming to

H_2 and CO. On the anode side, hydrogen combined with oxygen ion, forms water and releases two electrons. On Ni/YSZ anode side, carbon monoxide has a higher overpotential than hydrogen. It combined with oxygen ion, forming carbon dioxide and released two electrons. Equations (2.1) and (2.2) show the reaction formula [13].

$$H_2 + O^{2-} \rightarrow H_2O + 2e^- \quad (2.1)$$

$$CO + O^{2-} \rightarrow CO_2 + 2e^- \quad (2.2)$$

Fuel reforming can also take place on nickel at the anode. This occurs when steam is added to the hydrocarbon fuel, typically at a ratio of 3 parts steam to 1 part of fuel, the reaction of methane is then given by Equation (2.3).

$$CH_4 + H_2O \rightarrow CO = 3H_2 \quad (2.3)[13]$$

The hydrogen and carbon monoxide released by this reaction can then react individually with oxide ions emerging from the electrolyte. Equations (2.1) and (2.2) show the chemical reactions. Usually the CO conversion is sluggish so the shift reaction also occurs on the anode to produce more hydrogen. Equation (2.4) shows the chemical reactions:

$$CO + H_2O \rightarrow CO_2 + H_2 \quad (2.4)\ [13]$$

Especially for the single chamber SOFC, which is discussed later, hydrocarbon fuel can generate H_2 + CO in the operating chamber. For example, reaction formula for ethane is shown in the Equation (2.5) [14].

$$C_2H_6 + O_2 \rightarrow 3H_2 + 2CO \quad (2.5)$$

The operating efficiency of SOFCs in generating electricity is among the highest of the fuel cells at about 60%. Furthermore, the high operating temperature allows cogeneration applications to create high-pressure steam that can be used in many applications. Combining a high-temperature fuel cell with a turbine further increases the overall efficiency of generating electricity for a hybrid fuel cell with a potential of an efficiency of more than 70%. A recently report from the Ningbo Institute of Material Technology & Engineering Chinese Academy of Sciences states that a single SOFC (cathode materials is LaSrMnO, anode material is Ni-YSZ, electrolyte material is YSZ) can generate 0.5 - 0.6 voltage at different temperatures 850°C, 750°C and 700°C and the fuel utilization is as high as 98%, 91% and 70%.respectively. When the output voltage is 0.7V, the power density is up to 600, 460, 270mw/cm^2 at the respective temperatures state above. Figure 2.1 shows the output voltage corresponding to the fuel utilization at different temperature.

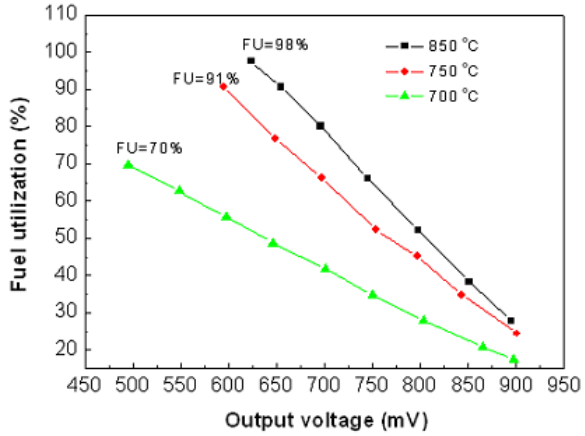

Figure 2.1. Single fuel cell's the output voltage corresponding to the fuel utilization at different temperatures [2]

2.2. Advantages and Disadvantages of SOFC's

As SOFCs operate at extremely high temperatures, it takes significant time to reach operating temperatures. In addition, SOFC may respond slowly to changes in electricity demand. It is therefore considered to be a leading candidate for high-power applications including industrial and large-scale central electricity generating stations. This section details the limitations and benefits of two types of high temperature operating fuel cells (SOFC and MCFC) by a comparative analysis.

High temperature fuel cells (MCFC and SOFC) are suitable for continuous power production, and are mostly used in large, stationary power plants. Their high operating temperature allows the opportunity for cogeneration – using waste heat to generate steam for space heating, industrial processing, or in a steam turbine, for power generation. In general, high temperature fuel cells exhibit higher efficiency and are less sensitive to fuel composition than low temperature fuel cells. SOFCs use a hard ceramic electrolyte and operate at temperatures up to 1000°C. In an MCFC, the liquid carbonate salt used as an electrolyte causes difficulties such as corrosion and creep and poses the risk of contaminating the reforming catalyst present inside the cell [15; 16]. With their solid oxide electrolytes, SOFCs do not have this limitation and have thus drawn more attention in high temperature fuel cell research. SOFCs also have many other advantages in comparison with other fuel cells. They are made from ceramic materials that do not have any moving parts or corrosive liquid electrolytes, leading to highly reliable electricity generation systems with low maintenance needs.

- They can operate directly on methane or natural gas, avoiding the need for expensive/difficult fuel reforming to generate pure hydrogen [17].
- They have low air and noise emissions. The high operating temperature results in high grade exhaust heat which provides a wider range of cogeneration options such as microturbines to enable the development of electricity generation products with ~60% efficiency. Efficiencies of this level have not been obtained by any other combination of technologies [18].

SOFCs are at the forefront of the environmentally benign technologies and are key to developing improved energy systems. They are targeted for use in three main energy applications: stationary energy sources, transportation and military applications [15; 16]. From the Figure 2.2, it can be seen that the SOFC has relatively high generating efficiency as high as 70%.

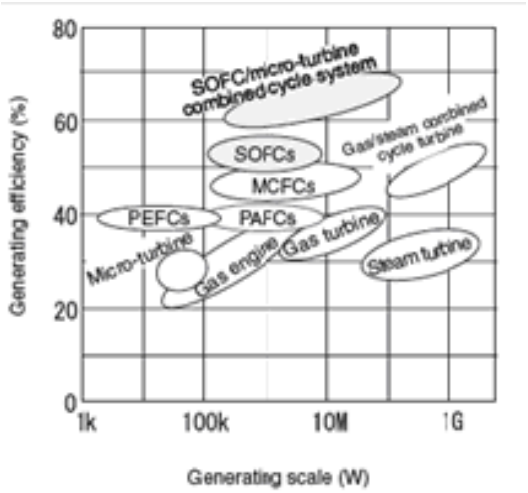

Figure 2.2. Current efficiency of various power systems and comparison of the output power performance between various power generation systems [20].

2.3. Conventional SOFC and Single Chamber-SOFC

Conventional SOFCs require two gas chambers in which the fuel and oxidant gases are separately supplied to each electrode without mixing. Based on this configuration, there are three major structures. These include the tubular, planar and monolithic configurations that can be used for SOFCs [19]. Figures 2.3, 2.4 and 2.5 show each of these structures.

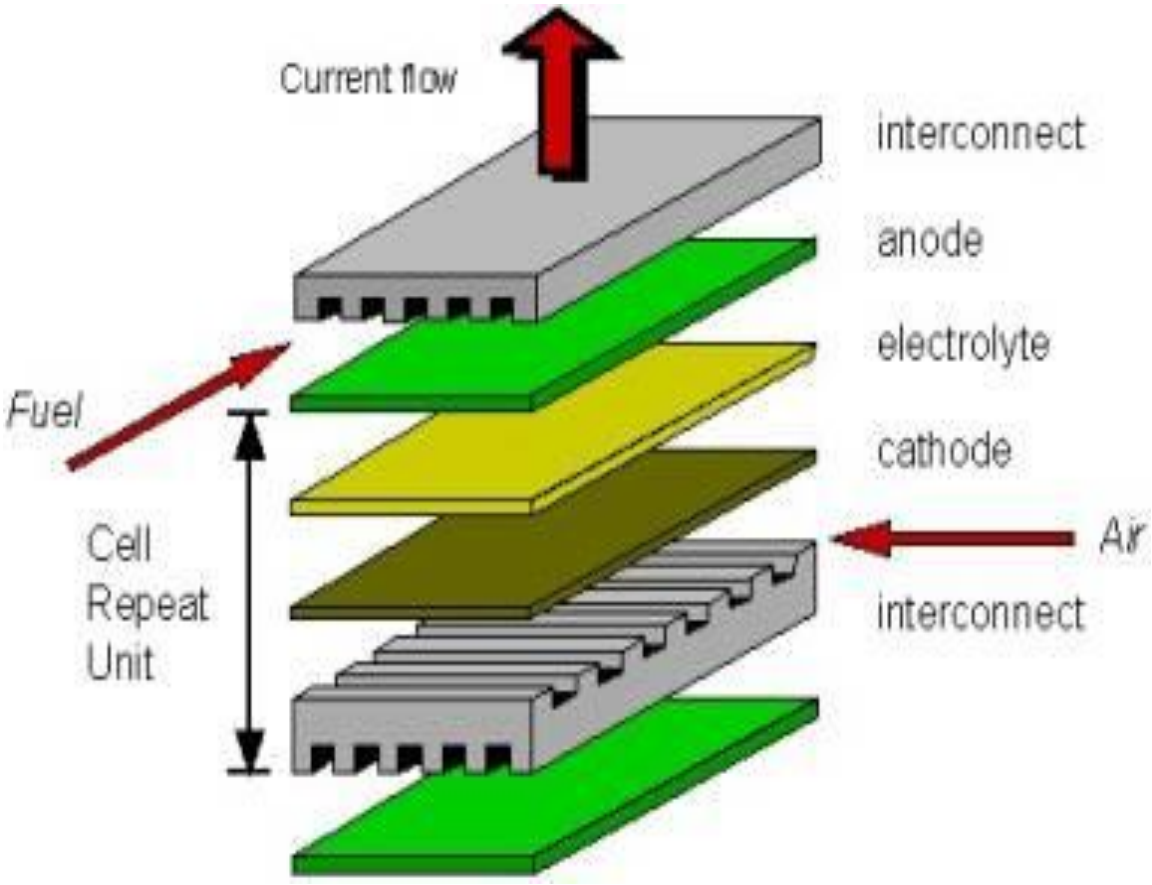

Figure 2.3. Configuration for a planar design SOFC [21]

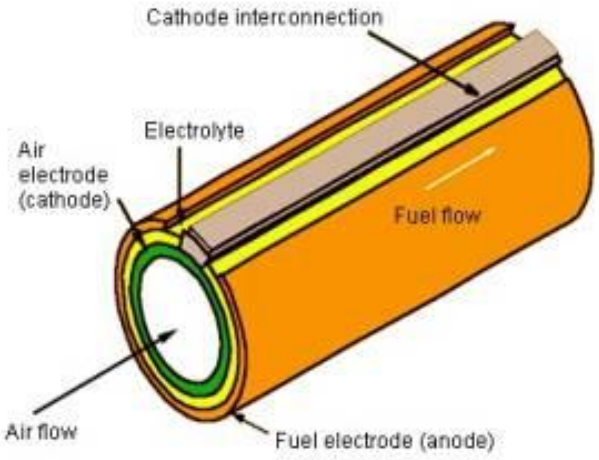

Figure 2.4. Configuration for a tubular design SOFC [21]

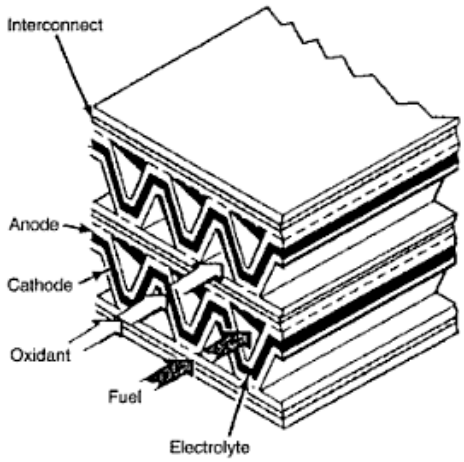

Figure 2.5. Configuration for a monolithic design SOFC [11]

In the planar design, the components are assembled in flat stacks, with air and fuel flowing through channels built into the cathode and anode. In the tubular design, components are assembled in the form of a hollow tube, with the cell constructed in

layers around a tubular cathode; air flows through the inside of the tube and fuel flows around the exterior [21]. The monolithic design uses a honey comb structure. Green laminates of air electrode/electrolyte/fuel electrode and interconnect are formed and co-sintered. This eliminates the need for high temperature seals, but requires forming the stack by co-sintering, a rather difficult task considering the different materials involved and microstructure requirements for each layer [19]. Table 2.1 compares the different SOFC cell configuration**.**

Among all designs of solid oxide fuel cells (SOFCs), major progress has been achieved with the tubular design. However, the electrical resistance of tubular SOFCs is high, and specific power output and volumetric power density are low. A planar cell structure is an attractive geometry for integration into a stack configuration.

Table 2.1. Comparison for the different SOFC cell configuration [11].

Style	Advantage	Disadvantage
Tubular	➢ Ease of manufacturing ➢ No need for gas tight cell sealing ➢ Less thermal cracking due to thermal expansion mismatch (longer life)	➢ Edge current collection ➢ Low – power density ➢ High materials cost
Planar (SOFC)	➢ Lower fabrication cost ➢ Ease in flow arrangement ➢ Higher power density	➢ High-temperature gas tight sealing ➢ High assembly effort and cost ➢ Stricter requirement on thermal expansion match
Monolithic	➢ Higher power density ➢ A corrugated design is easy to assemble	➢ For a corrugated design, the manufacturing process is complex.

However, due to its high operating temperatures, the gas-tight sealing between the chambers is problematic, raising manufacturing costs, and subsequently reducing long-term reliability. Therefore, the sealing of each gas chamber restrict the flexibility of configuring the system design. This has been one of the critical issues in SOFC design.

The configuration of single chamber SOFC (SC-SOFC) has the potential of overcoming this problem and meeting a flexible system design demand. A single chamber fuel cells that consists of only one gas chamber, where both the anode and the cathode are exposed to the same mixture of fuel and air, has been proposed by many researchers [22; 23; 24; 25; 26; 27].

Hibino and Iwahara [25] were pioneer researchers who demonstrated a working single chamber solid oxide fuel cell (SC-SOFC) operating at temperatures above 500^{o}C. SC-SOFC has only one gas chamber where the electrolyte and electrodes are exposed to the same mixture of fuel and oxidant gas. The major advantage of SC-SOFCs is the possibility of the direct use of hydrocarbon fuel without loss of fuel cell performance. However, in the case of conventional SOFC the direct use of hydrocarbon fuel usually leads to carbon deposition on anode side and as a result the fuel cell performance decrease [28]. Another advantage is related to the possibility of application of porous electrolyte [29], as the mechanism of operation is based on difference of catalytic activities of electrodes. This significantly simplifies technological requirements and cost effective technologies can be used for fuel cell fabrication, e.g. screen printing [29]. Moreover, SC-SOFC does not need high temperature sealing to separate the anode and

cathode chambers [30]. A major drawback of the SC-SOFCs is their lower fuel utilization than conventional SOFCs and this is currently the main development challenge.

There are two kinds of SC-SOFCs. One has a screen-printed cathode and an anode on the opposite side of the electrolyte as shown in the Figure 2.6 [14; 30; 31] and the other has linearly patterned cathode and anode on the same electrolyte surface as shown in Figure 2.7 [32; 33].

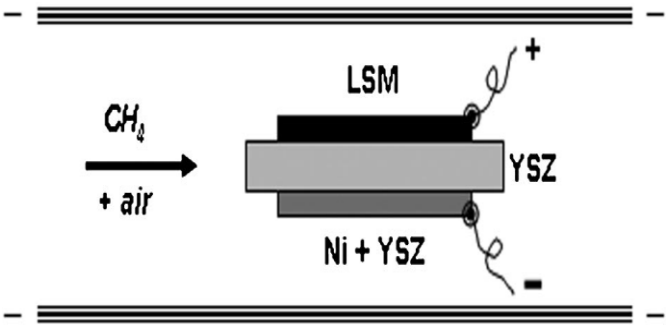

Figure 2.6. Schematic of screen-printed SC cell [31]

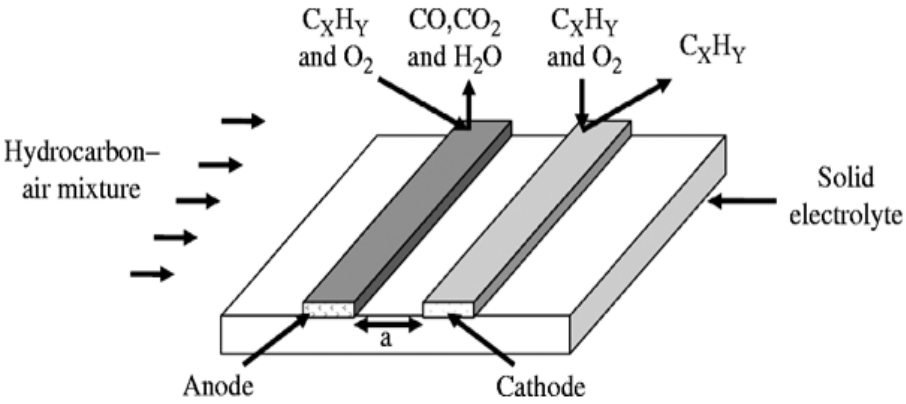

Figure 2.7. Schematic of co-planar SC cell [28]

The former type of SC-SOFC has recently received intensive research interest, whereas only a few studies are reported on the latter type involving a surface conduction between single-line-patterned electrodes on the electrolyte. However, the latter design of SC-SOFC has some advantages. In this design, the solid electrolyte used in this surface-conduction type SOFC does not have to be a pore-free thin film and it can be operated at lower temperatures, which makes the cell more shock resistant against both thermal and mechanical stresses. On the other hand, the electrolyte substrate can be manufactured easily by a die pressing operation. The ohmic resistance of the cell can also be decreased simply by narrowing the gap between the two electrodes. Furthermore, if the anode and cathode are micropatterned to be placed closely together, this type of a SC-SOFC will produce a higher power density in a reliable manner.

2.4. Fabrication Techniques for μ-SC-SOFC and Issues

With the development of the micro-electromechanical systems (MEMS) and portable electronic devices, miniaturized fuel cells are attractive candidates for power sources. Compared with conventional electrochemical batteries, micro solid oxide fuel cells are capable of higher energy densities and lower recharging times. Table 2.2 shows the summary of standard and μ–SOFC and PEMFC stack performance values in area and volumetric power density [9].

μ-SOFCs are in their early stages and many researchers are attempting the utilization of different microfabrication techniques for their manufacture. Using micropatterning methods, electrode can be deposited closer together reducing the ohmic

losses at the electrolyte. In addition, using microfabrication, the architecture of SC-SOFC can be connected in combinations of series or parallel arrays to increase voltage, current, and total power of the entire assembly.

Table 2.2. Summary of standard and µ–SOFC and µ-PEMFC stack performance values in area and volumetric power density

Systems	Area power density ($mWcm^{-2}$)	Volumetric power density ($mWcm^{-3}$)
Standard PEMFC~80°C	800 [34]	1600 [34]
µ-PEMFC ~25°C	195 [35]	~4000*
Standard SOFC 750°C	308 [36]	280 [36]
µ-SOFC ~600°C	145 [37]	~6000**

Note:
* volumetric power density estimated from [38] using a cell volume of 0.02 cm^3
** volumetric power density estimated from [37] using a cell volume of 0.02 cm^{-3}

From a commercial perspective the fuel cell industry is concerned in manufacturing of µ-SC-SOFC with high quality and low cost. The concept of fabricating µ-SC-SOFC is in its primitive stages. This dissertation focuses on the fabrication of parallel-connected inter-digitized design µ-SC-SOFCs. Figure 2.8 shows the design of fuel cell structure.

The development of µ-SC-SOFC has had incremental attempts. Hibino, (1996) the pioneer of SC-SOFC fabricated a new cell design with interpenetrating comb-like electrode pattern on the same surface of an electrolytic material with feature sizes in the millimeter range [39]. Chung and Chung carried out finite element modeling of a micro-SC-SOFC with side-by-side design [40]. The focus of research has been around

improving the μ-SC-SOFC's efficiency and reducing the operating temperature. Most researchers have based their work on a co-planar design to test the different electrodes and electrolyte materials' characteristic, operating parameters and power output [41; 42] . The research efforts for the single sided planar design have been explained below:

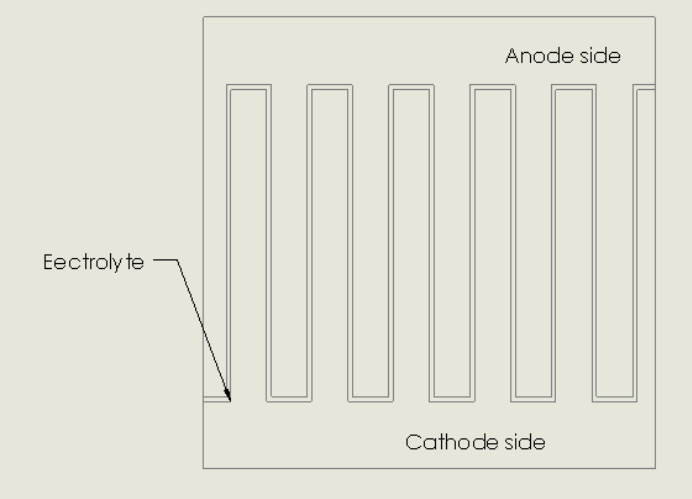

Figure 2.8. Parallel-connected inter-digitized design micro-SC-SOFCs, unit (mm)

2.4.1. MIMIC method. In Buergler works [31], initial attempts have been made to introduce micromolding in capillaries (MIMIC) for the preparation of μ-SC-SOFCs. MIMIC is one of the soft lithography methods. Generally, it allows the deposition of polymers and ink molecules onto the various substrates. In this research, author used the MIMIC to deposit the ceramic anode and cathode material on the CGO (electrolyte) substrate. This process includes the following steps:

(a) Place PDMS-mold on ion conducting CGO substrate.

(b) Apply suspension droplets in the reservoirs at the opening of the microchannels.

(c) Repeat this step on each side of the mold.

(d) Capillary forces fill microchannels with anode suspension of the PDMS mold

(e) Capillary forces fill microchannels with cathode suspensions of the PDMS mold.

(f) Excess suspension is removed from the reservoirs.

(g) The microlines are slowly dried.

(h) Remove PDMS-mold: interdigitating array of anode and cathode stripes.

(i) This forms a micro-cell.

(j) Co-sinter the anode arrays

(k) Co-sinter the cathode arrays

(l) Apply Pt-paste

(m) Attach flattened Pt-wire

(n) Prepare the assembly as current-collectors.

(o) Perform subsequent heat treatment.

In this work the cathode and anode were fabricated by PDMS-molds on the electrolyte substrate. The gap between two electrodes was reduced to 10 μm. However, since not all the capillaries were completely filled an incomplete array of cells was formed. The process has very low repeatability and low quality. Anther issue in this method is that the fluid used in micromolding in capillaries technique (MIMIC) which is powder – free chemical solution having low solid loading (<5 vol%) and low Viscosity (<200mPa.s). Figure 2.9 shows the schematic of MIMIC process for preparation of the micro cells.

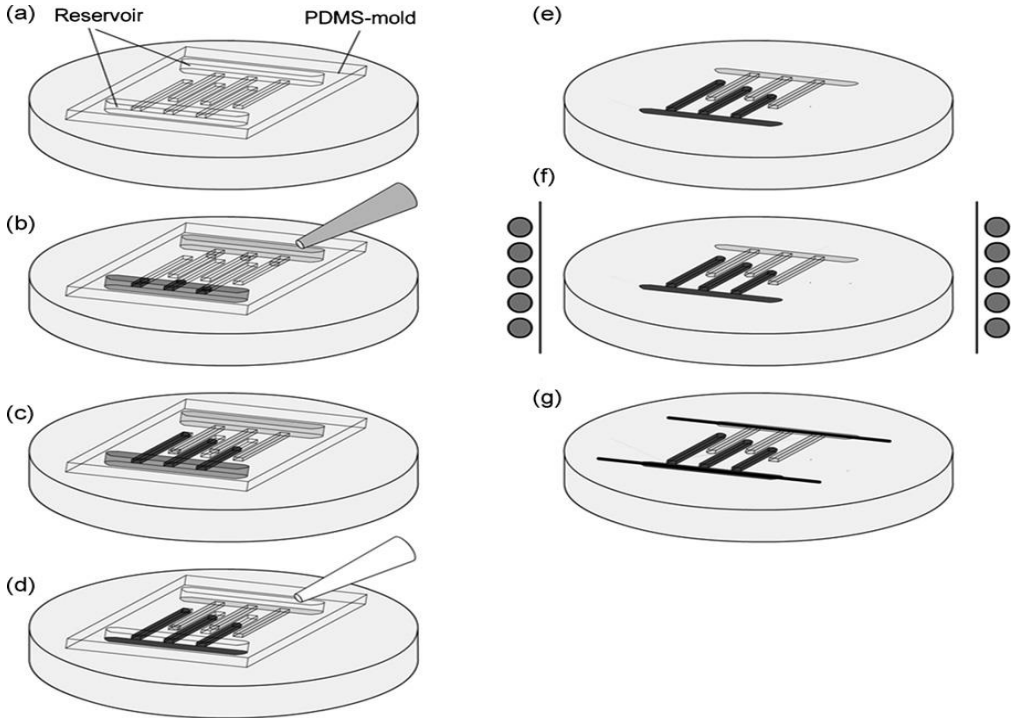

Figure 2.9. Schematic of MIMIC process for preparation of the micro cells [31]

2.4.2. Microfluidic lithography. In Sung-Jin Ahn's paper [43], they introduced a microfluidic device made of PDMS to fabricate ceramic microstructures using the colloidal suspension of relatively high solid loadings (>20 vol%). The lower overall pressure allows gas contained within connected volumes of the channel networks to escape out. As the pressure is returned to atmospheric level, the suspensions from the reservoirs flow in to rapidly fill the voids left within the channels. This procedure, called vacuum-assisted microfluidic lithography (mFL), is effective to produce complex microstructures in a relatively short period.

Figure 2.10 shows the schematic of the vacuum-assisted microfluidic lithography with ceramic suspension. The process includes the following steps:

(a) Prepare polydimethylsiloxane (PDMS) mold through photolithography.

(b) Place PDMS mold on the Si wafer substrate.

(c) Apply two different suspensions at the entrances of reservoir and evacuate.

(d) Fill the channels by returning to atmospheric pressure.

(e) Remove PDMS mold after complete infiltration and drying.

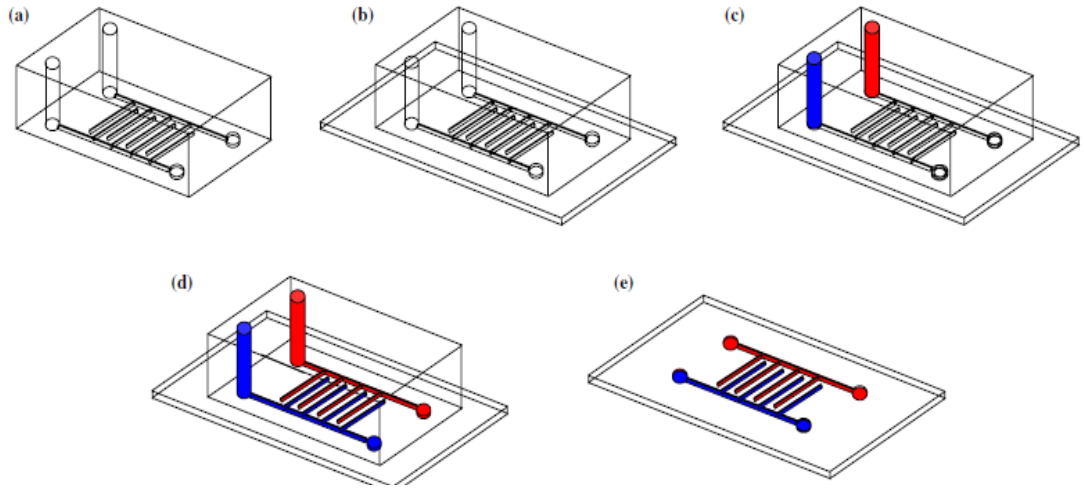

Figure 2.10. Schematic of the vacuum-assisted microfluidic lithography with ceramic suspension [32]

In Sung's research, the SC-SOFC was downsized to the micron level. However, suspension drying behavior plays an important role in the fabrication of well defined micro pattern structure. This method can use colloidal suspensions with low viscosities. However, this approach has low repeatability.

2.4.3. Direct writing. Direct writing involves extrusion of suspension filament on substrate and is amenable for mass production. In this method, the suspension's solid

loading is up to 60%. The suspension's viscosity is higher than those in soft lithography are. The direct-writing principle is shown in the Figure 2.11. In 2006, Prof. Jennifer A Lewis [42; 44] introduced the direct ink writing method to generate three dimensional ceramic structures. This approach allows one to design and rapidly fabricate ceramic materials in complex 3D shapes without the need for expensive tooling, dies, or lithographic masks. The ability to pattern ceramic materials in three dimensions (3D) is critical for structural, functional, and biomedical applications.

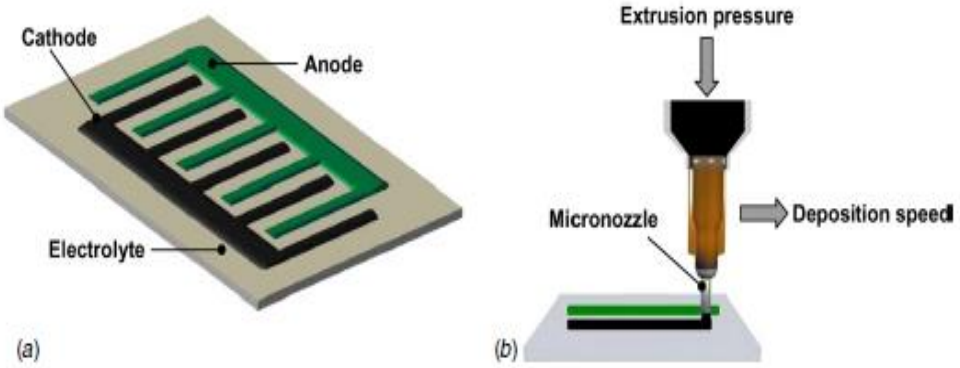

Figure 2.11. (a) Schematic illustration of a single-chamber solid oxide fuel cell in single-face configuration with interdigitated electrodes. (b) Schematic illustration of the robot-controlled direct-write microfabrication of electrode lines on an electrolyte plate. The quality of the deposited structures strongly depends on the two main process parameters, extrusion pressure and deposition speed [45].

In 2005, Yong Bum Kim [45] successfully implicated the direct write technique to fabricate serial-connected integrated planar solid oxide fuel. They direct-wrote the anode (YSZ+NiO) and Cathode (LSCF) on the side of a partially Yttria stabilized

zirconia substrate. In 2006, Sung-Jin Ahn et al. [43]used the direct write technique to extrusion the anode (NiO-SDC-Pd) and cathode(LSM) onto the substrate of YSZ through a syringe nozzle. The average width of anode was about 500μm and that of cathode was about 450μm. In 2007, Melanie Kuhn [46] implicated the direct write technique to fabricate parallel-connected SC-SOFC on electrolyte pie. According to her research, the electrolyte width was more than 500 μm. The average gap between the electrodes was around 1mm. In this experiment, both cells exhibited stable open circuit voltage and peak power density of 0.9V and 2.3mWcm^{-2}.

2.5. Research Goals

In this research, a single chamber SOFC with inter-digitized structure of electrolyte and electrodes is proposed. Several fabrication methods are being attempted to evaluate a reliable technique to fabricate μ-SC-SOFC with high quality, high repeatability, low material cost, and low manufacturing cost. Further, optimization of the feasible candidate manufacturing techniques will be performed.

CHAPTER 3

Methodology

3.1. SC-SOFC Structure and Fabrication Issues

With the development of the micro-electromechanical systems and miniatureized electronic devices, microengineering techniques for the realization of structures and devices at the microscale have been progressing rapidly.

Some micro/nano fabrication techniques to fabricate the micropatterns precisely on planar substrates include EBL, soft lithography, photo lithography, direct-writing, and others. Based on literature review, initial attempts have focused on the use of soft lithography and direct-writing pattern for co-planar SC-SOFC fabrication. However, these methods have low repeatability and low quality.

This research focuses on microfabrication of parallel-connected inter-digitized design of μ-SC-SOFCs. The Figure 2.8 shows the detail structure. In this design, the anode and cathode of the fuel cells are located at the same side of electrolyte. In this chapter, different proposed fabrication approaches for μ-SC-SOFCs are discussed.

3.2. Material Requirement and Issues

3.2.1. Electrode material. In particular, the following specific properties are required for the anode materials.

1) Stability: the anode must be chemically, morphologically, and dimensionally stable at a given operating temperature in the fuel gas environment; it must also be tolerant towards contaminants.
2) Ionic and electronic conductivity: a maximum electrical conductivity under a large variety of operating conditions is desired to minimize the ohmic losses.
3) Compatibility: the anode must be chemically, thermally, and mechanically compatible with the other fuel cell components during fabrication as well as under operation.
4) Porosity: the porosity of the anode must be tailored with regard to mass transport considerations as well as mechanical strength. For the cathode, the porous structure is to enhance gas access to catalytically activeate towards oxygen reduction [47].

For the thin films of micro solid oxide fuel cells, these requirements are still followed. No matter what technique is used, the choices of cathode and anode material are based on stability, conductivity, compatibility and porosity. Yttria-stabilized-zircona (YSZ) is conventional electrolyte material, which has good ionic conductivity at high temperature. Nickel has a good electronic conductivity, stability and compatibility with YSZ. Therefore, two phase cermets (ceramic–metal composites) that combine all properties are used. For cathode, perovskites are commonly chosen [48]. In our research, the anode material is 8mol% YSZ + NiO with weight ratio 60:40. The cathode material used in this experiment is Lanthanum Strontium Cobalt Ferrous - LSCF ($La_{0.6}Sr_{0.2}Fe_{0.8}Co_{0.2}O_{3-\delta}$).

3.2.2. Electrolyte material. Materials requirements for the electrolyte include: (1) High ionic conductivity with negligible electronic conductivity to reduce ohmic losses.(2) Chemical stability with electrode. (3) Suitable mechanical properties. (4) Dense microstructure [9].

The conventional electrolyte material is 8% yttria stabilized zirconia (YSZ). Recently there are advanced materials under consideration to replace the conventional electrolyte. However, some issues associated with the stability of these materials under the harsh operation environment still exist, for example, the low mechanical strength and stability of doped ceria, and the poor chemical compatibility of LSGM with NiO anode. YSZ is still the most commonly used electrolyte material for SOFCs because of its unique properties such as high chemical and thermal stability, excellent mechanical properties and pure ionic conductivity over a wide range of conditions [49]. In this research, 8 mol % YSZ is chosen as the electrolyte material.

3.3. Micropatterning Techniques

In this research, a combination of several micropatterning techniques with complimentary deposition methods are being attempted to find valid high quality, high repeatability and low cost fabricating process for μ-SC-SOFCs.

In this research, the micropatterning techniques utilized include electron beam lithography (EBL), soft lithography, and photolithography. Deposition methods include pulsed laser deposition (PLD) and magnetron sputtering (MS). PLD and MS are applied to deposit ceramic electrode (electrolyte) material into the pattern. In the literature [50],

four techniques i) Magnetron sputtering, ii) Pulsed laser deposition, iii) Chemical vapor deposition, and electron beam evaporation, have been shown to be compatible with IC process. The electrolyte in μ-SC-SOFCs have been configured in either free standing [37; 51; 52] or supported on substrate designs [33]. The direct writing technique used is analogous to the ones used in relevant literature [43; 46]. Using the direct writing technique, the ceramic slurry (suspension) can be printed on the substrate in the required pattern design.

3.3.1. Electron beam lithography (EBL). Electron beam lithography is a maskless process based on direct writing using an electron beam. The sample is covered by an electron sensitive resist layer, a focused beam scans across the sample, and turns on and off according to the data input, exposing the resist point-by point to produce the image. Figure 3.1 presents a schematic illustration of EBL process [53].

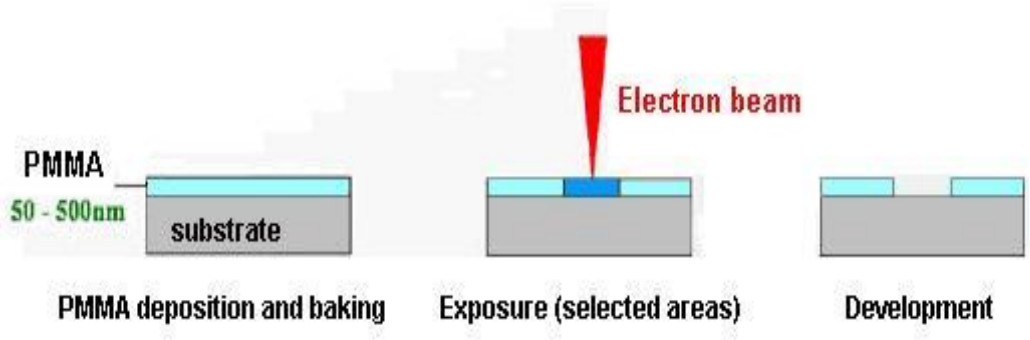

Figure 3.1. Electron beam lithography-process steps [53]

Electron lithography offers higher patterning resolution than optical lithography because of the shorter wavelength possessed by the 10-50kev electrons that it employs. The resolution of optical lithography is limited by diffraction, but this is not a problem for electron lithography [54]. The reason for this is the short wavelengths (0.2-0.5 angstroms) exhibited by the electrons in the energy range that are being used by EBL systems. In summary, the pros of the EBL include:

Electron lithography offers higher patterning resolution than optical lithography because of the shorter wavelength possessed by the 10-50kev electrons that it employs. The resolution of optical lithography is limited by diffraction, but this is not a problem for electron lithography [54]. The reason for this is the short wavelengths (0.2-0.5 angstroms) exhibited by the electrons in the energy range that are being used by EBL systems. In summary, the pros of the EBL include:

1) E-beam lithography can directly write the pattern onto the electron-sensitive resist. Compare to the optical lithography, this method don't need to develop the mask.
2) More precise than photolithography.
3) Independent of the limit of light diffraction.

3.3.2. SOFT lithography. Soft lithography is one of the earliest forms of mechanical patterning introduced. Soft lithography has been widely used in microfluidic devices and bio-related experiments due to its low cost, flexible and fast prototyping nature. It is mainly used for patterning of micrometer sizes or features greater than 100 nm in size. This is because at lower sizes it is difficult to control the amount and flow of a

liquid ink, in addition, the stamps are not sufficiently rigid. The feature resolution of the printing is poorer than nanoimprint, where a hard mold and embossing is used.

Soft lithography is an umbrella term for many methods designed to pattern materials like polymers. In Xia and Whitsides soft lithography review [55], they stated quite a few different methods that are regarded as soft lithography methods. They are as described below:

1) Near-Field Phase Shift Lithography. A transparent PDMS phase mask with relief on its surface is placed in conformal contact with a layer of photoresist. Light passing through the stamp is modulated in the near-field. If the relief on the surface of the stamp shifts the phase of light by an odd multiple of (a node in the intensity is produced. Features with dimensions between 40 and 100 nm are produced in photoresist at each phase edge [56].
2) Replica Molding. A PDMS stamp is cast against a conventionally patterned master. Polyurethane is then molded against the secondary PDMS master. In this way, multiple copies can be made without damaging the original master. The technique can replicate features as small as 30 nm [57].
3) Micromolding in Capillaries (MIMIC). Continuous channels are formed when a PDMS stamp is brought into conformal contact with a solid substrate. Capillary action fills the channels with a polymer precursor. The polymer is cured and the stamp is removed. MIMIC is able to generate features down to 1 μm in size [57; 58].

4) Microtransfer Molding (TM). A PDMS stamp is filled with a prepolymer or ceramic precursor and placed on a substrate. The material is cured and the stamp is removed. The technique generates features as small as 250 nm and is able to generate multilayer systems [59].
5) Microcontact Printing (CP). An "ink" of alkanethiols is spread on a patterned PDMS stamp. The stamp is then brought into contact with the substrate, which can range from coinage metals to oxide layers. The thiol ink is transferred to the substrate where it forms a self-assembled monolayer that can act as a resist against etching. Features as small as 300 nm have been made in this way [60].
6) Techniques used in other groups include micromachining of silicon for microelectromechanical systems (MEMS) and embossing of thermoplastic with patterned quartz [61].

3.3.3. Photolithography. Photolithography is a process used in microfabrication to selectively remove parts of a thin film or the bulk of a substrate. It uses UV light to transfer a geometric pattern from a photo mask to a light-sensitive chemical photo resist, on the substrate. A series of chemical treatments then engraves the exposure pattern into the material underneath the photo resist. It shares some fundamental principles with photography in that, the pattern in the etching resist is created by exposing it to light, using either a projected image or an optical mask. Comparing to EBL, photolithography is not a direct write method. After exposed, the pattern can not be used. The development is performed to remove the un-polymerized resist. After hard baking the pattern, the pattern can be used to deposit material. Figure 3.2 presents a schematic illustration of

photolithography process. The steps involved in the photolithographic process are (1) wafer cleaning, (2) barrier layer formation, (3) photoresist application, (4) soft baking, (5) mask alignment, (6) exposure and development, (7) and hard-baking.

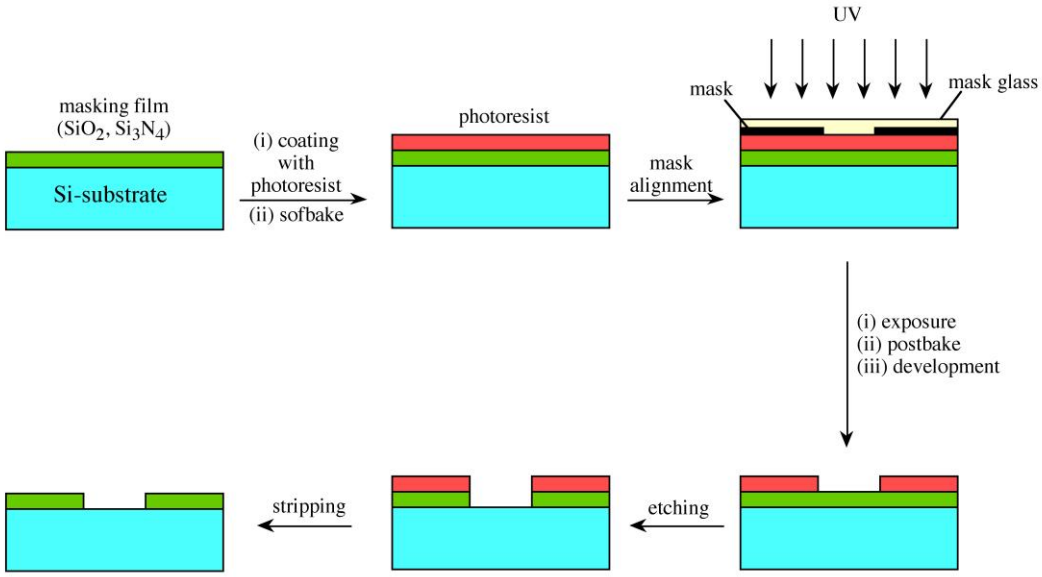

Figure 3.2. Photolithography process steps [62]

3.3.4. Deposition method: pulsed laser deposition (PLD). The commonly used vapor deposition (VD) methods include the PLD and magnetron sputtering. This research focuses on the use of the Pulsed laser deposition technique. Figure 3.3 presents a schematic illustration of PLD process. PLD relies on a photon interaction to create an ejected plume of material from any target. The vapor (plume) is collected on a substrate placed a short distance from the target. Though the actual complex physical processes,

material is removed. One can consider the ejection of material to occur due to rapid explosion of the target surface due to superheating. The laser-induced expulsion produces a plume of material with stoichiometry similar to the target. It is generally easier to obtain the desired film stoichiometry for multi-element materials using PLD than with other deposition technologies [63].

Pulse laser deposition has become a precision based technique for depositing thin films of a variety of materials. The ability to deposit almost any material, preserve the stoichiometry of multicomponent compounds and to carry out reactive deposition has finally been recognized and renewed the interest in this technology. Ceramic material thin films deposited by pulsed laser deposition have been known for a couple of years, since the availability of high-energy pulsed UV lasers.

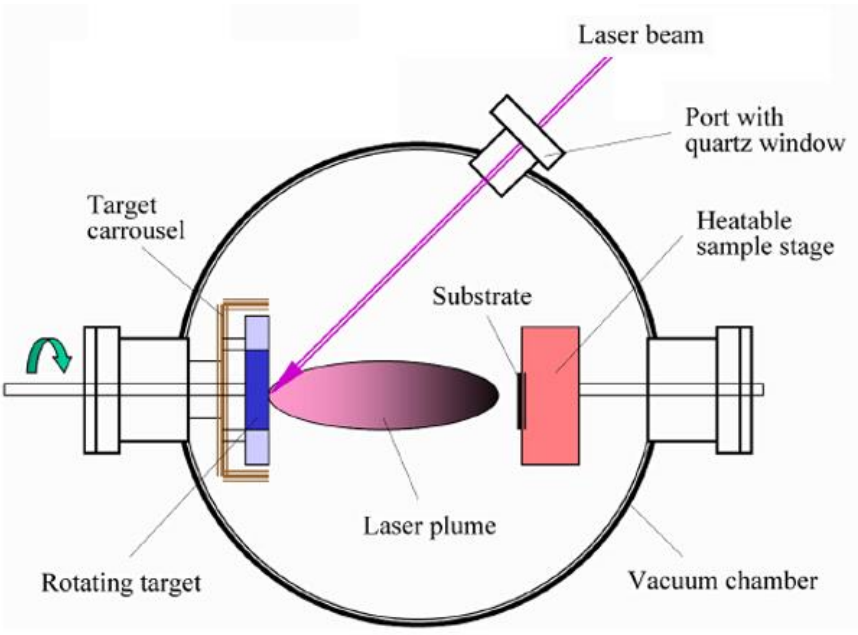

Figure 3.3. Schematic illustration of PLD process [63]

3.4. Alternative Fabricating Processes

This section discusses the combination of different fabrication processes including their feasibility towards μ-SC-SOFC manufacturing.

3.4.1. EBL+PLD. Two types of alternative parallel-connected inter-digitized design μ-SC-SOFCs can be fabricated. In the first configuration we can deposit the anode and cathode material on the electrolyte substrate with the e-beam pattern. In the other design, we can choose others substrates, such as glass, or Al_2O_3 wafer, and deposit all of three components (anode, cathode, and electrolyte) on the substrate. The process sequence of the second design is stated below:

1) Prepare the electrolyte wafer.
2) Spin coat PMMA(electronic sensitive resist) on the wafer.
3) Exposure of the electrolyte pattern by EBL.
4) Deposit of 8mol %YSZ on the wafer.
5) Removal of the resist.
6) Anneal the 8mol% YSZ at 1350^{o}C for 3 hours.
7) Exposure of anode pattern by EBL.
8) Deposit of anode material on the wafer.
9) Removal of the resist.
10) Anneal the anode material at 1350^{o}C for 3 hours.
11) Spin coat PMMA on the wafer with the cathode pattern.
12) Exposure of cathode pattern to e-beam.
13) Deposit of cathode material on wafer.

14) Removal of the resist.

15) Anneal the cathode material at 1000^{o}C for 3 hours.

16) Bond electrical wires by platinum paste on the sides of the anode and the cathode.

17) The fuel cells were heated and held at 1000°C for an hour.

18) The final products were subjected to a hydrogen reduction procedure at 700ºC for 3 hours to convert NiO to Ni in anodes.

19) Test the SC-SOFC.

3.4.2. Soft lithography + photolithography. This μ-SC-SOFC design has an inter-digitized anode and cathode structures on the same side of the electrolyte. Based on this design, the feasibility of Microfluidic method was tested for fabricating micro single chamber solid oxide (μ-SC_SOFC) fuel cell. The mask pattern for the mold was designed as shown in Figure 3.4. The area between the outside two squares and the area insides of the zigzag pattern are not transparent to UV light. The use of photolithography technique and this mask design were used to make the micro pattern on the Si wafer. The Si wafer was used to cover Polydimethylsiloxane (PDMS) within a mold box. The placement of the Si wafer on the Polydimethylsiloxane (PDMS) enabled the transfer of the micro-pattern on to the top of the PDMS surface. This assembly was subjected to suitable vacuum for a period one hour. Further the silicon wafer was peeled systematically. The removal of the silicon wafer enabled the release of the PDMS mold. The details of the photolithography technique mask design to make the micro pattern on the Si wafer and the removal of the Si wafer to release the PDMS mold is explained as shown in Figure 2.10.

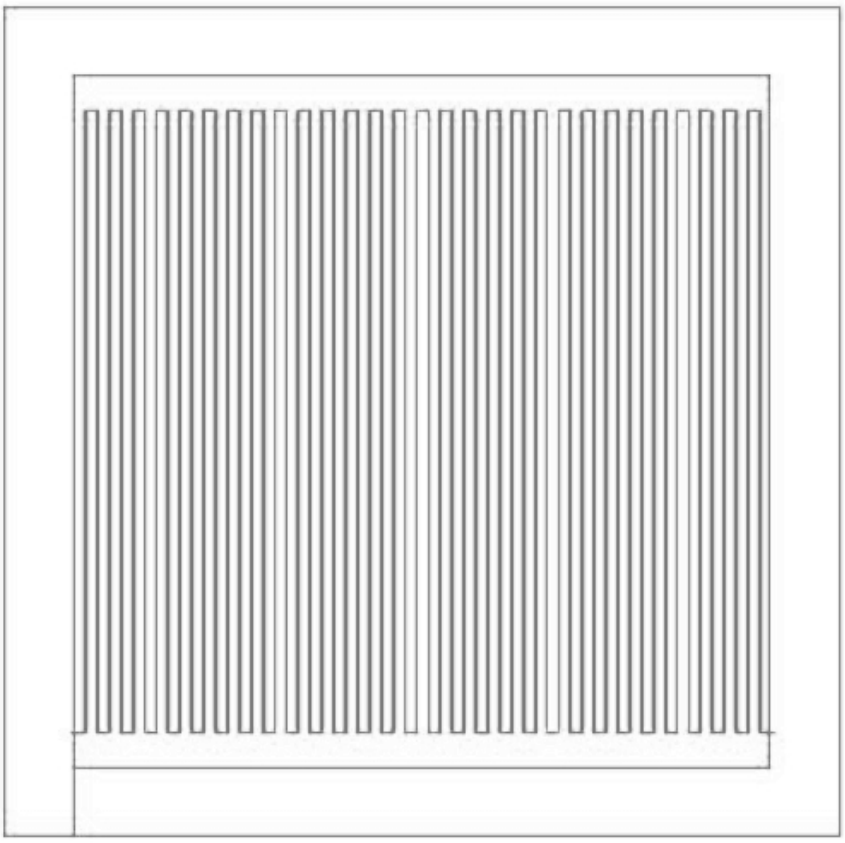

Figure 3.4. Mask of PDMS mold

3.4.3. Photolithography + PLD. In this approach, photolithography technology was used in combination with the PLD. Photolithography was used to create the electrolyte, cathode, and anode patterns on the substrate. And then PLD was used to deposit the thin film ceramic material. Figure 3.5, 3.6 and 3.7 show the major steps on fabricating the SOFC. The combination of photolithography and PLD was used to generate the anode, cathode and electrolyte structure respectively. In order to get the required microstructures, two major parameters: deposition pressure and substrate temperature were controlled. Before each deposition, the substrate needs be pre-cleaned

by plasma machine. After each deposition cycle and lift off the photoresist and the ceramic pattern need to be annealed.

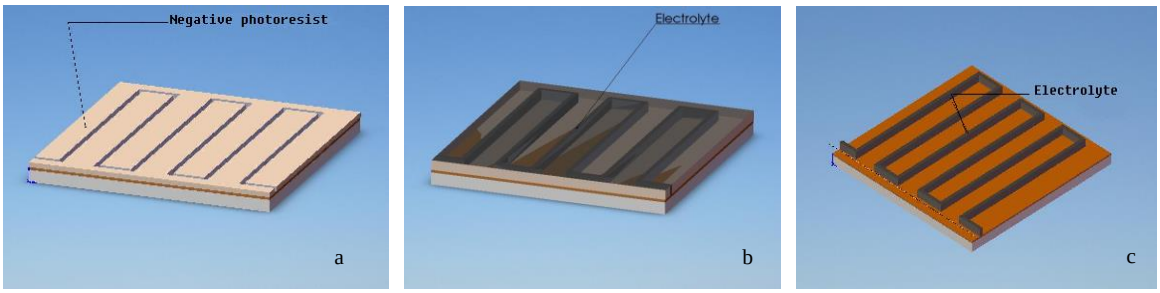

Figure 3.5. Fabricate electrolyte (a) Generate electrolyte pattern by photolithography; (b) After plasma etching, depositing the YSZ material; (c) Lift-off photo resist and anneal the YSZ material.

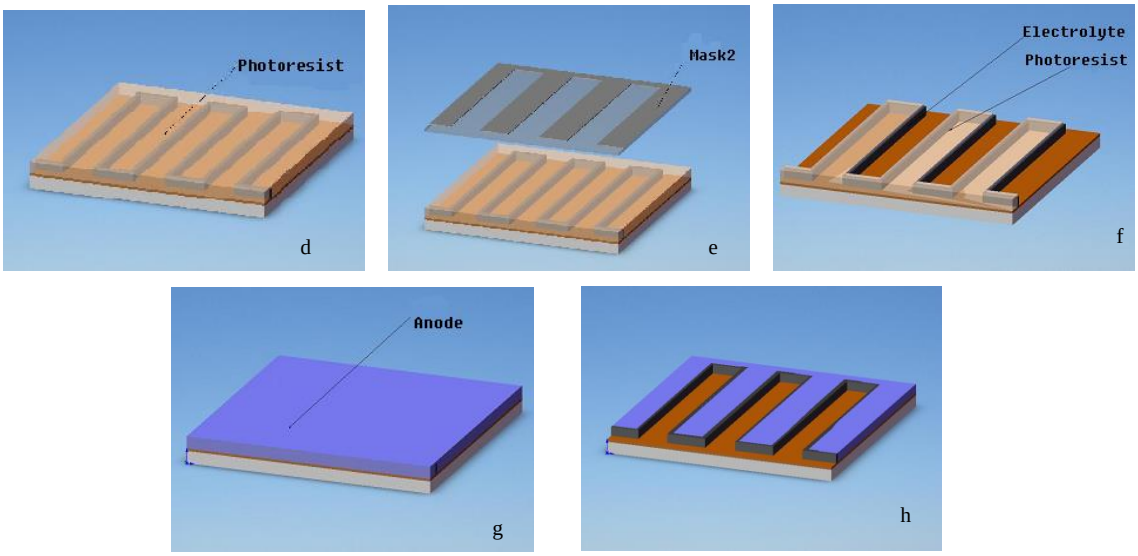

Figure 3.6. Fabricate anode (d) Coating the photo resist; (e) Generate anode pattern by photolithography; (f) Develop the anode resist pattern; (e) Sample and etch the pattern by plasma; (g) Deposit YSZ + NiO material; (h) Lift of the photo resist and anneal the anode material.

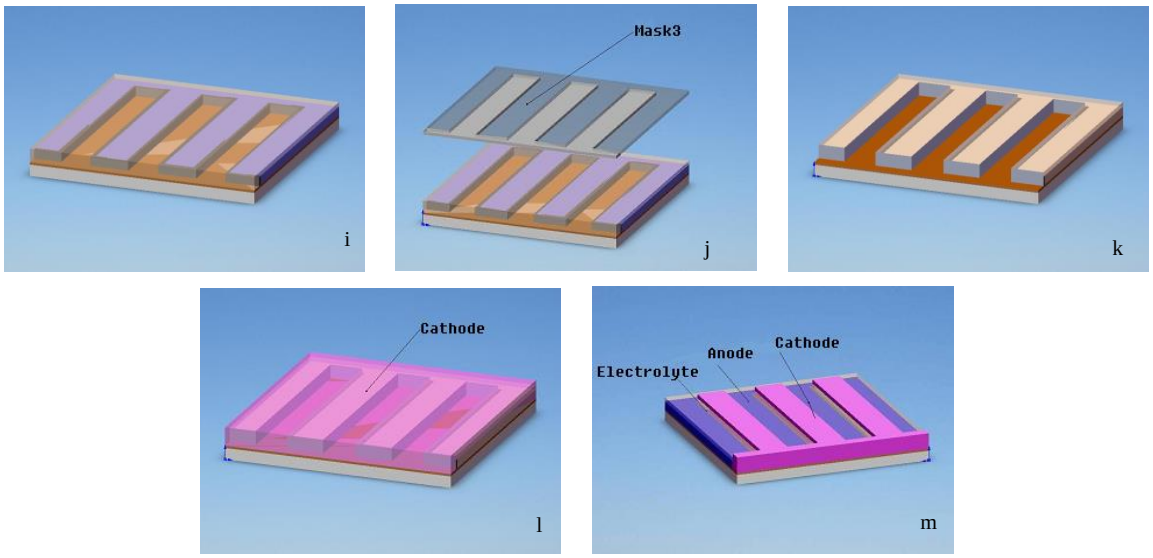

Figure 3.7. Fabricate cathode (i) Coat photo resist on the (h) pattern; (j) Generate cathode pattern by photo lithography; (k) Develop the cathode resist pattern (j) Sample and etch the pattern by plasma; (l) Depositing the LSCF material; (m) Lift of the photo resist.

The targets for PLD were prepared from powders. The average particle size of the electrolyte powder was around 500nm. The average particle sizes of anode and cathode powders were 50nm and 500nm respectively. All powders were pressed unitarily at room temperature at 10 tons for 10-15 min. Further, electrolyte and anode powder was baked at 1400°C for 6 hours and cathode powder was baked at 1250°C for 3 hours.

3.4.4. Direct writing. Direct writing involves extrusion of a suspension filament on substrate and is amenable for mass production. In this method, the suspension‘s solid loading can be increased as high as 60%. The suspension’s viscosity is higher as compared to those used in soft lithography. This approach allows one to design and rapidly fabricate ceramic materials in complex 3D shapes without the need for expensive

tooling, dies, or lithographic masks. The ability to pattern ceramic materials in 3D is critical for structural, functional, and biomedical applications.

At 2005, Yong Bum Kim introduced this technology for the fabrication of the solid oxide fuel cell. In direct-write microfabrication, powdered electrode materials are first synthesized into inks that are subsequently extruded through a micronozzle onto an electrolyte plate mounted on a robot-controlled platform. The microfabricated structures are then sintered to remove the organic components of the inks and to obtain porous electrodes. Processing–structure relationships were obtained using systematic experimentation for the direct-write microfabrication of nickel oxide–yttria stabilized zirconia (NiO–YSZ) anodes and lanthanum strontium manganite (LSM) cathodes on an YSZ electrolyte. Single-chamber μ-SOFCs were fabricated with interdigitated electrodes of a few hundred microns in size[64]. Figure 3.8 schematically illustrates the SC-SOFC in coplanar design and direct writing process map. The direct writing system comprised of a micro extrusion system, pressure regulator, sample holder and motion controller. The micro extrusion system includes air cylinder, piston, reservoir retainer, and micronozzle. This procedure includes the following steps:

1) Prepare the electrolyte substrate.
2) Prepare the anode and cathode slurry.
3) Fill the anode slurry into the reservoir retainer, which is held into an air cylinder.
4) Control the air pressure for the piston loaded on the end of the retainer. By adjusting the pressure, slurry was extruded from the micronozzle. Simultaneously, the velocity, acceleration and deceleration of motion stage were controlled by the

motion controller. Sequential lines of anode were written on the electrolyte substrate.

5) Glue the platinum wire by anode slurry.
6) Anneal the anode lines.
7) Fill the cathode slurry into the reservoir retainer. Repeat the step 4.
8) Glue the platinum wires by cathode slurry.
9) Annealing the cathode lines.
10) Test the fuel cell.

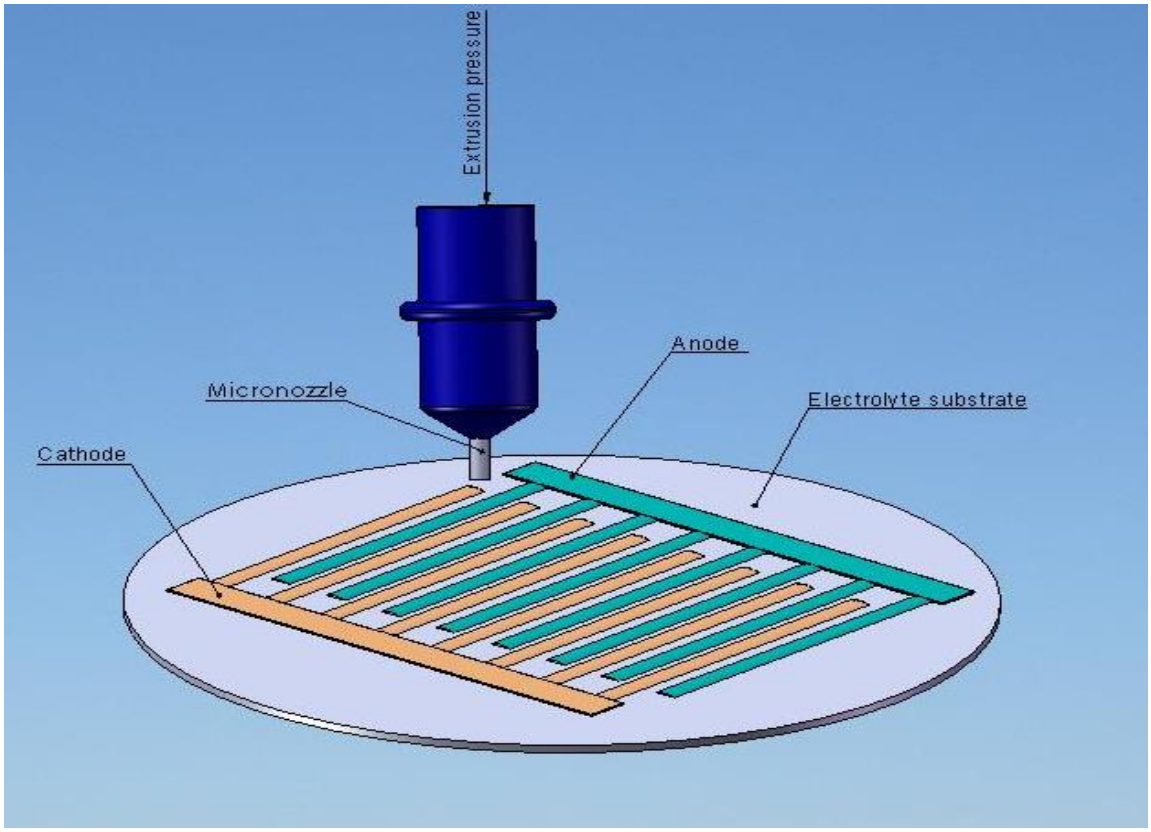

Figure 3.8. Schematic illustration of a SC-SOFC in coplanar design and process

By controlling the air pressure, velocity, the mixture ratio of the slurry and the distance between the nozzle and the substrate, the required the micro structure of anode and cathode can be met. After annealing, the shapes of printed electrodes were retained. The steps for direct-writing are stated below:

1) Prepare substrate.
2) Determine ratio of each material component for the slurry.
3) Parameter research on the direct writing process (includes air pressure of the piston, velocity and acceleration of the motion controller).

3.4.5. Direct writing + photolithography. Direct writing is amenable to depositing colloidal ceramic slurry on the substrate. Based on the preliminary testing and data from other researchers [65], the viscosities of the slurries are varied leading to inconsistent width at different line segments. From the Melanie Kuhn‘s study, it has been observed that the variance of anode line width was around 14.8μm and the variance of cathode line width was around 7.8μm. This is a major limitation of the direct-writing method where it is difficult to reduce the gap between the electrodes to less than 10μm. Based on to the above mentioned limitation, two approaches are proposed. The first is to prepare homogeneous slurry and further study its rheological properties. The other approach includes restraining the flow of the slurry by building constraining structures using photolithography that prevent the slurry diffusion. Also, as for existing of the constraining wall, it is possible to deposit the multilayer electrode in a single line.

Photolithography will be used to generate the photoresist wall-like constraining pattern on the electrolyte substrate. Depending on the photoresist choice, the wall height

can be as high as to 100μm. The width of the electrodes is to be designed as 100μm-150 μm. The gap between the electrodes can be as low as 10-15μm. Figure 3.9 schematically illustrates the major process using the photolithography and direct-writing process. This procedure includes the following steps.

1) Prepare the electrolyte substrate.
2) Using photolithography create the anode pattern on the substrate.
3) Prepare the anode slurry.
4) Direct write the anode slurry into the photoresist cavity.
5) Pre-dry the slurry at low temperature.
6) Lift off the photoresist.
7) Anneal the anode material.
8) Use photolithography.
9) Create the cathode pattern on the substrate.
10) Prepare the cathode slurry.
11) Direct write the cathode slurry into the photoresist cavity.
12) Pre-dry the slurry at low temperature.
13) Lift-off the photoresist.
14) Anneal the cathode material.
15) Glue the platinum wire on the electrodes sides.
16) Anneal the material.
17) Test the fuel cell.

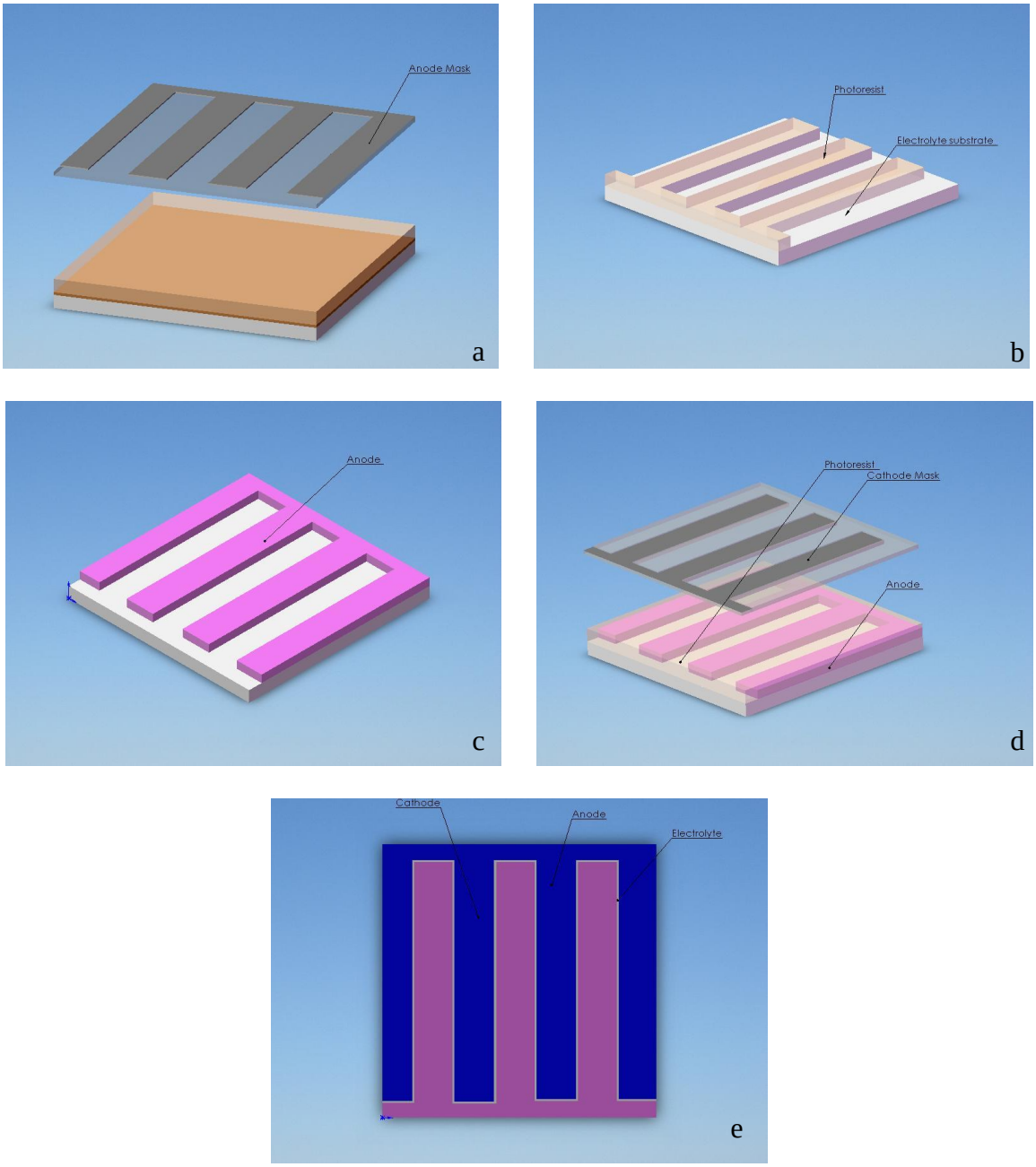

Figure 3.9. Schematically illustrates hybrid photolithography and direct writing. (a) Coat the photoresist on the electrolyte substrate; (b) Use the photolithography generate the anode pattern on the electrolyte substrate; (c) Direct write the anode material into the no photoresist space, lift off the photoresist, and sintering the sample; (d) Coat the photoresist on the (c) sample, and using the photolithography generate the cathode pattern on the (c) sample; (e) Direct write the cathode material into the no photoresist space, lift off the photoresist, and sintering the sample.

Based on the above principle the photoresist slurry can be written for multiple layers. In this design, the thickness of the anode and cathode will increase, and the width will be kept to 150μm accurately. This research provides a novel manufacturing concept to fabricate high quality and repeatability SOFC by combining the photolithography method and direct writing method.

CHAPTER 4

Results

4.1. Results for EBL + PLD Process

EBL is a reliable technique to create the nano-sized features directly on the substrate. Its advantages have been stated in the section 3.2.1 and the process was illustrated in the section 3.4.1. The Elionix ELS-7500 EX E-Beam Lithography System at Duke University (as shown in Figure 4.1) was used for this research. ELS-7500EX is capable of producing ultra fine features down to a 10 nm line width [66].

Figure 4.1. Elionix ELS-7500 EX E-Beam Lithography System [66]

To optimize speed, the resist sensitivity should be high; beam current should be large; beam overlapping should be small (low pixel count), and exposure field should be large [67]. Based on this requirement, 50nA Beam current, a scan rate of 60µsec/step were chosen to obtain a minimum line width of 10nm. The maximum field size the system provides is 1200µm. However the stitching and overlay error is around 150nm. For the 10mm x 10mm design in this research the field size was chosen around to 600µm which resulted in a stitching and overlay error of around 50nm [67]. PMMA 495K and PMMA 950K resist were chosen. PMMA is most commonly used as a high resolution positive resist for EBL [68]. Total thickness of resist film was around 1~2µm.

However, even though suitable parameters were chosen to optimize the speed, the operating speed was still slow. To write a 10mm line with 10µm width using the EBL takes more than 2 hours to complete. On the other hand, since the field size is only 600µm, for the chosen design, there are at least 17 fields that need to be stitched together for a single line. The stitching errors were magnified. Figure 4.2 shows the micrograph of the EBL process fabrication result.

Figure 4.2. EBL field stitching error

From the optical microscope, it was observed that the stitching error was much larger than 50nm, even though stitching alignment process was conducted. Thus, based on the above described limitations this process was not pursued for μ-SC-SOFC fabrication.

4.2. Results for Soft lithography + Photolithography Process

The mask for photolithography shown in Figure 3.3 was prepared with different feature sizes. The widths of the electrolyte were 10μm, 15μm, and 20μm respectively. Figure 4.3 shows the aluminum die for the PDMS mold. It is fabricated in the CNC milling machine. The inside square covers the outside square in Figure 3.3.

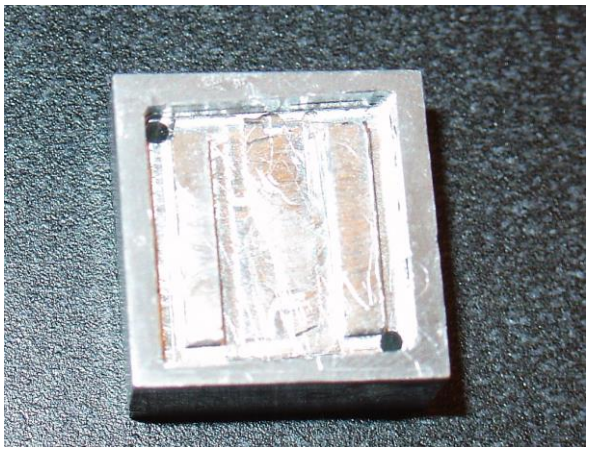

Figure 4.3. Aluminium die

However, this method had very low repeatability. Making the precise PDMS mold was a challenge. Issues of evacuating the mold from bubbles and ensuring pattern

replication on the mold remain to be resolved. In addition, soft lithography is suitable for the low viscosity slurry. Slurry having good fluidity makes it easy to move into the very thin mold channels. However, after sintering, the shrinkage rate is high and crack formations are difficult to avoid. After initial testing using this method, it was decided to investigate other fabrication methods. Figure 4.4 shows one of PDMS molds. The bubbles destroyed the integrity of the mold.

Figure 4.4. PDMS mold

4.3. Results for PLD + Photolithography Process

This section describes different results obtained using the combination of two processes: photolithography for micro pattern generation and PLD for material deposition. Results for the following fabrication steps are explained below.

1) Prepare substrate.
2) Prepare PLD targets.

3) Parameter research.

4) Design photolithography mask.

5) Fabricate μ-SC-SOFC.

4.3.1. Substrate preparation. In order to keep the deposition surface flat the Al_2O_3 substrate was polished. Dark brown colored Si_3N_4 thin film was deposited on the Al_2O_3 substrate by Magnetron sputtering. The deposition of a dark color thin film was conducted to reduce the reflectivity of the white Al_2O_3 wafer, which was cut to 20mm x 20mm dimensions. The thickness of thin film was around 300nm.

4.3.2. PLD target preparation. Both anode and cathode PLD targets were prepared from powders. The electrolyte material was composed of 1mol% CeO_2, 10 mol% Sc_2O_3 and 89 mol% ZrO_2 (Ce-ScSZ). The anode material consisted of 60 wt% NiO and 40 wt% YSZ and the cathode material was LSCF. The average particle sizes of the electrolyte powders were around 50 nm. The average particle sizes of anode and cathode powders were around 50nm and 500nm, respectively. All powders were pressed unitarily at room temperature at 10 tons for 10-15 min. Further, electrolyte and anode powder was baked at 1400ºC for 6 hours and cathode powder was baked at 1250ºC for 4 hours.

In order to evaluate the deposited material's phase characterization, X-ray diffraction was performed. 5000 pulses of electrolyte, anode and cathode materials were deposited with PLD on Si (100) substrate, respectively. XRD spectra in Figures 4.5 and 4.6 show that YSZ (electrolyte) and LSCF (cathode) experienced phase transformations from amorphous crystallography to their corresponding polycrystalline structures.

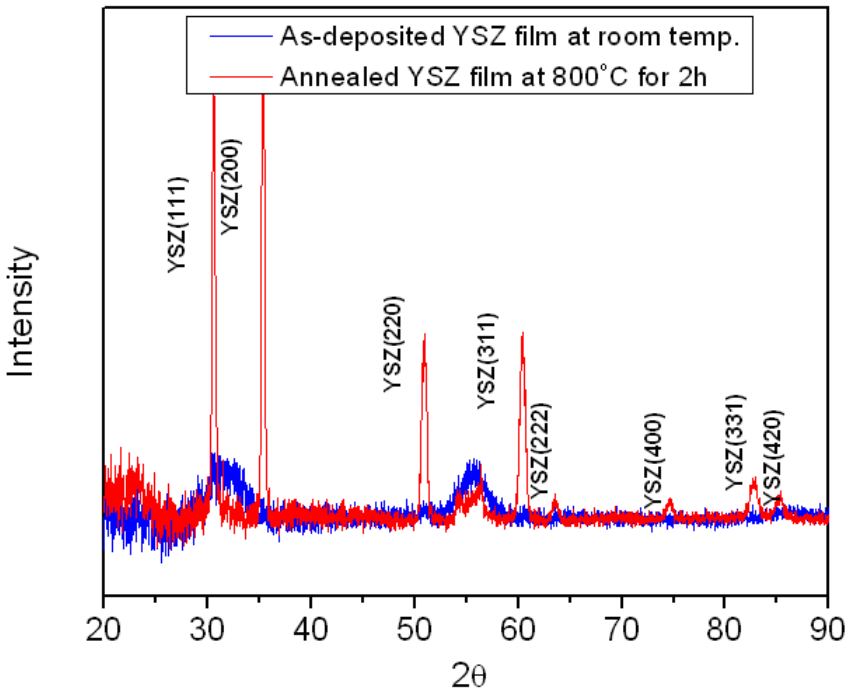

Figure 4.5. XRD spectra of YSZ (electrolyte)

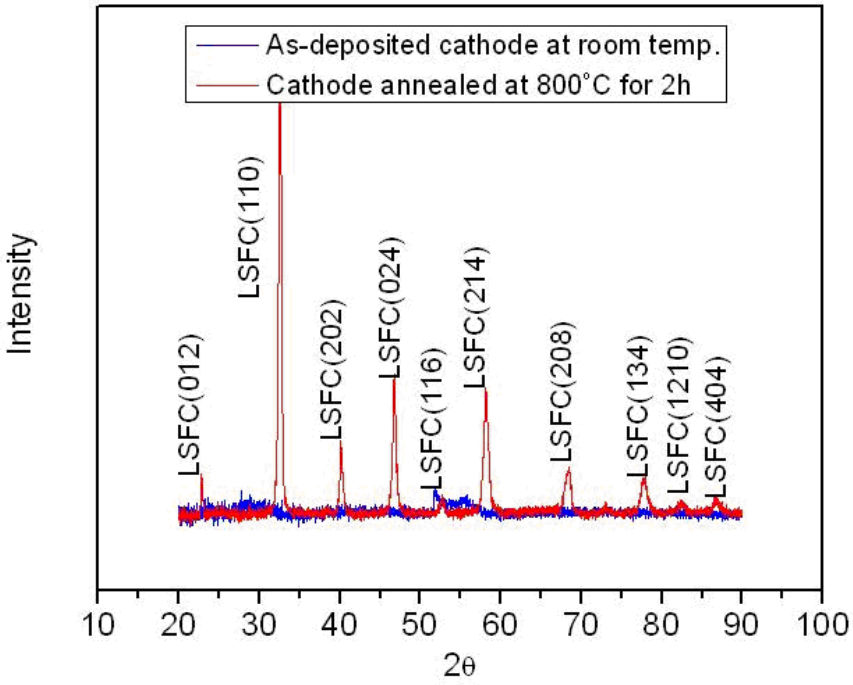

Figure 4.6. XRD spectra of LSFC (cathode)

XRD spectra in Figure 4.7 demonstrate that the as-deposited anode was a composite of amorphous YSZ and NiO. After high temperature annealing and reduction in H_2, cubic phase of YSZ and elemental Ni phase were revealed.

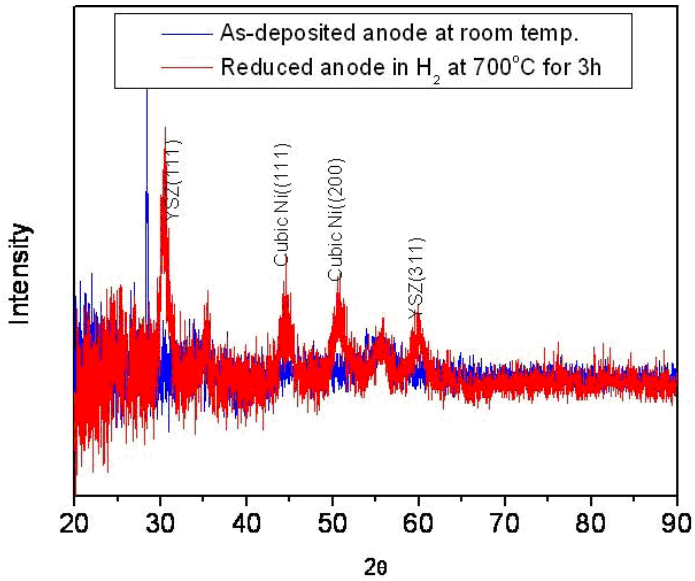

Figure 4.7. XRD spectra of YSZ + NiO (anode)

4.3.3. PLD parameter research. In order to analyze the effects of the deposition pressure, annealing temperature and annealing time on the microstructure of anode and cathode material PLD parameter research was conducted. Table 4.1 shows the operating conditions for LSCF deposition. Four deposition pressures (50, 100, 200, 300 mTorr) are chosen. The samples deposited under different pressure are annealed for 4 and 8 hours separately. The annealing temperature was hold at 800ºC.

Table 4.1. Operating conditions for LSCF deposition

Operating pressure (mTorr)	Annealing temperature (ºC)	Annealing time (h)
50	800	4
50	800	8
100	800	4
100	800	8
200	800	4
200	800	8
300	800	4
300	800	8

A SEM analysis was for observing the effects of parameters including operating pressure, annealing temperatures and annealing time. Figures 4.8 to 4.15 show the SEM images of the top view and cross section of LSCF deposition thin film for 10k pulses under the different operating conditions as shown in Table 4.1.

Based on them, the thin films generated at low operating pressure, 50mTorr and 100 mTorr, were dense. The thin film demonstrates lattice structure. Under 50mTorr,the thickness is around 400nm. Under 100mTorr, the thickness is around 800nm. However, the thin films deposited under these situations did not generate a porous microstructure electrode as desired. Though, the thin films generated at 300mTorr have porous microstructure, there are large crack formations. They are hard to demonstrate the lattice structure. This will lead to high ohmic loss. It was observed that the thin film generated at 200 mTorr operating pressure and sintered at 800°C for 4 hours had a good microstructure. Also, the cross section image for the above deposition condition was around 500nm per 10k pulses.

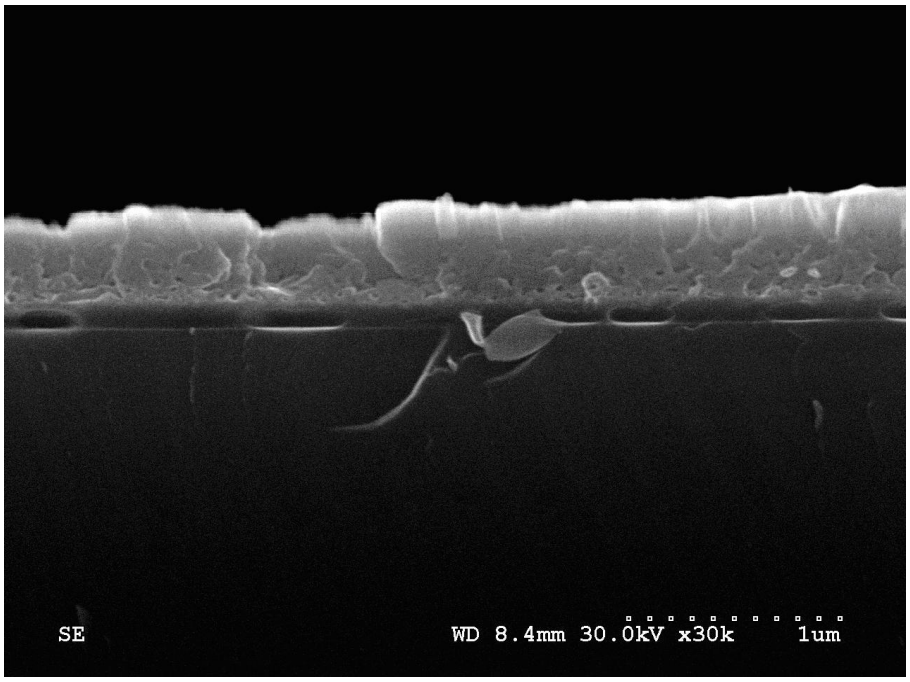

(a)

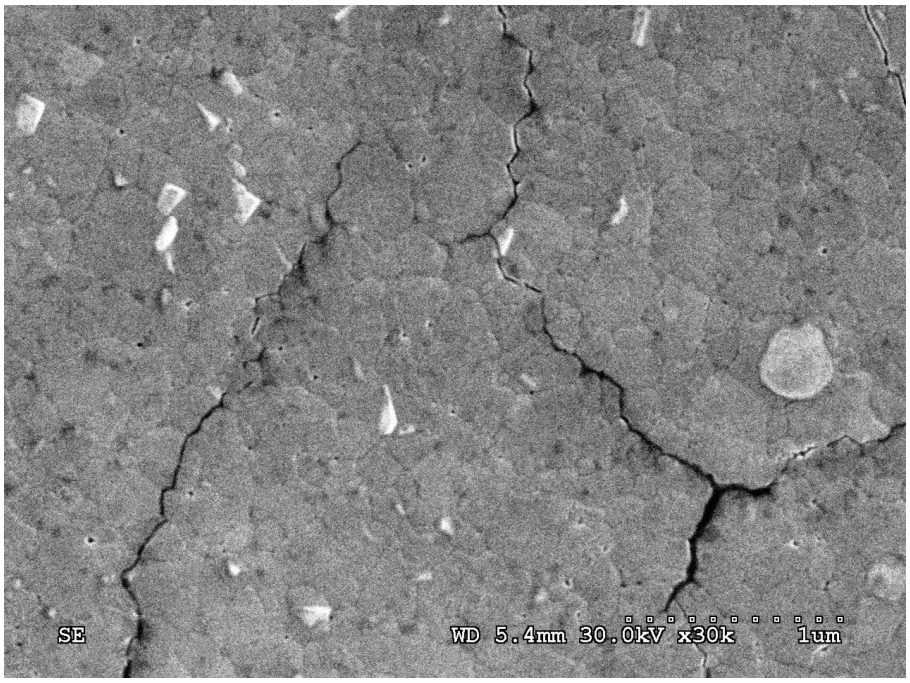

(b)

Figure 4.8. (a) Cross section, (b) Top view of the LCSF film which deposited under operating pressure 50mTorr, sinter temperature 800°C and annealing time 4 hours. The thickness is around 400nm. This structure is dense but has crack. The thin film demonstrates lattice structure.

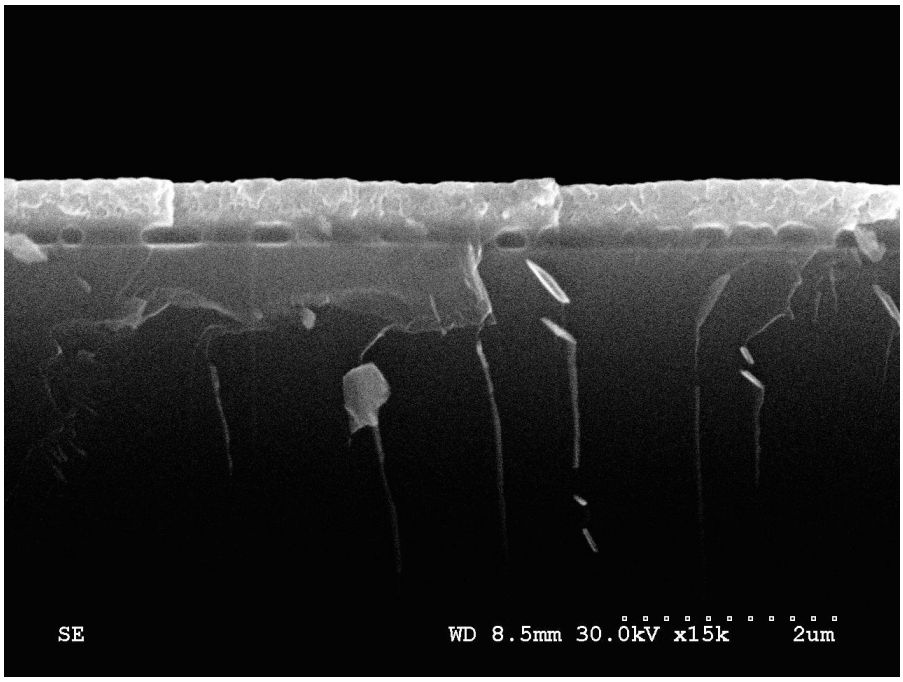

(a)

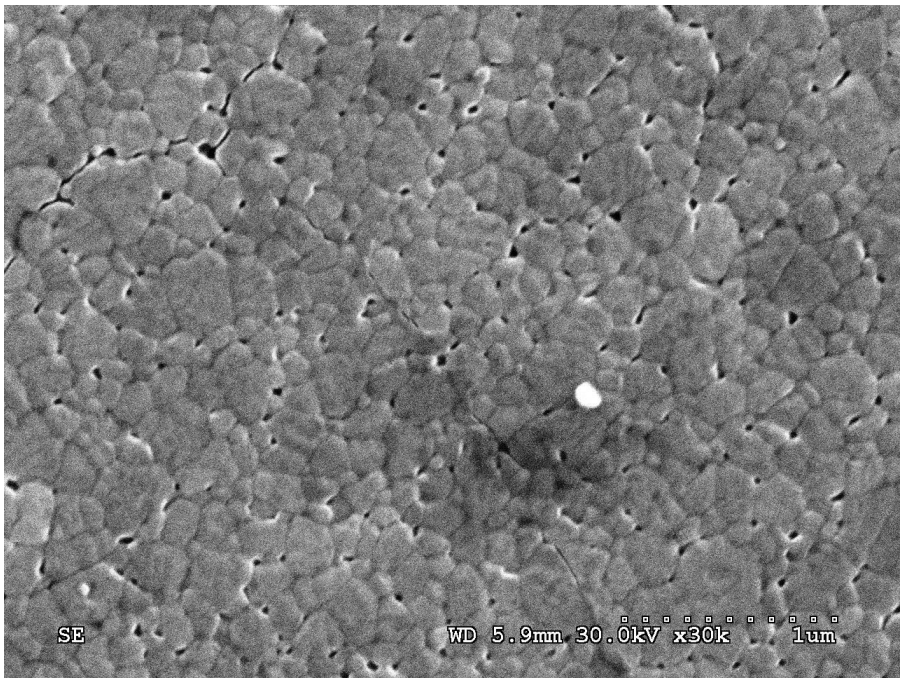

(b)

Figure 4.9. (a) Cross section, (b) Top view of the LCSF film which deposited under operating pressure 50mTorr, sinter temperature 800°C and annealing time 8 hours. The thickness is around 400nm. This structure has few pinholes but dense. The thin film demonstrates lattice structure.

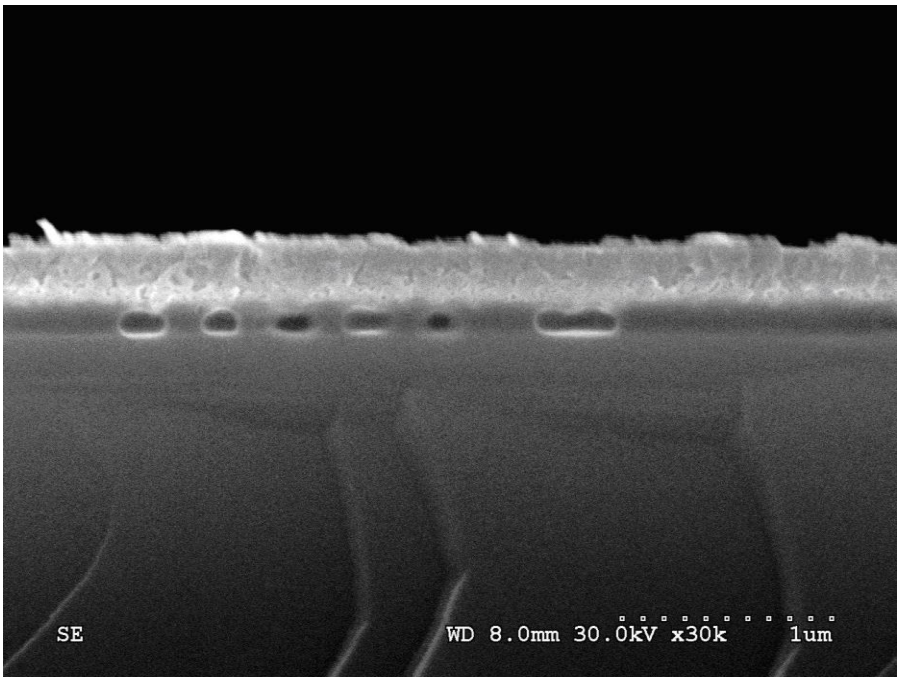

(a)

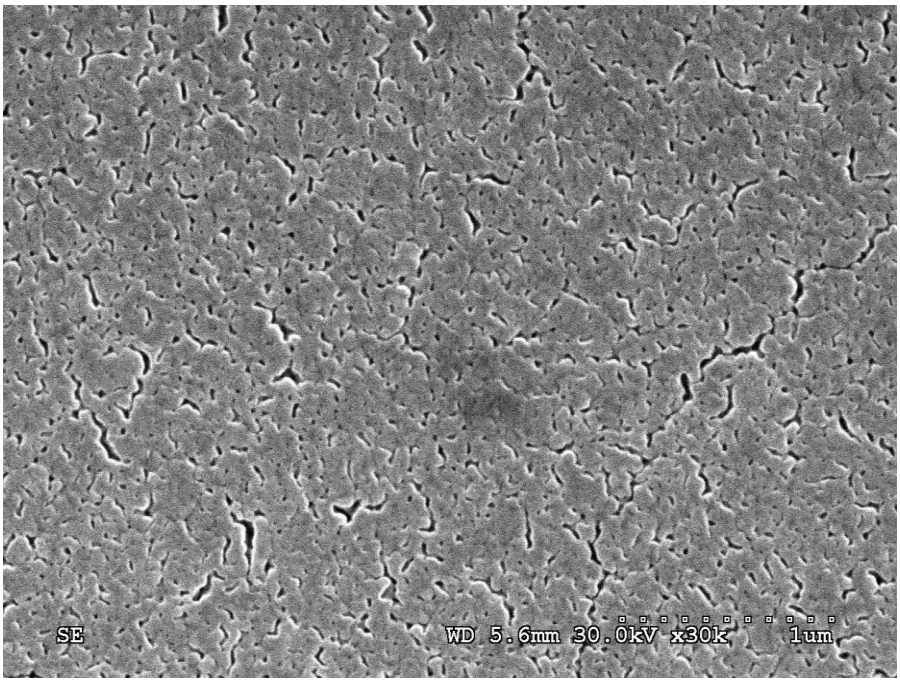

(b)

Figure 4.10. (a) Cross section, (b) Top view of the LCSF film which deposited under operating pressure 100mTorr, sinter temperature 800°C and annealing time 4 hours. The thickness is around 400nm. This structure has some pinholes.

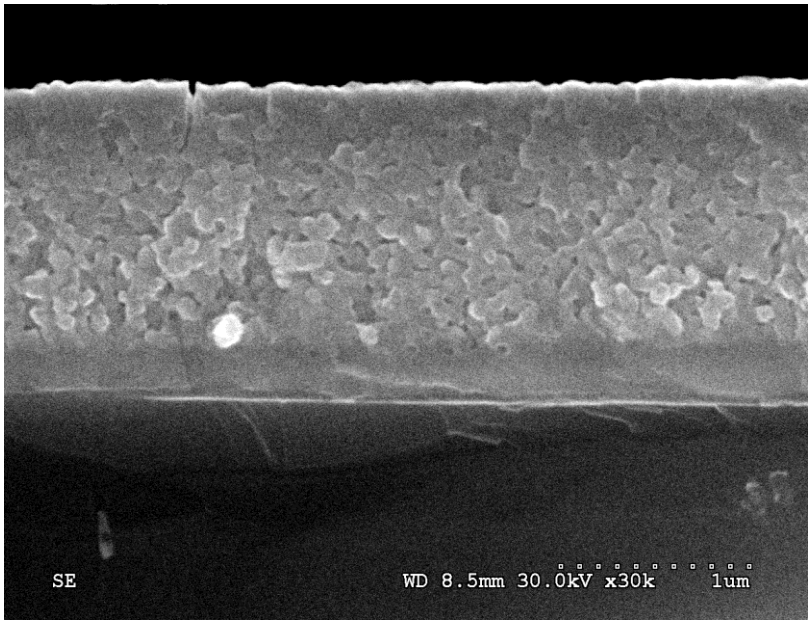

(a)

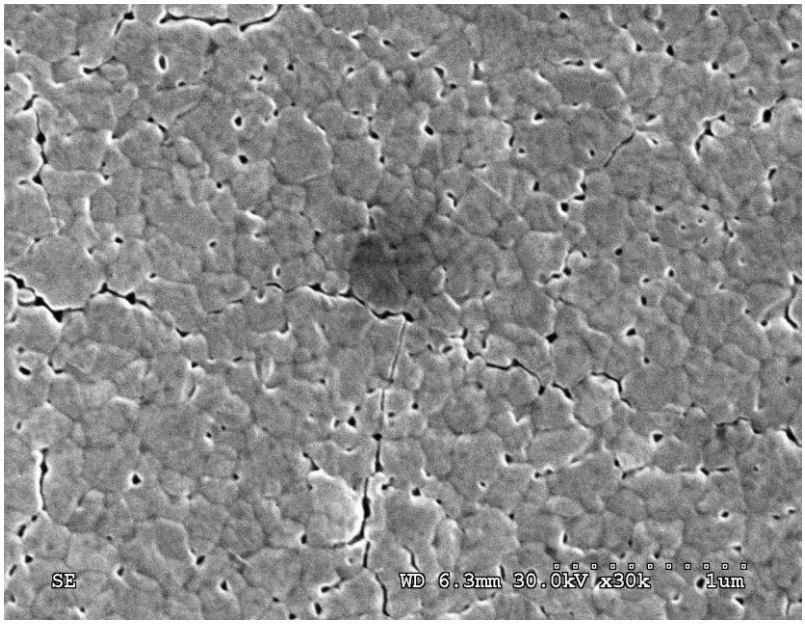

(b)

Figure 4.11 (a) Cross section, (b) Top view of the LCSF film which deposited under operating pressure 100mTorr, sinter temperature 800°C and annealing time 8 hours. The thickness is around 800nm. This structure is still dense, but the bottom of the thin film has some porous structure and thin cracks. The thin film demonstrates lattice structure.

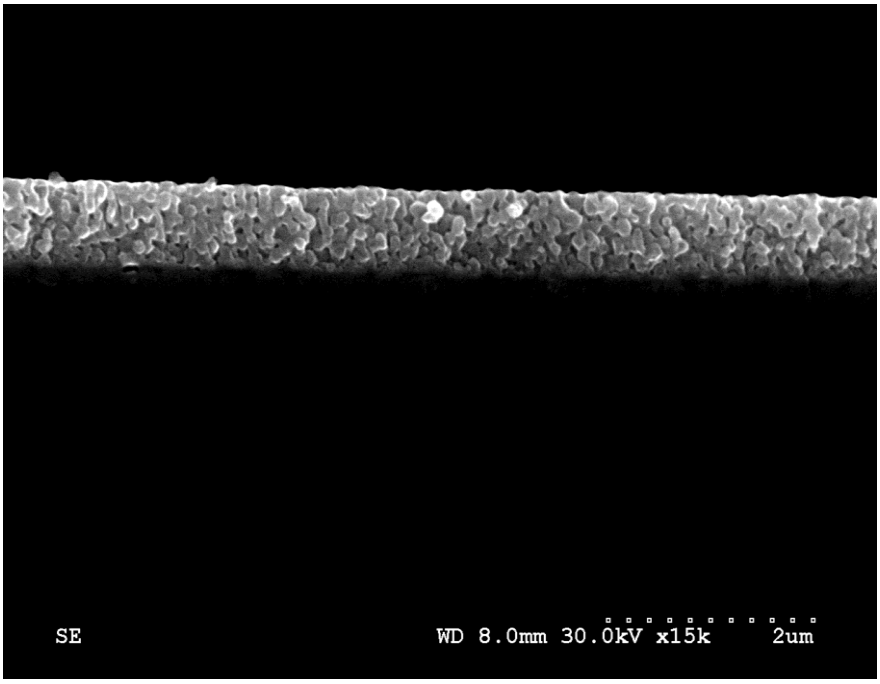

(a)

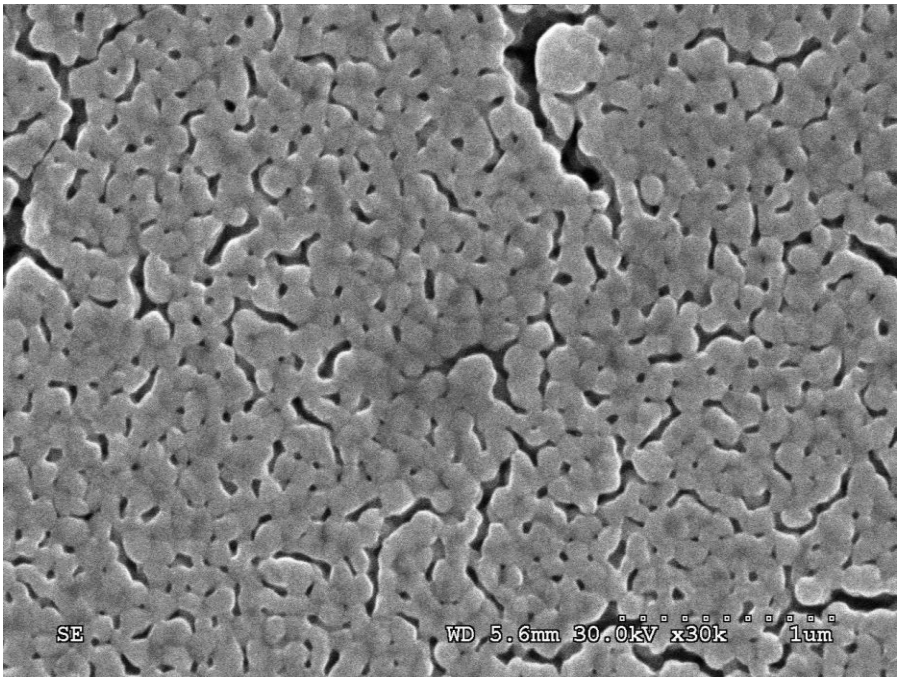

(b)

Figure 4.12 (a) Cross section, (b) Top view of the LCSF film which deposited under operating pressure 200mTorr, sinter temperature 800°C and annealing time 4 hours. The thickness is around 800nm. This structure is porous structure and bigger cracks. Lattice structure is not very clear.

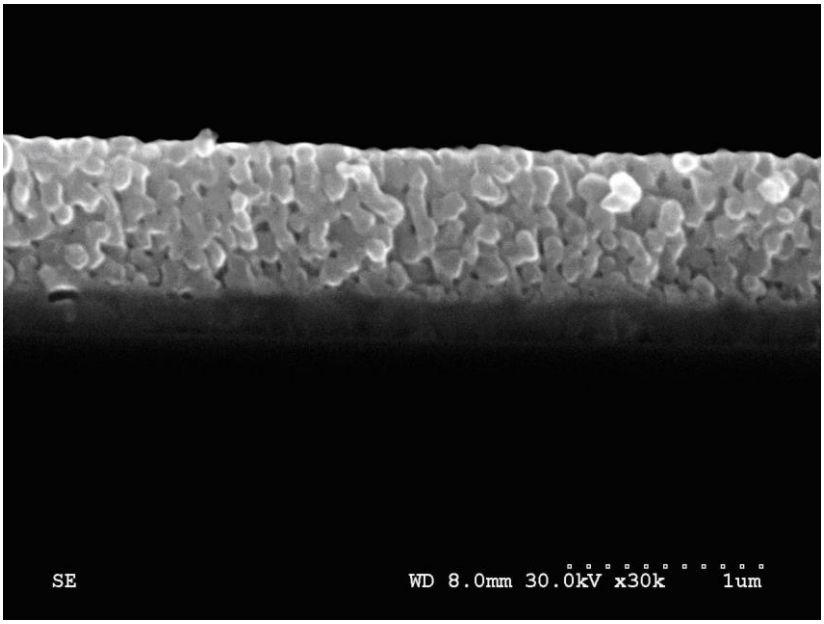

(a)

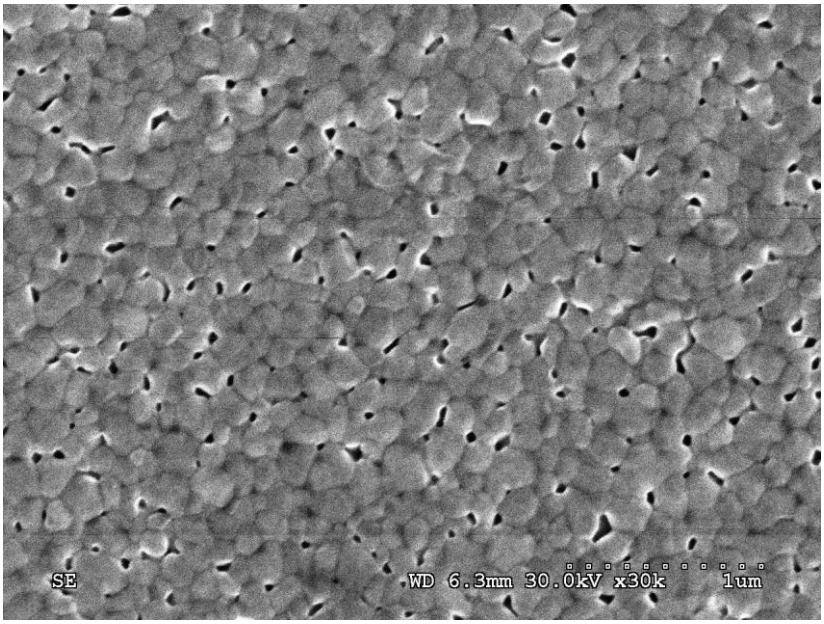

(b)

Figure 4.13. (a) Cross section, (b) Top view of the LCSF film which deposited under operating pressure 200mTorr, sinter temperature 800°C and annealing time 8 hours. The thickness is around 800nm. This structure is porous structure and thin cracks. The thin film demonstrates lattice structure.

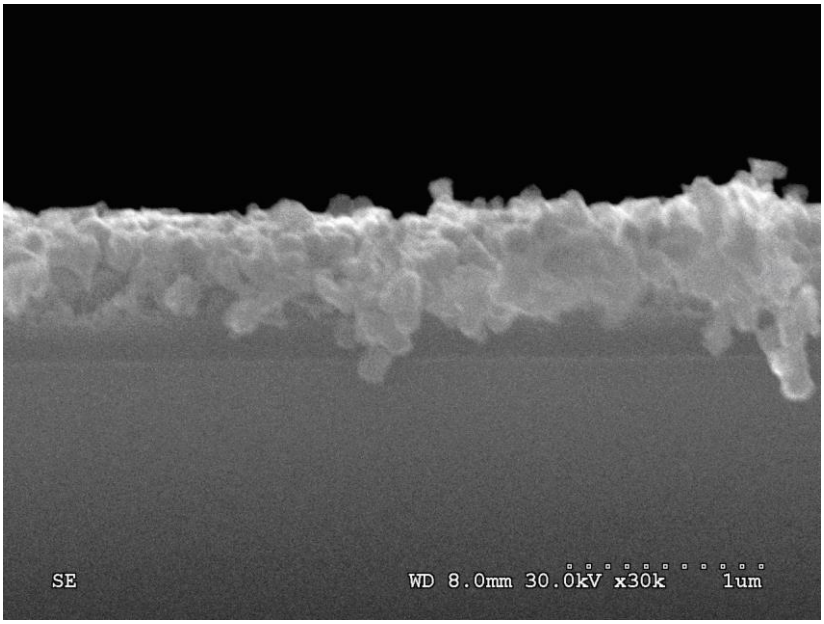

(a)

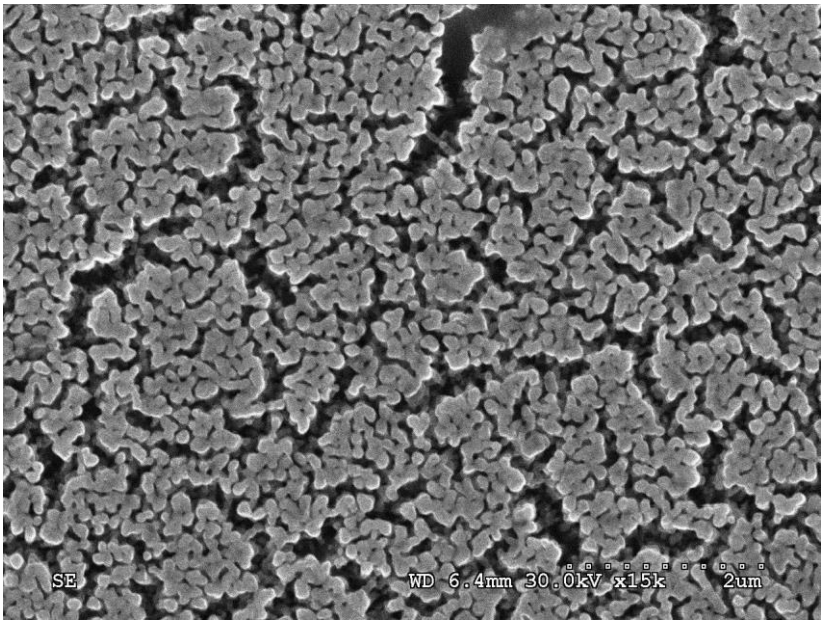

(b)

Figure 4.14. (a) Cross section, (b) Top view of the LCSF film which deposited under operating pressure 300mTorr, sinter temperature 800°C and annealing time 4 hours. The thickness is around 500nm. This structure is porous structure and large cracks. It is hard to demonstrate the lattice structure.

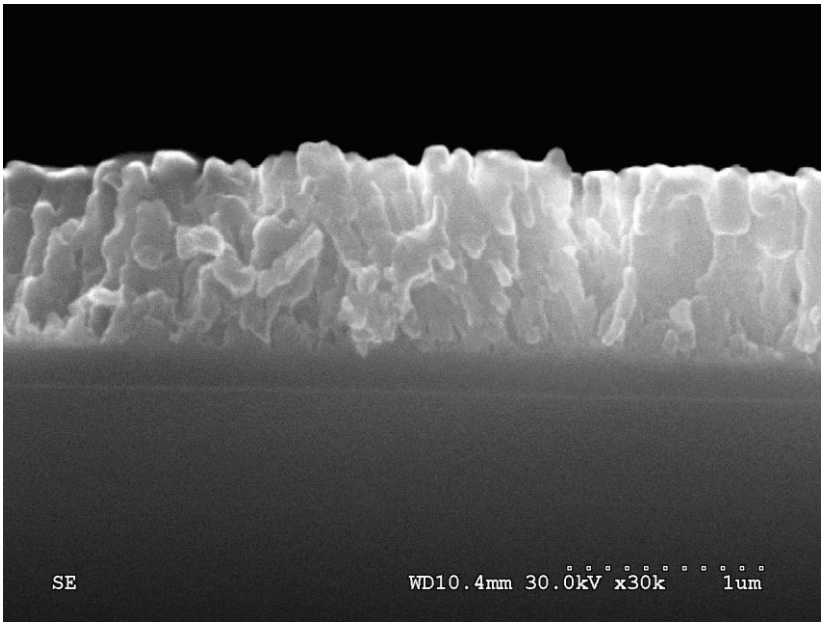

(a)

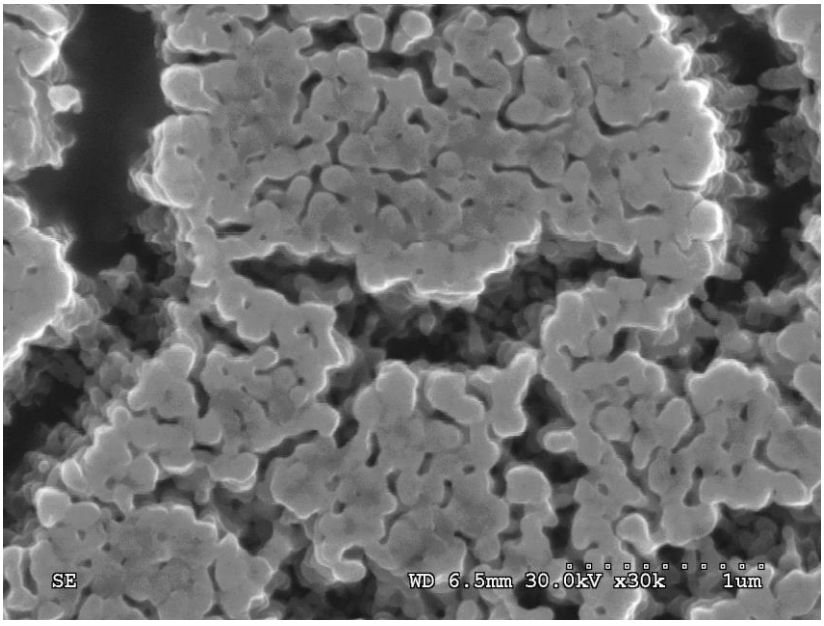

(b)

Figure 4.15. (a) Cross section, (b) Top view of the LCSF film which deposited under operating pressure 300mTorr, sinter temperature 800°C and annealing time 8 hours. The thickness is around 800nm. LSCF Powder has been sintered to large area. This structure has large cracks.

Figures 4.16, 4.17 and 4.18 show the SEM images of the top cross section of YSZ deposition thin film for 20k pulses. Based on LSCF experiments and prior work in the field it was hypothesized that dense thin film can be generated at low operating pressures. Thus, the operating pressure was set at 15 mTorr. It was observed that at 15 mTorr, 600°C and 2 hour annealing period a dense electrolyte thin film was formed. However, at 15 mTorr, 400°C and 2 hour annealing period a columnar microstructure was formed, which is suitable for the conventional planar SOFC. Thus, by means of controlling the sintering temperature and time, the desired microstructure can be achieved.

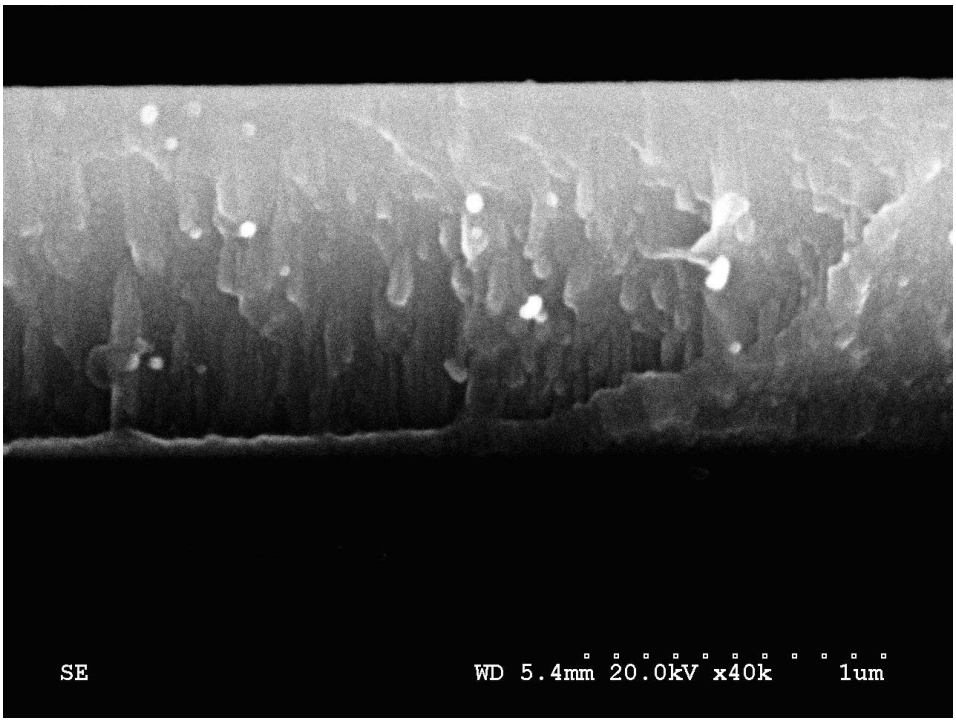

Figure 4.16. Cross section of the YSZ electrolyte thin film which deposited under operating pressure 15mTorr, sinter temperature 350°C and annealing time 2 hours. This structure is dense. The thickness is around 800nm.

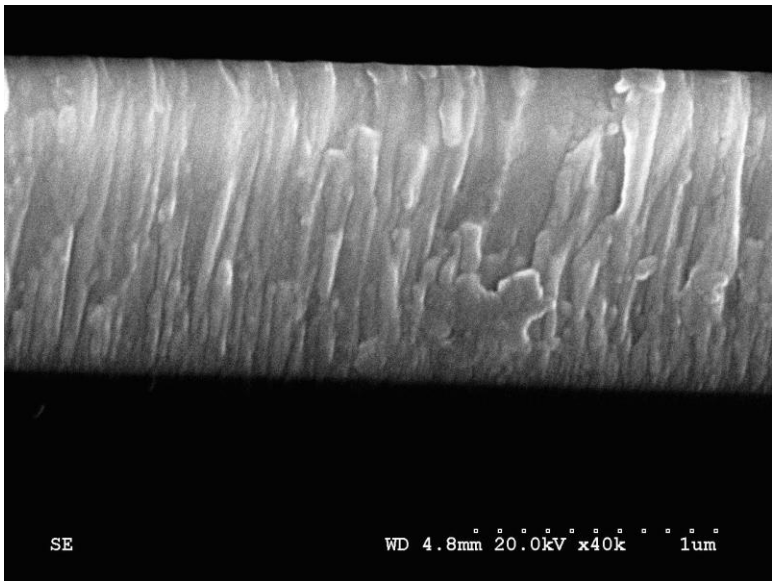

Figure 4.17. Cross section of the YSZ electrolyte thin film which deposited under operating pressure 15mTorr, sinter temperature 400°C and annealing time 2 hours. This structure is dense. The thickness is around 800nm.

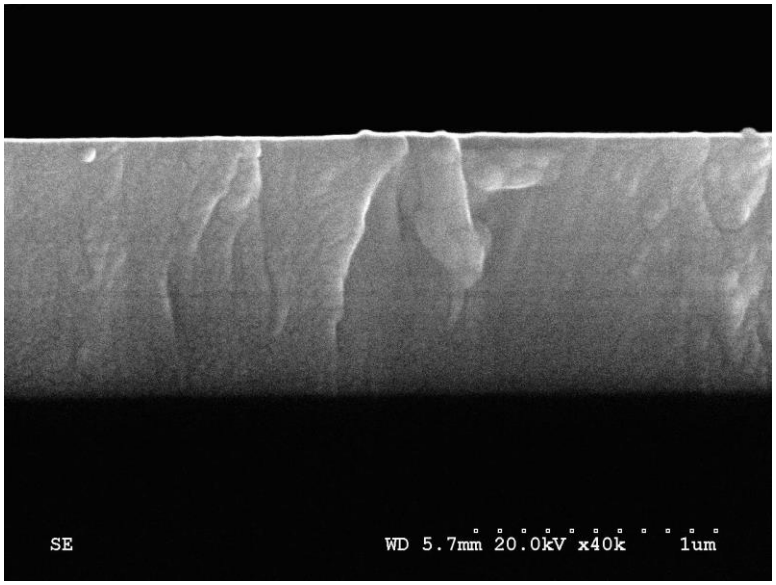

Figure 4.18. Cross section of the YSZ electrolyte thin film which deposited under operating pressure 15mTorr, sinter temperature 600°C and annealing time 2 hours. This structure is dense. The thickness is around 800nm.

4.3.4. Photolithography masks design. In order to improve the electrical contact of the electrolyte and electrodes, 3µm overlaps of electrodes on electrolyte walls were designed. Furthermore, alignment was carefully carried out while generating the electrode patterns. The masks were designed as shown in Figures 4.19 to 4.21. During this design, the widths of electrode were varied from 50 µm, 100 µm, to 150 µm. The widths of electrolyte were varied from 5um, 10 µm, 15 µm, to 20 µm. In total there were 12 sets of masks prepared for SC-SOFC.

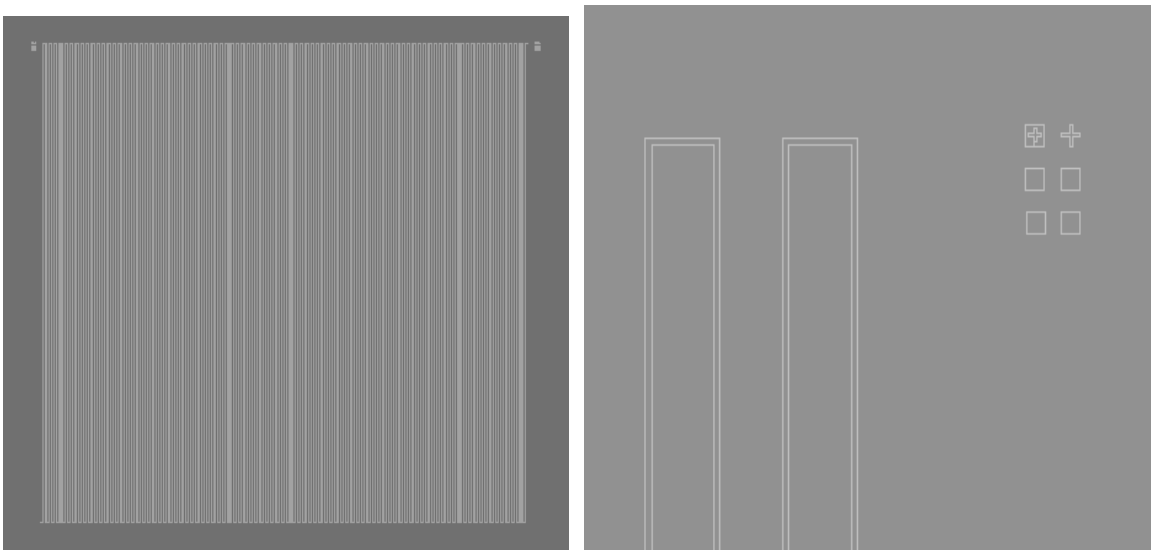

(a) (b)

Figure 4.19. (a) Electrolyte pattern mask; (b) Electrolyte pattern mask detail design and alignment marks.

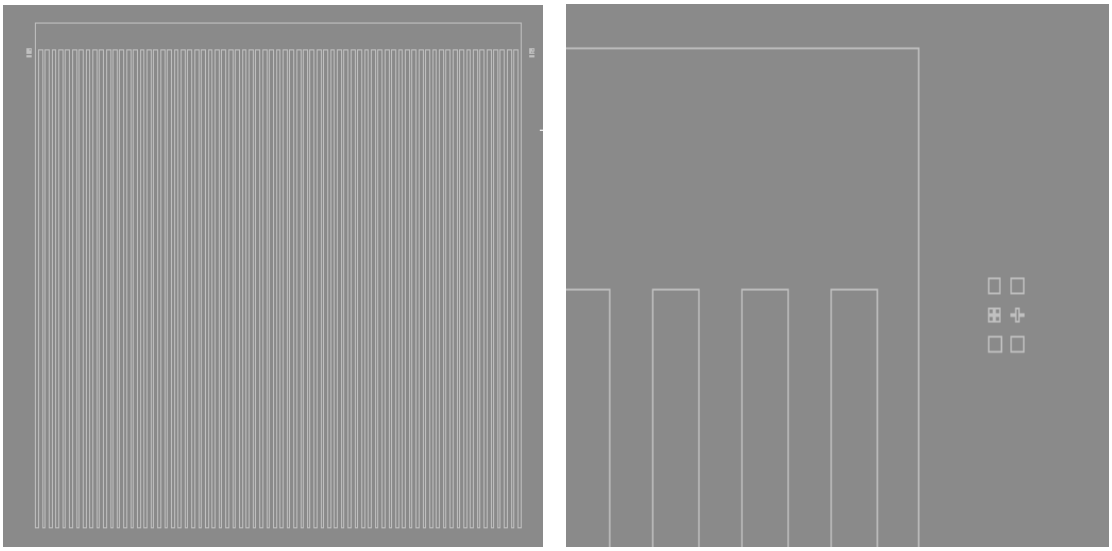

(a) (b)

Figure 4.20. (a)Cathode pattern mask; (b) Cathode pattern mask detail and alignment marks

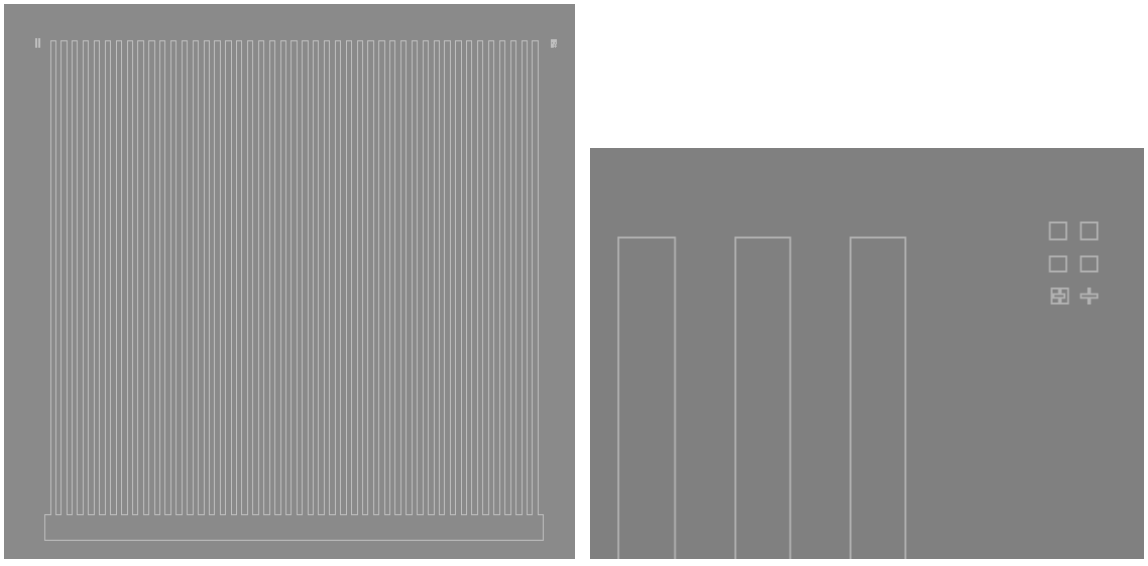

(a) (b)

Figure 4.21. (a) Anode pattern mask; (b) Anode pattern mask detail and alignment marks

Figure 4.22 shows the anode photoresist pattern with overlap between electrolyte wall and anode pattern. On the top of pattern, the alignment marks were matched, exposed and developed during the process. However, in the processing the initial overlap area increased. The initial ~3 µm increased to ~ 6 µm. Based on this finding further investigation is needed to understand effect of photoresist parameters, mask parameters, and process parameters on the pattern geometry. In section 4.3.5, fundamental research on photoresist and photolithography process will be carried out.

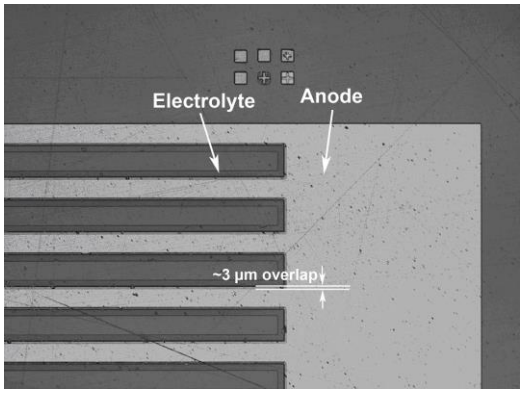

Figure 4.22. Anode photoresist pattern under optical microscope

4.3.5. Photoresist and photolithography process research. During this research, Futurrex NR9-8000 negative photoresist was applied. It is designed for thick film applications and is compatible with UV exposure tools emitting at the 365 nm exposure wavelength, including wafer steppers, scanning projection aligners and proximity printers and contact printers. Resist was developed in resist developer RD6 by spray or immersion at 20-25°C and using water to stop developing. After drying the resist,

resist remover RR4 or acetone was used to remove of resist [69]. NR9-8000 is one of popular negative photoresist for the thick film recently. However the process characterization of this photoresist has limitations.

4.4. Results for Direct Writing

The key research tasks for manufacturing SOFC using direct writing include: (1) Prepare electrolyte substrate. (2) Prepare electrodes slurry. (3) Optimize direct writing systems parameters.

4.4.1. Electrolyte substrate preparation. In this research, the substrate was made of 66% YSZ (particle size 55nm) and 34% YSZ (particle size 5-10 nm). The electrolyte substrate was pressed at 10000 lb for 5 minutes and sintered at 1350°C for 10 hours. After sintering, the substrate surface was polished using 180, 360 600 sand papers under 12 tons for 15 min each. SEM machine was used to check the lattice structure of the electrolyte substrate. Figure 4.23 and 4.24 show the micro structure of the electrolyte substrate. According to the figures, the powders have been sintered to form a crystallographic structure, but the surface is not smooth enough. To overcome the surface roughness the surface will be polished under 180, 360, 600, 800 sand papers under 15tons for 30 min each.

4.4.2. Electrode slurry preparation. Slurry preparation is the most important and challenging step for the direct-writing process. The viscosity of the slurry affects the choice of the writing pressure, writing velocity, and writing distance between the nozzle

and the substrate. Viscosity also has an influence on the widths of electrode deposited on the substrate and the shape of the structure after sintering.

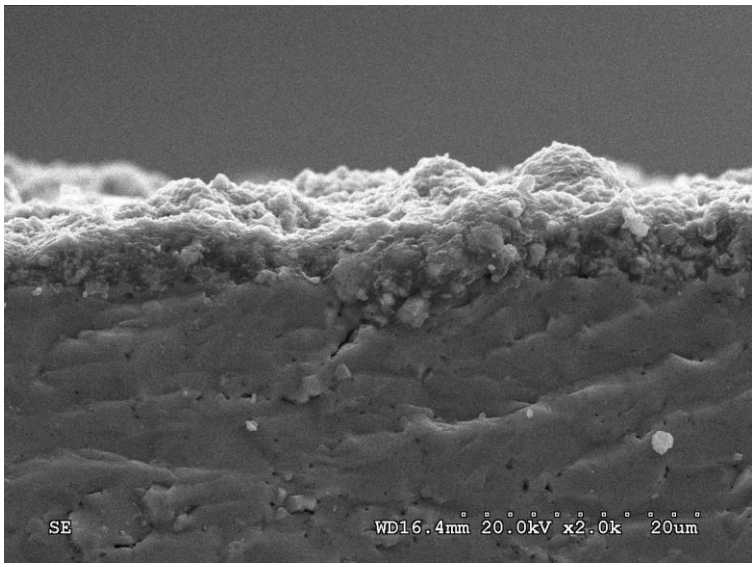

Figure 4.23. Cross section of the electrolyte substrate

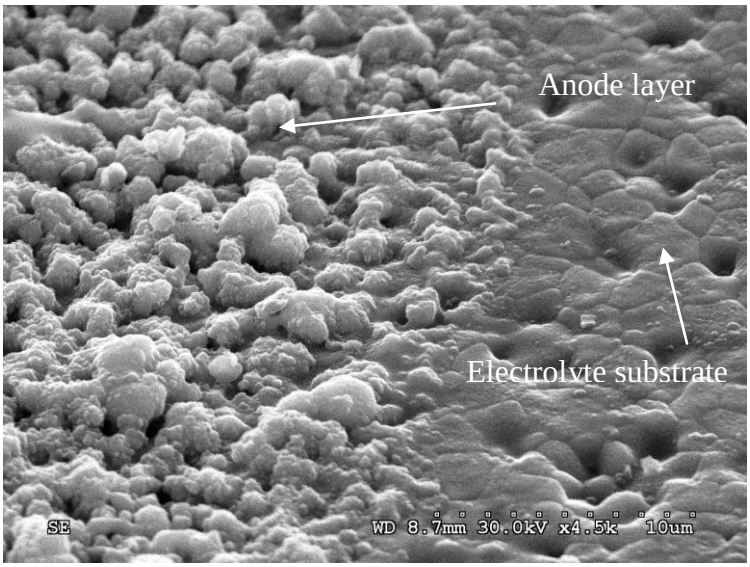

Figure 4.24. Top view of the electrolyte substrate and anode layer

The anode material consisted of 60wt% NiO and 40wt% YSZ (8 mol% YSZ, particle size 55nm). For anode slurry, anode powders were mixed with organic solvent α-Terpineol. Solid loading was between 35wt% - 50wt%. Triton X-100 was used as a dispersant with a range between 1% - 1.5%. The mixture was prepared by ball milling in Spex Mixer/Mill (Spex 800 M). After 1 hour milling, around 10% - 15% binders, polyvinyl butyral (PVB) was added and milled for another hour. The viscosity of slurry was around 25000~35000 cps. The cathode material consisted of LSCF. The slurry was prepared in the similar way to prepare the anode slurry. The viscosity was around 2000~35000cps.

Figure 4.25 shows the top views of lines written by the different concentration ration of anode slurries. For those lines written by the low solid loading concentration (Figure 4.25-a), there are a lot of thin anode islands on the surface. For those lines written by the low binder concentration (Figure 4.25-b), there are a lot of thick anode isloands on the surface. The line written by the slurry with 50% solid loading and 1% dispersant and 15% binder (Figure 4.25-c) has some island. The line written by the slurry with 50% solid loading, 1% dispersant and 12% binder (Figure 4.25-d) has porous micro contracture without island.

Figure 4.26 shows the cross section of lines written by the slurry with high solid loading concentration (50%). These figures show that nano powders are sintered together. The line has a good shape and the line thickness is around 10-15μm. The anode line written by the slurry with 12% binder has better shape than that with 15% binder. Figure 4.27 shows the top view and cross section of the LSCF line written by the slurry with

50% solid loading, 1% dispersant and 15% binder. The line thickness is less than 10μm. Nano powders are sintered together. The printed line has a good shape. The printed line has porous microstructure without island.

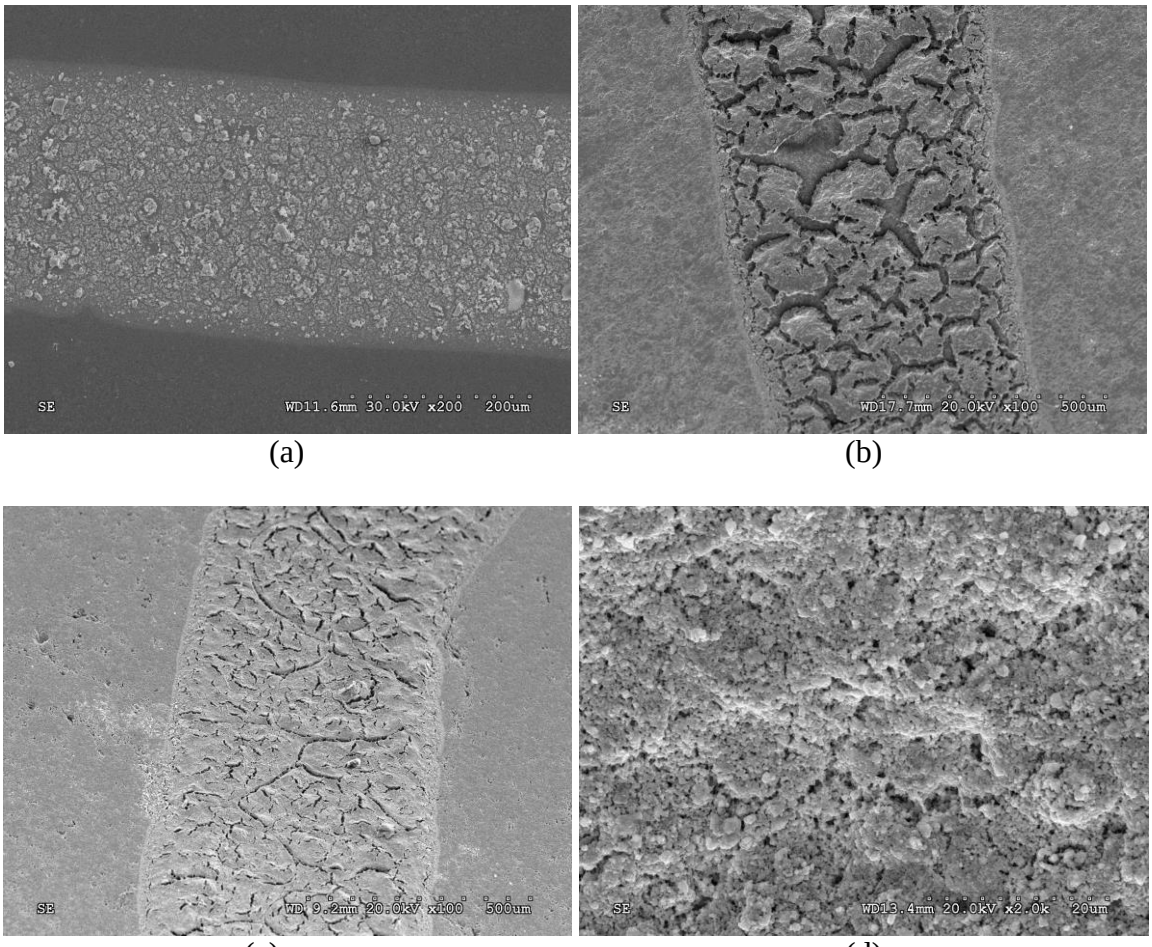

Figure 4.25. Top view of line written by the slurry with (a) 35% solid loading, 1% dispersant, and 20% binder; (b) 50% solid loading, 1.5% dispersant, and 8% binder;(c) 50% solid loading, 1% dispersant, and 15% binder; and (d) 50% solid loading, 1% dispersant, and 12% binder.

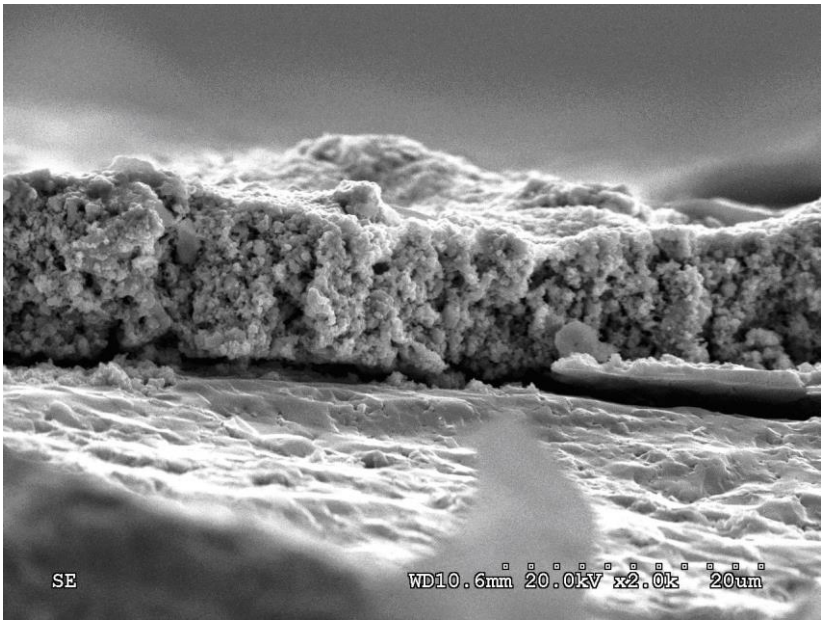

(a)

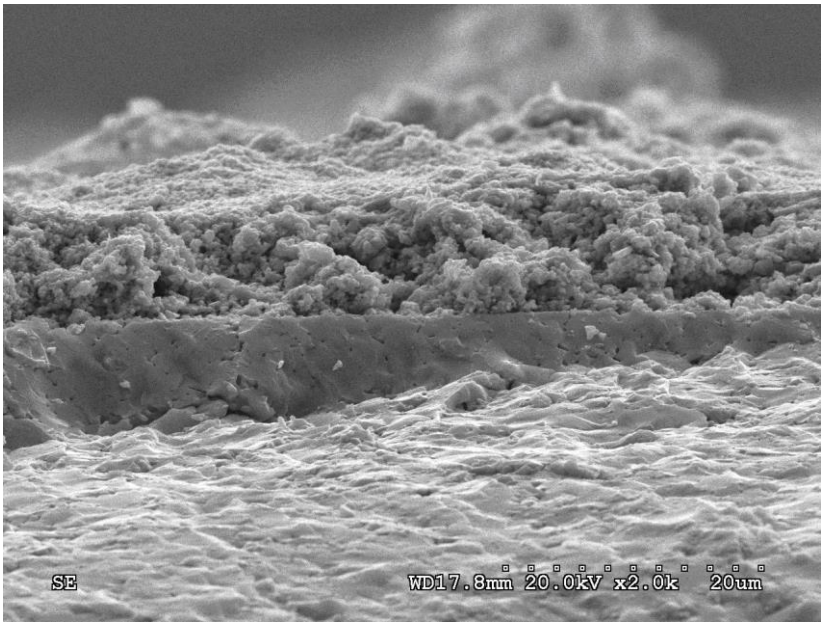

(b)

Figure 4.26. Cross section of anode lines (a) written by the slurry with 50% solid loading, 1% dispersant and 12% binder; and (b) written by the slurry with 50% solid loading, 1% dispersant and 15% binder

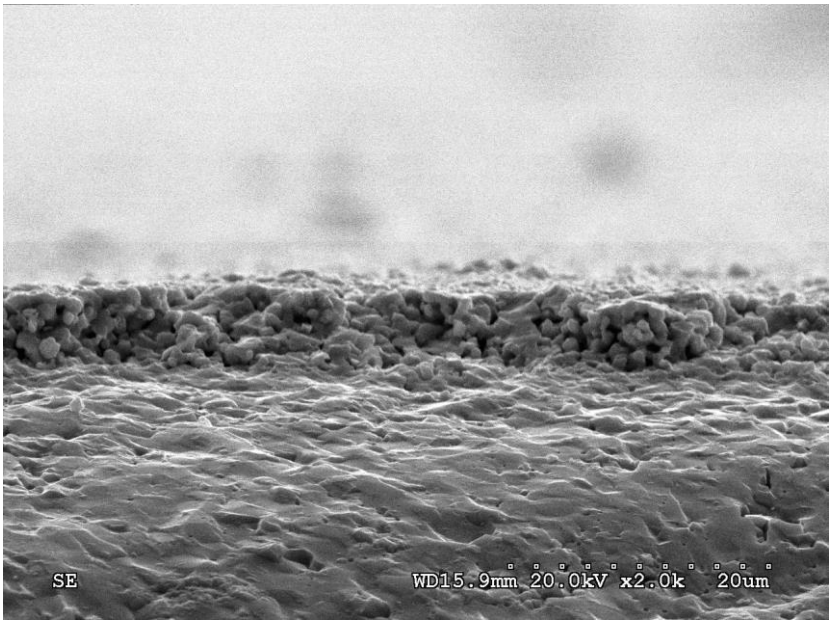

(a)

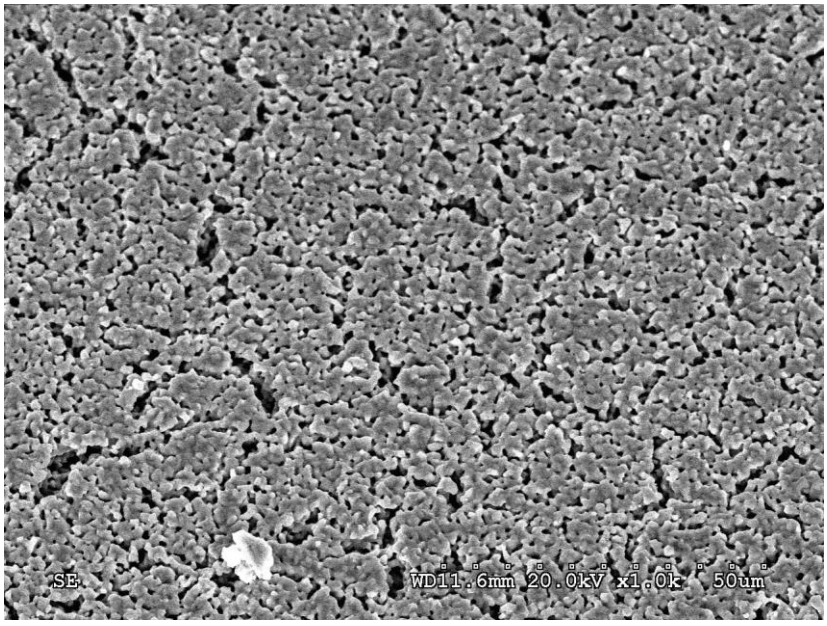

(b)

Figure 4.27. (a) Cross section and (b) top view of LSCF direct writing lines. The line thickness is less than 10μm. Nano powders are sintered together. The printed line has a good shape. The printed line has porous microstructure without island.

4.4.3. Microstructure evaluation for direct writing features. Using the direct-write setup anode and cathode lines were written on the electrolyte substrate. After sintering, these lines SEM observation was carried out to evaluate the microstructure. Based on SEM images, the anode and cathode lines were generated.

1) If the binder's concentration was less than 10%, the deposited pattern lines may develop large cracks. 12% was the optimal ratio to obtain the desired pattern.
2) For the current system using a 100 μm nozzle, 50% solid loading of anode material was the highest ratio that could be extruded.
3) For the cathode slurry, 50% solid loading, 1% dispersant and 15% binder can generate good line patterns with appropriate porous and continuous micro structure. In the chapters 6 and 7, the conductivity of cathode pattern lines will be evaluated.

4.5. Summary of Preliminary Results

In the previous chapters, several approaches to fabricate the μ-SC-SOFC are discussed and preliminary results were shown. Among these approaches, direct writing method allows one to design and rapidly fabricate ceramic materials in complex 3D shapes without the need for expensive tooling, dies or lithographic masks. Furthermore, direct writing can be combined with photolithography method to improve the direct writing pattern's quality. In the following chapters, the direct writing method will be studied in further detail.

4.5.1. Direct writing slurry analysis. Ceramic slurries were composed by electrode powder, binder, dispersant and solvent. The concentration of the slurry determines its rheology characteristic. The rheology characteristic affects the fluid behavior. In the chapter 5, the function of dispersant (Triton X-100) on LSCF slurry are studied. In the chapter 6, the effects of binder and solid loading were evaluated. In addition, the sintering time and the sintering temperature affect the width and microstructure. The binder removal process was studied.

4.5.2. Direct writing process parameter analysis. After analyzing of the slurry rheology properties, the direct writing process parameters were evaluated. The microstructure of the electrode pattern lines are not only affected by the concentration ratio of the slurry, but also affected by the extrusion parameters, such as the nozzle size, distance between the nozzle and substrate, pressure in the slurry chamber, and the diffusion rate of the electrolyte substrate. In chapter 7, three major parameters (extrusion pressure, nozzle speed, stand-off distance) were studied based on a full factor experimental design.

CHAPTER 5

Understanding the Effect of Dispersant on LSCF Slurry Rheology

5.1. Requirements of the Slurry for Direct Writing

Nano or submicron sized powders have good potential for SOFC applications, since they possess high surface area, low sintering temperature with the possibility of microstructure control when the attractive forces are of high magnitudes [70]. The choice of nano or submicron powder in this research is also supported by literature wherein micro size fuel cell fabrication was demonstrated using similar powder sizes [71]. The particle size of the powder should be at least about one order of magnitude smaller than the minimum internal dimension of the micro component in order to obtain fairly isotropic behavior [72].

Besides the requirement of powder size, the electrode slurries utilized for direct writing process have to fulfill several requirements which include:

1) The particles should not settle rapidly under the effect of gravity and remain under suspension. The segregation can result in density inhomogeneities during the direct writing of artifacts.
2) In addition, the slurries have to be easily reproduced and be insensitive to slight variations in solid content, chemical composition and storage time [73].

3) The slurries have to have high solid loading content, to achieve reasonable shrinkage rage and achieve a relatively dense microstructure.

5.1.1. Need for dispersant. The combination of high solid loading and small particles leads to higher slurry viscosity because of increased particle-particle interactions and consequent difficulties in slurry handling during the direct writing process. Generally, the concentration, particle size, and viscosity (as controlled by the addition of binder) can all have a pronounced influence on the stability and sedimentation of the slurry. Ceramic powders have the tendency to agglomerate due to the attractive intra-particle Van der Waals forces. However, this tendency can be eliminated with the addition of appropriate dispersants which alter the powder surface properties so that repulsive forces either due to electrostatics repulsion resulting from the overlapping of electrical double layers or due to steric hindrance result from absorption of large molecules become higher than the attractive ones and the particles can remain separated in suspension [70]. In many ceramic shaping processes including slip casting, tape casting or spray drying, a dispersant is generally added to the ceramic slurry to facilitate ball milling and produce ceramics with superior properties.

5.1.2. Function of the dispersant. Dispersant addition can dramatically reduce the viscosity of slurries with very high solid content. The utilization of effective dispersant is prominent within the ceramic industry. A dispersant is used for the stabilization of oxide powder slurries. The type of dispersant to be used with a particular ceramic powder as well as its optimum quantity is vital in order to prepare stable slurries of high solids content that can produce defect-free, high quality products.

Dispersants are chemicals, which have components of surface-active agents called surfactants. The dispersants aids in the breaking up of the agglomerate into smaller particle. Suspension processing is an integral component of many ceramic forming processes, such as spray drying, slip casting, tape casting, and gel casting. Various polymeric additives are used in this processing of ceramic powders to produce the flow behavior and suspension properties that are required for shape forming. The goal is to obtain a well-dispersed and stable suspension, with a low viscosity to facilitate casting and a small yield stress to prevent settling [74].

Generally, without a dispersant, the wetting and immersion process of a high-energy ceramic powder surface with a lower-energy liquid occur almost simultaneously. These processes are both irreversible and rapid. However, the dispersion and stability steps are more complex and may occur on different time scales, depending on the particle concentration in suspension.

5.2. Experiments

5.2.1. Cathode slurry materials. The cathode material consisted of LSCF powder (manufacturer: Fuel cell material company). The surface area of powder was $6.3 m^2/g$. To prepare cathode slurry, LSCF powders were mixed with organic solvent α terpineol, dispersant (Triton X-100) and binder (PVB). Solid loading was varied from 40wt%, 50wt% to 60wt%.

Triton X-100 was chosen as a dispersant and it has successfully been used for YSZ submicron powder stabilization as reported elsewhere [75]. Triton X-100

($C_{14}H_{22}O(C_2H_4O)_{10}$) is a nonionic surfactant which has a hydrophilic polyethylene oxide group (on average it has 9.5 ethylene oxide units) and a hydrocarbon lipophilic or hydrophobic group. It has been used in dispersion of carbon materials for soft composite materials.

5.2.2. Binder concentration. The electrodes of the fuel cell must maintain a stable porous structure during the sintering process. PVB (Polyvinyl butyral) was chosen as binder. The use of binder (PVB) increases the viscosity and stability of the slurry due to PVB's large sized molecules as explained in chapter 6. This higher viscosity can assist in controlling the direct writing process to obtain desirable results. It can be burnt out under 400°C [76]. The detail binder removal process will be discussed in chapter 6.

Based on prior research [proposal] it has been proved that 10-15 weight % of binder is suitable for direct writing the porous cathode without through-hole microstructure. In this dispersant research, in order to understand the dispersant's effect on the slurry's rheological properties, the concentration of binder was kept constant at 12 wt% of the solid powder loading.

5.2.3. Variations in dispersant and solid loading concentrations. Based on prior research, the slurry with 50% solid loading and 1% dispersant and 15% binder has shown reasonable fabrication quality for the direct writing process. In this research, three sets of solid loading slurries were researched. These include 40wt%, 50wt% and 60wt%. The concentrations of dispersant were varied from 0, 0.2, 0.4, 0.6, 1 and 1.5wt% of the solid loading.

The knowledge of the slurry's rheological characteristics is valuable in predicting the pumpability and pourability performance in a dipping or coating operation. Viscosity is a principle parameter to evaluate flow measurements of fluids, such as gases, liquids and semi-solids [77]. In this research the viscosity measurements are made in conjunction with flow characterization, direct writing process's efficiency and the sintered line's quality. In order to realize effects of dispersant on different solid loading slurries, rheological characteristics of different constituent concentration combinations were studied as shown in Table 5.1.

Table 5.1. Slurry concentration combinations

Solid loading (wt%/ v)	Dispersant (% of solid loading wt)	Binder (% of solid loading wt)
40%	0.0	12%
40%	0.2	12%
40%	0.4	12%
40%	0.6	12%
40%	1.0	12%
40%	1.5	12%
50%	0.0	12%
50%	0.2	12%
50%	0.4	12%
50%	0.6	12%
50%	1.0	12%
50%	1.5	12%
60%	0.0	12%
60%	0.2	12%
60%	0.4	12%
60%	0.6	12%
60%	1.0	12%
60%	1.5	12%

The rheological properties of the slurries were measured with a rotational viscometer (Brookfield LVDV-III Ultra Rheometers) using a concentric cylinder measuring geometry (SC4-15,) at 22.4°C. The viscosity of the slurries was measured for shear rate between 0.05 and $7s^{-1}$ for a minimal of (n=3) times to ensure good reproducibility. Figure 5.1 shows Brookfield LVDV-III Ultra Rheometer.

Figure 5.1. Brookfield Rheometer [77]

5.2.4. Slurry preparation process. To prepare the slurry, two separate milling processes were performed. Initially for wetting the powder, nano size LSCF powder was

mixed with solvent (50% volume) α -Terpineol and dispersant Triton. The mixture was ball milled in Spex Mixer/Mill (Spex800 M) for 20 minutes. In addition, 12 wt% binder was melted and ball milled with the remaining solvent (50% solvent) at 100°C. Finally, both LSCF powder and binder mixture were ball milled together for 90mins.

5.2.5. YSZ substrate preparation. In this research, the substrate was made of 66% YSZ (particle size 55nm) and 34% YSZ (particle size 5-10 nm). The YSZ powder was put into a die with a diameter of 25mm. The electrolyte substrate was pressed at 10000lb for 5 minutes and sintered at 1350°C for 10 hours. After sintering, the samples were polished as the surface roughness of the substrate directly affects the expansion of cathode trace. The substrate surface was polished sequentially by the following sand papers (180, 400, 600, and 800) for at least 15 minutes under a 12 lb load.

5.2.6. Testing procedures. The viscosity of cathode slurry is the measure of the internal friction of the fluid. Newtonian fluid and non-Newtonian fluid have different relationships between shear stress and shear rate. For a Newtonian fluid, a plot of shear stress versus shear rate at a given temperature is a straight line with a constant slope that is independent of the shear rate. However, for a non-Newtonian fluid, the slope of shear stress and shear rate is not a constant. When the viscosity decreases with an increase in the shear rate, the fluid is called shear thinning. In the opposite case where the viscosity increases as the fluid is subjected to a higher shear rate, the fluid is called shear-thickening [78]. In this research, rheological properties of different slurries and their effect on the direct writing were studied. Important aspects of the slurry's rheological behavior are explained below.

5.2.6.1 Stability of slurry viscosity with respect to time. The rotational viscometer uses the concept that a torque (shear stress) is required to rotate an object in a fluid. The viscometer measures the torque required to rotate a spindle in a fluid at a known speed. During the operation, the viscometer generates a torque in the slurry. In order to attain a stable viscosity at a specific torque, different composition slurries take different time period to stabilize.

Thus before measuring the rheology of the slurry, it is important to understand the time periods required to attain constant viscosity reading. To evaluate the stable time periods for a constant shear rate at 22.4°C, data was collected every 30 seconds until stable viscosity was achieved.

5.2.6.2. Effect of shear rate and shear stress variation on slurry viscosity. After investigating stable time periods for different slurries, viscosity measurements were made at different spindle speeds to study the rheological properties of candidate cathode slurries. The procedure involved reducing the shear rate from the highest feasible value to record the viscosity of the slurry until the slurry was stable Rheocalc software was used to plot the share rate, viscosity and provide analysis plots using different fluid models including the Herschel bulkley, power law, etc.

5.6.2.3. Direct writing cathode lines on the YSZ substrate. The cathode slurries were extruded out of a 100µm nozzle. Cathode lines were written on the YSZ substrate under the following conditions (Extrusion pressure 200kPa, 100kPa, 30kPa, nozzle to substrate distance: 100µm and speed of nozzle: 0.5 mm/s). For each type of slurry, four 10mm length lines were written. Direct-writing pressures were chosen based on the

minimal threshold required to extrude a given slurry composition (e.g. 200kPa for 60% solid loading 100kPa for 50% solid loading, and 30 and 15 kPa for 40% solid loading, respectively) In order to compare the direct writing results for 50% and 60% solid loading, 50% solid loading slurries were extruded under 200kPa. Similarly, to compare 40% and 50% solid loading, the 40% solid loading slurries were extruded under 100kPa also. The 40% solid loading slurries were not extruded under 200kPa as the line width after extrusion at this pressure was excessively large for practical cathode electrode fabrication.

5.6.2.4. Evaluating width and height of the line. Cathode lines were observed by a Zeiss microscope. Top view and profile images of cathode lines were recorded. Image-pro plus software was used to check the width and height of the lines before and after sintering. The average of the peaks heights of the line profile was recorded as the line height.

5.3. Results and Discussion

5.3.1. Stability of slurries with respect to time. The slurry with 60% solid loading was highly viscous and attained a stable reading after 300s. The slurries with 50% and 40% solid loading had lower viscosities as compared to 60% solid loading. These slurries attained stability after 200s. Figures 5.2, Figure 5.3 and Figure 5.4 show time period to attain stable viscosity reading for 60%, 50%, and 40% solid loading, respectively. All the readings were recorded at 22.4°C. And all slurries show time independent feature with the experiment time period.

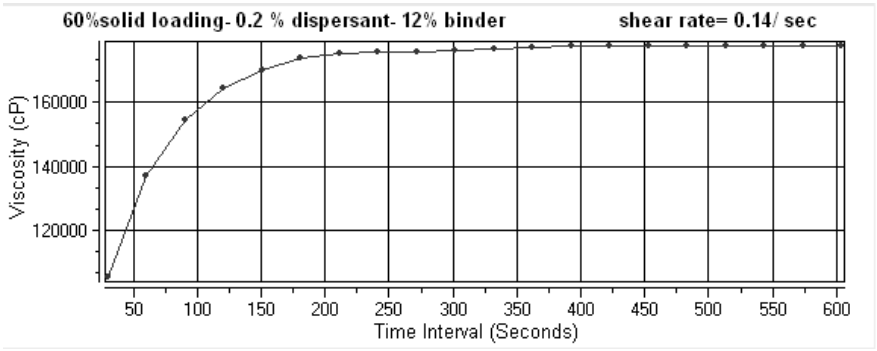

Figure 5.2. 60% solid loading 0.2 % dispersant, 12 % binder, slurry at shear rate of 0.14/s

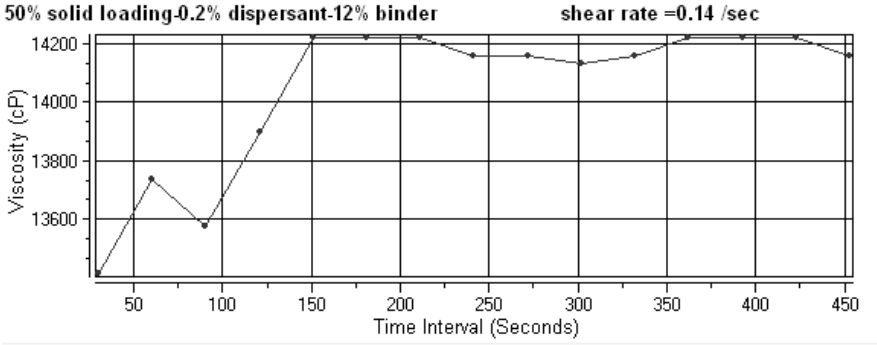

Figure 5.3. 50% solid loading 1.5 % dispersant, 12% binder, slurry at shear rate of 0.14/s

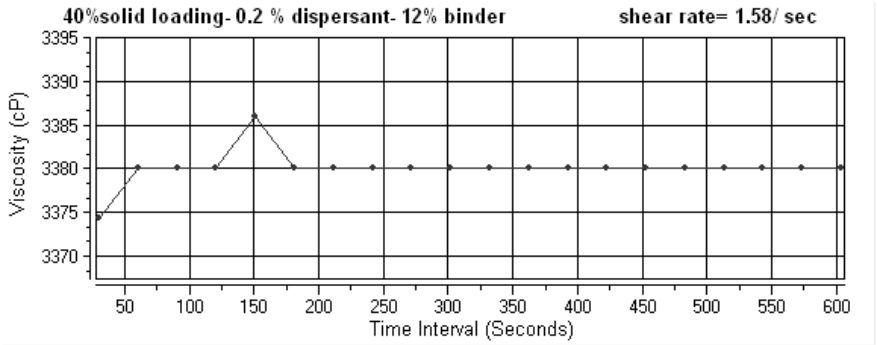

Figure 5.4. 40% solid loading, 0.2% dispersant, 12 % binder, slurry at shear rate of 3.8/s

5.3.2. Rheological characteristic of slurries. The rheological behavior of slurries was evaluated by monitoring the apparent viscosity obtained from the shear rate versus shear stress curves at 22.4°C. Based on differences shear rate for different slurries, the shear rate was varied from $0.01s^{-1}$ to $7s^{-1}$. Figure 5.5 shows the fluid with different fluid rheological properties.

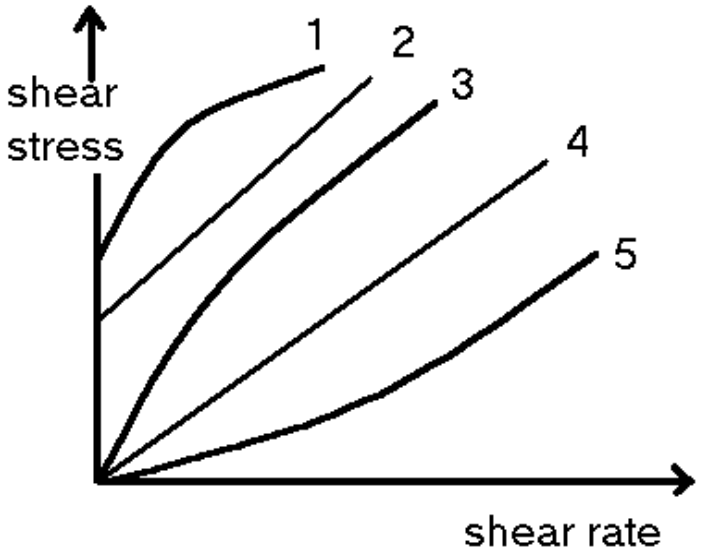

Figure 5.5. Fluid with different fluid rheological properties Where 1-viscoplastic fluid, 2-bingham fluid, 3-pseudoplastic fluid, 4-Newtonian fluid, 5-dilatant fluid [79].

Herschel-Bulkley generalized non-Newtonian fluid model was used to analysis the rheological data. The three parameter rheological model is mathematically described as following. Equation (5.1) shows the Herschel-bulkley model, where τ means shear

stress; D means shear rate; k means consistency index; n means flow index; and τ^o means yield stress.

$$\tau = \tau^o + kD^n \tag{5.1}$$

- When τ^o equals to 0, and n equals or approximate to1, it indicates that the slurry is Newtonian fluid
- When τ^o equals to 0, and n is smaller than 1, it indicates that the slurry is a pseudoplastic fluids
- When τ^o equals to 0, and n is larger than 1, it indicates that the slurry is a dilatants fluid.(shear thickening)
- When τ^o is not equal to 0, and n equals or approximate to1, the slurry is a Bingham fluid.
- When τ^o is not equal to 0, and n is smaller than 1, the slurry is a viscoplastic fluid.

A Bingham or Viscoplastic fluid behaves like solid under static conditions. A certain amount of force must be applied to the fluid before any flow is induced. This force is called yield stress. Once the yield value is exceeded and flow begins. Plastic fluids may display Newtonian, Pseudoplastic or Dilatant flow characteristics. Figures 5.6 to 5.11 show the viscosity and share rate plot and shear rate and shear stress plot (Hershel-Bulkley analysis plot) for slurries with different concentrations. They display different flow characteristics of slurry.

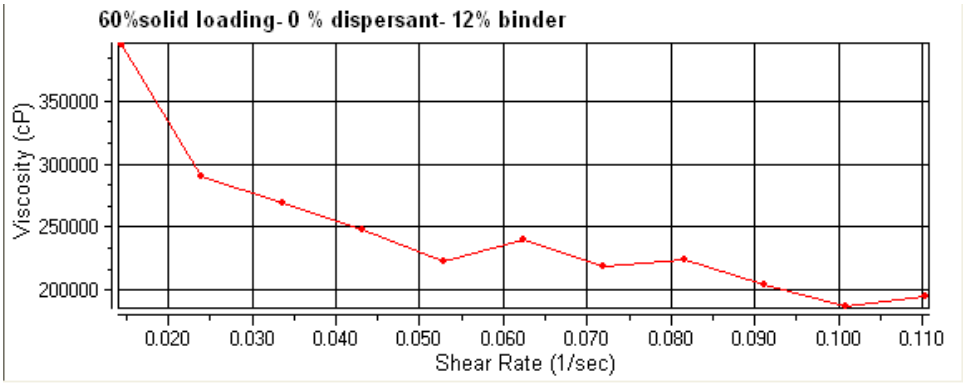

(a)

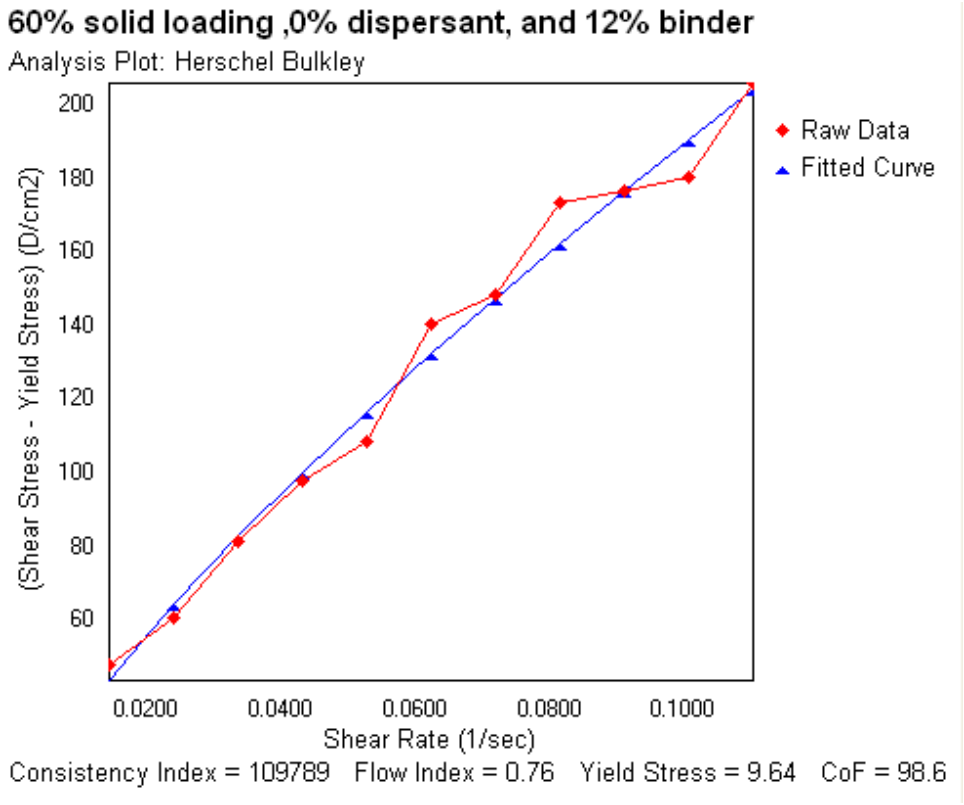

(b)

Figure 5.6 (a) Viscosity and share rate plot and (b) Shear rate and shear stress plot (Hershel-Bulkley analysis plot) for slurry with 60% solid loading, 0% dispersant and 12% binder. This slurry is a Viscoplastic fluid.

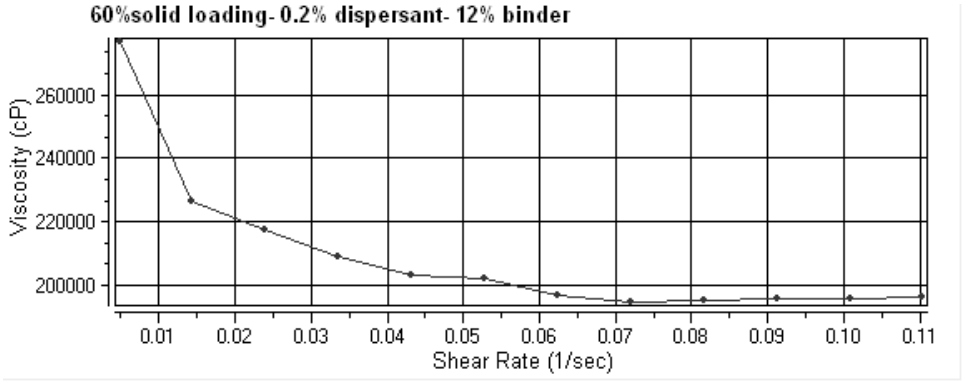

(a)

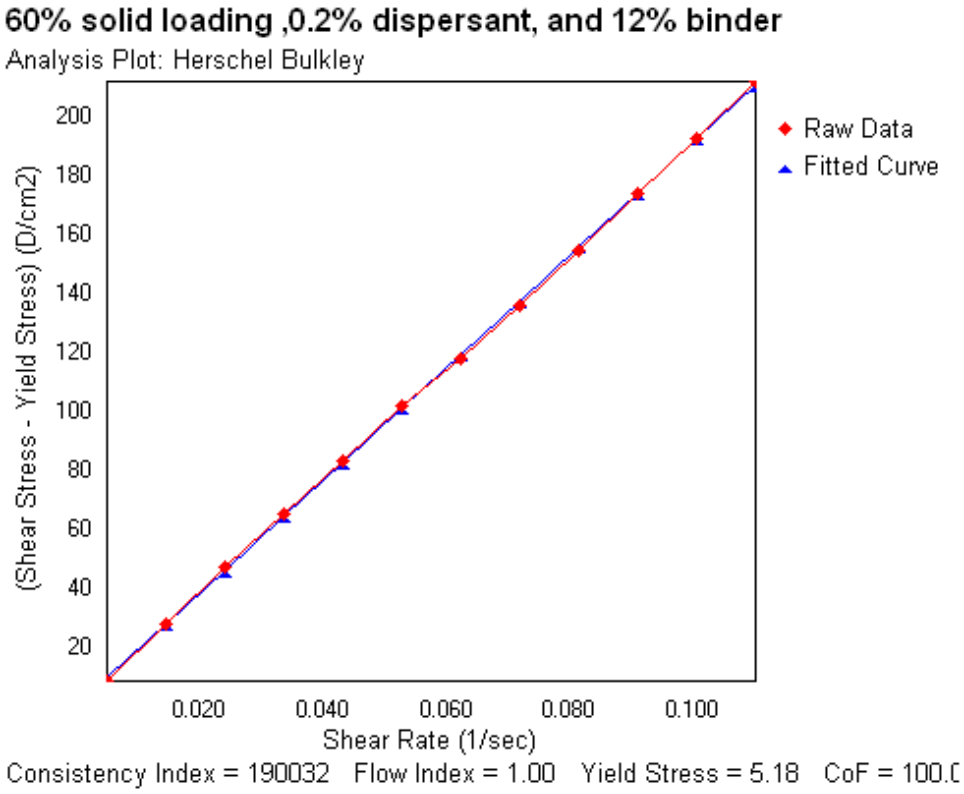

(b)

Figure 5.7 (a) Viscosity and share rate plot and (b) Shear rate and shear stress plot (Hershel-Bulkley analysis plot) for slurry with 60% solid loading, 0.2% dispersant and 12% binder. This slurry is a Bingham fluid.

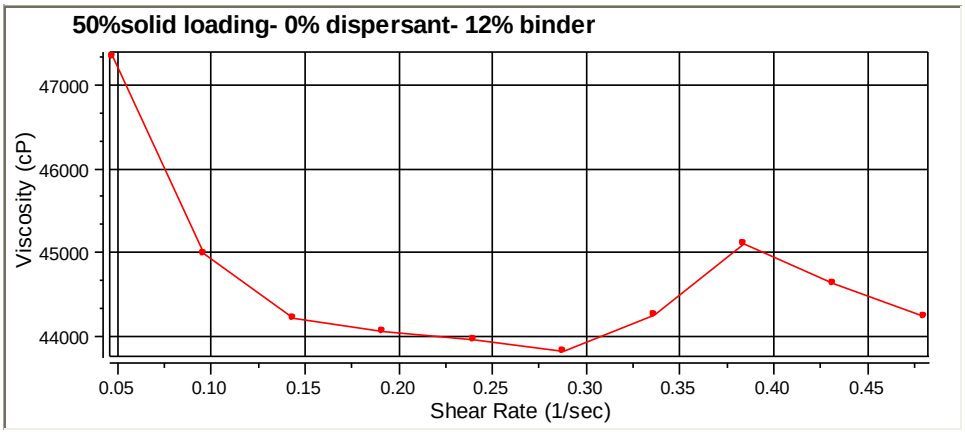

(a)

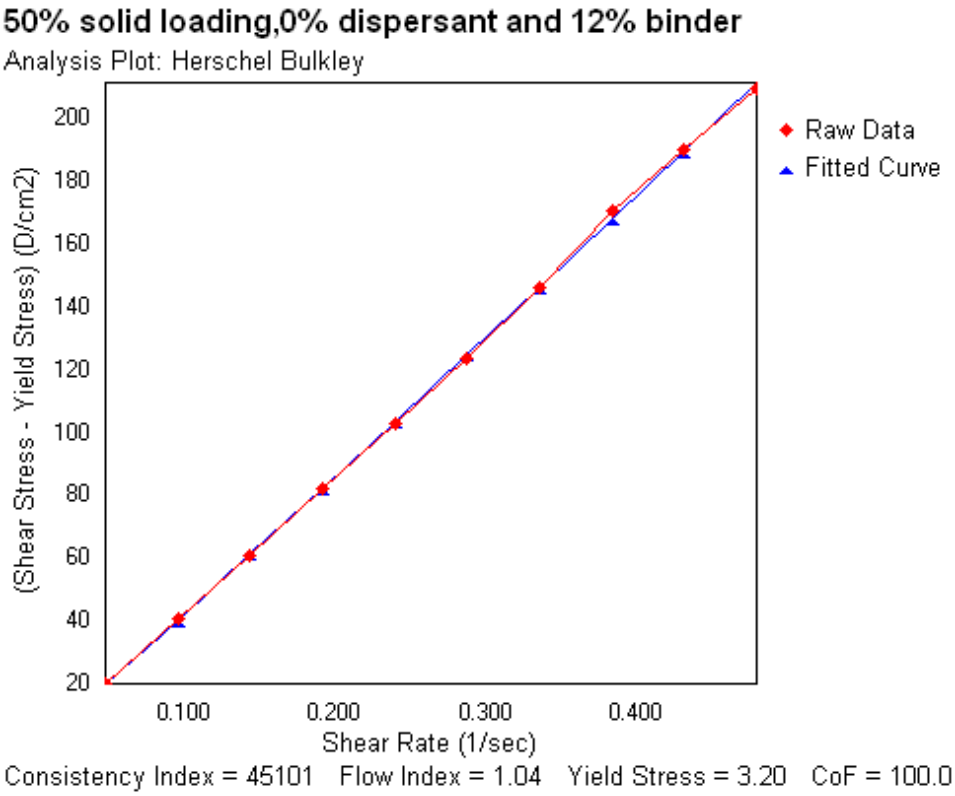

(b)

Figure 5.8 (a) Viscosity and share rate plot and (b) Shear rate and shear stress plot (Hershel-Bulkley analysis plot) for slurry with 50% solid loading, 0% dispersant and 12% binder. This slurry is a Bingham fluid.

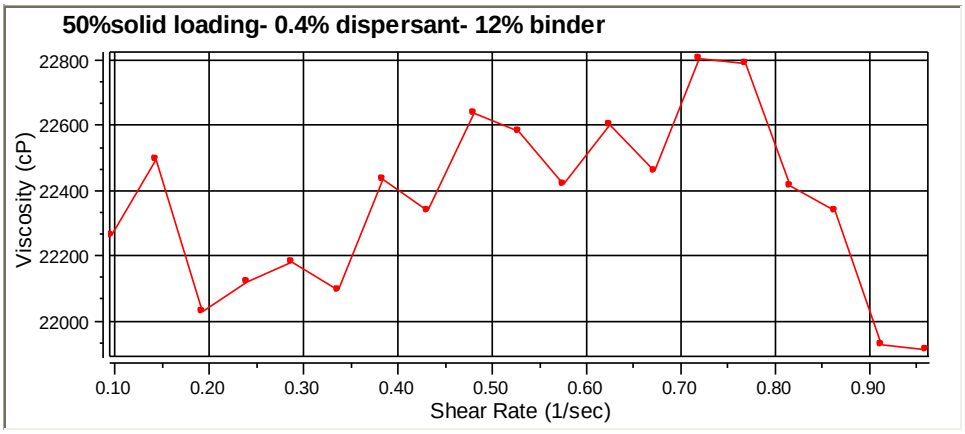

(a)

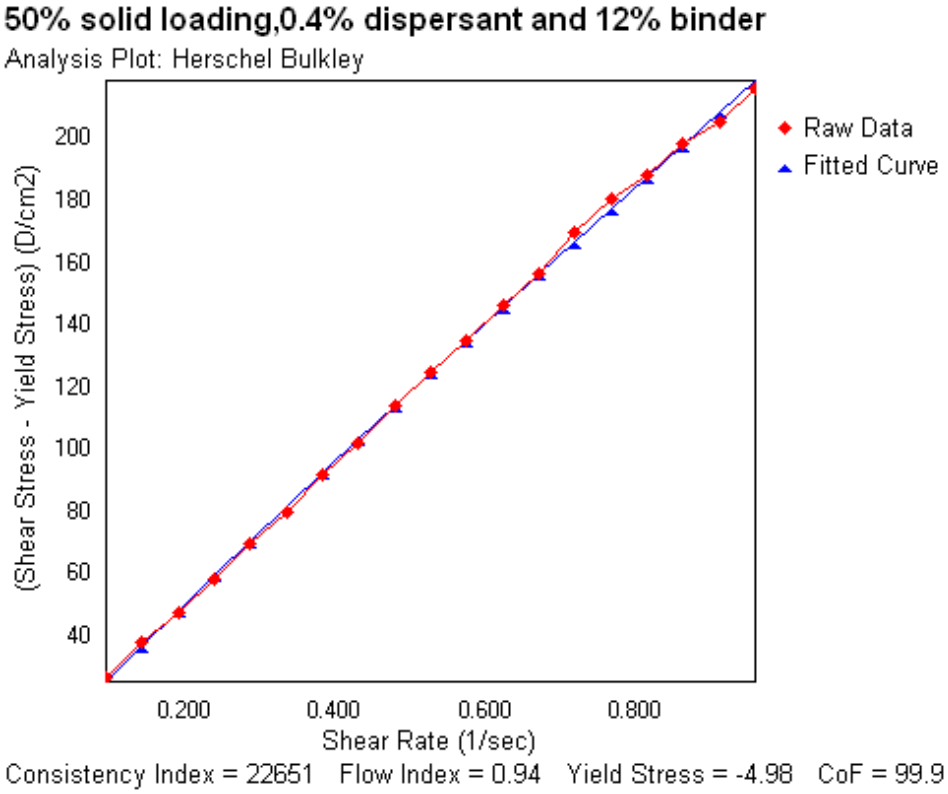

(b)

Figure 5.9 (a) Viscosity and share rate plot and (b) Shear rate and shear stress plot (Hershel-Bulkley analysis plot) for slurry with 50% solid loading, 0.4% dispersant and 12% binder. This slurry is a pseudoplastic fluid.

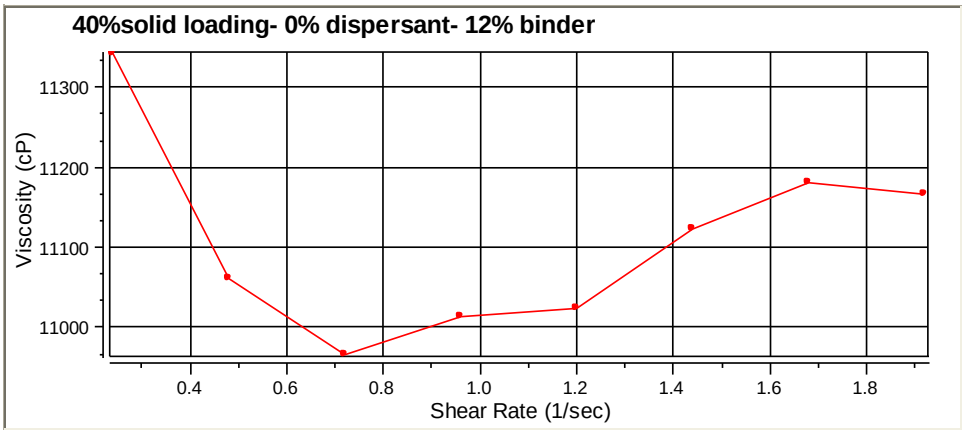

(a)

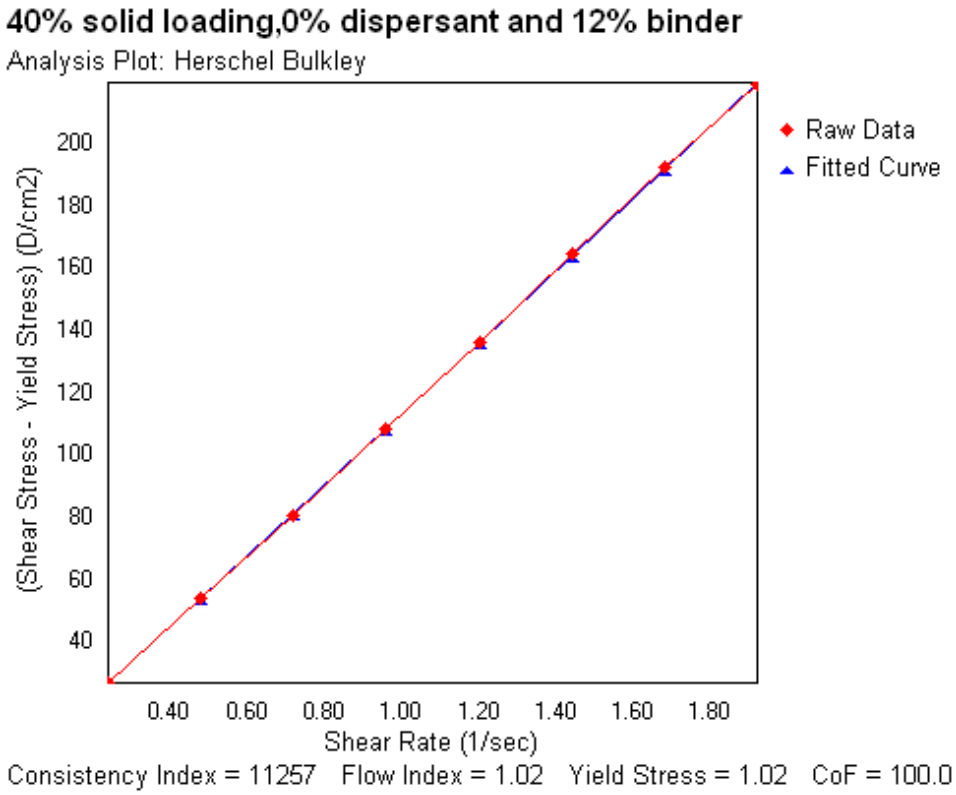

(b)

Figure 5.10 (a) Viscosity and share rate plot and (b) Shear rate and shear stress plot (Hershel-Bulkley analysis plot) for slurry with 40% solid loading, 0% dispersant and 12% binder. This slurry is a Newtonian fluid.

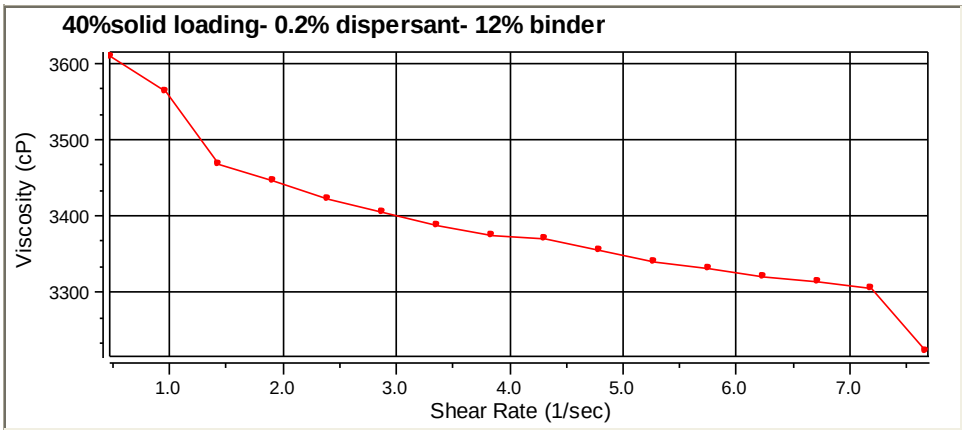

(a)

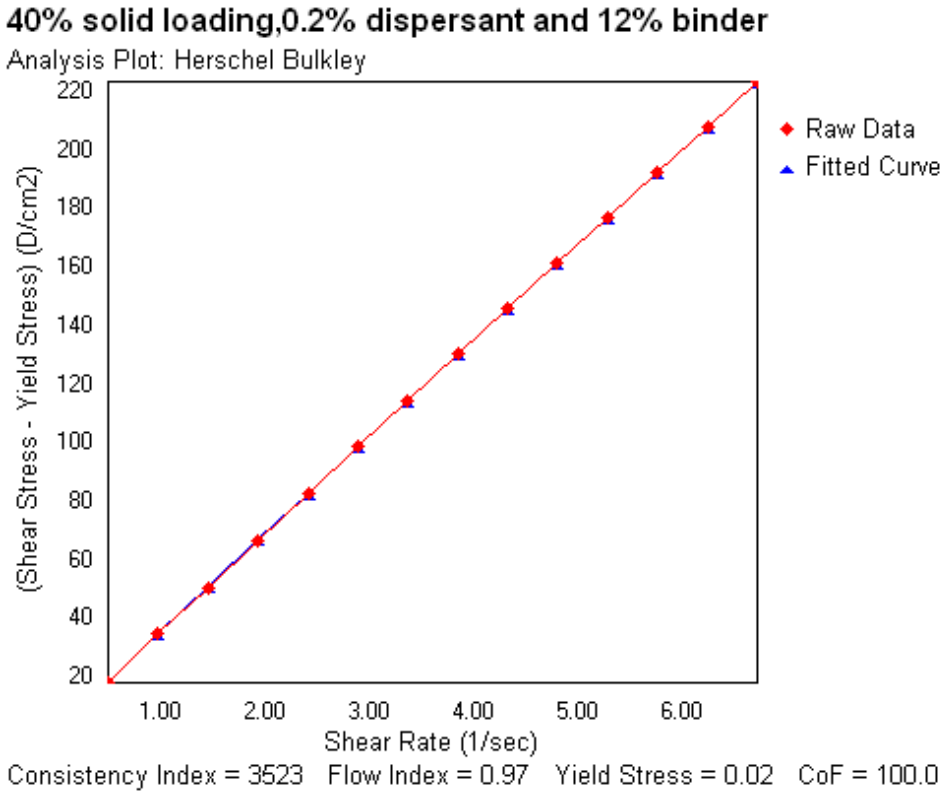

(b)

Figure 5.11 (a) Viscosity and share rate plot and (b) Shear rate and shear stress plot (Hershel-Bulkley analysis plot) for slurry with 40% solid loading, 0.2% dispersant and 12% binder. This slurry is a Newtonian fluid.

5.3.3. Evaluating the optimal dispersant concentration. The effectiveness of dispersants on slurry flow behavior was determined by rheology measurements. The viscosity of slurries without the addition of any dispersant was determined for comparison with the stabilized dispersions. The apparent viscosities were measured when toque equaled to 70% and shear stress was around 158 D/cm^2. The viscosity of the candidate slurries are plotted against the amount of dispersant in wt% of the LSCF powder used.

For 60% solid loading slurries, the Triton dispersant has a very high dispersing power, reducing the viscosity relative to dispersant–free dispersion by around 70% (Figure 5.12). At 0.4wt%, the 60% solid loading slurry achieved minimal viscosity. 0.4 wt% was the optimal dispersant concentration for 60% solid loading. The effectiveness of this dispersant can be explained based on strong adsorption and modification of the surface properties of the slurry powder which results in a strong reduction of the hamaker constant.

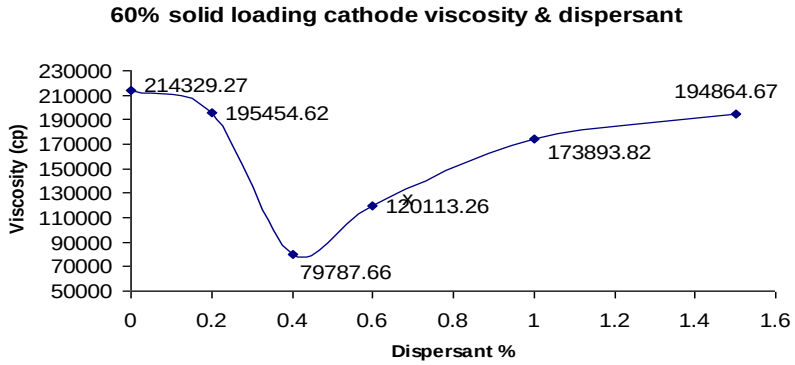

Figure 5.12. 60% solid loading cathode viscosity vs. dispersant concentration

For 50% and 40% solid loading, the slurries exhibited a minimum viscosity for dispersant concentration between 0.2-0.4 wt% (Figure 5.13 and 5.14). However, addition of dispersant beyond this threshold leads to an increase in the viscosity due to interactions between the free-floating dispersant molecules. This increase is likely due to dispersant-solvent interactions due to the free dispersant molecules in solution [75].

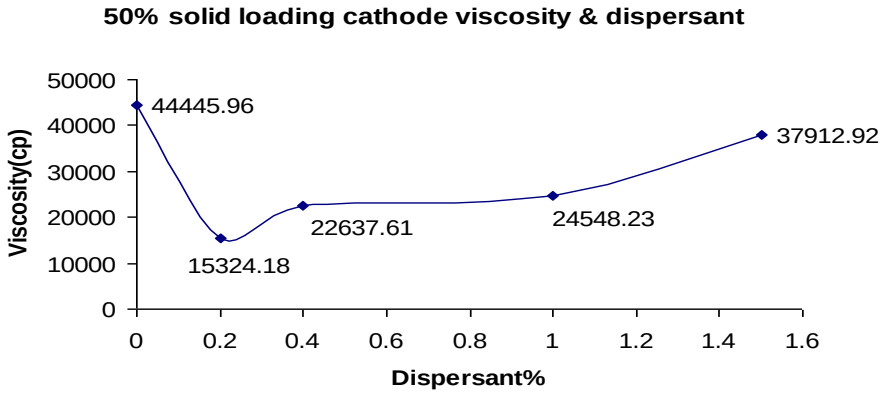

Figure 5.13. 50% solid loading cathode viscosity vs. dispersant concentration

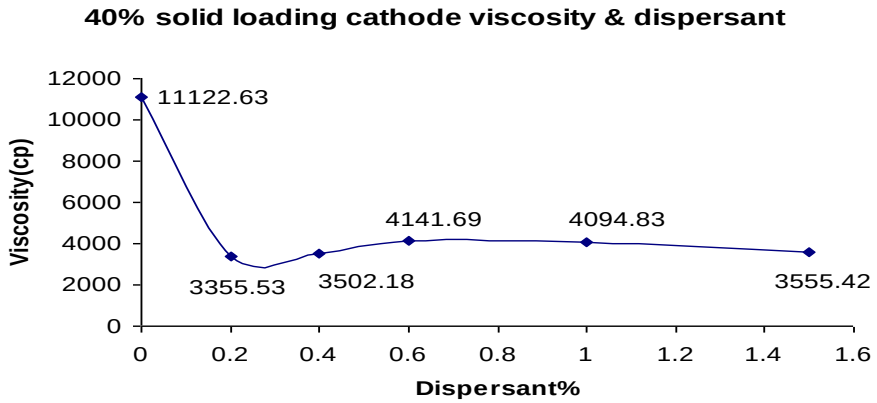

Figure 5.14. 40% solid loading cathode viscosity vs. dispersant concentration

5.3.4. Evaluating width and height of lines. The slurries were used to write three lines on the YSZ substrate, Table 5.2 shows the dimensional results for the cathode lines. For 60% solid loading slurry, the lowest extrusion pressure was 200kPa. 40% and 50% solid loading slurries could be extruded under 100kPa, for 40% solid loading slurries the lowest extrusion pressure was as low as 15kPa. However, during the writing process, the manipulation of low pressure was difficult to control. This table lists the dimension under 100kPa for 40% solid loading slurries, 200kPa for 50% solid loading slurries and 200kPa for 60% solid loading slurries.

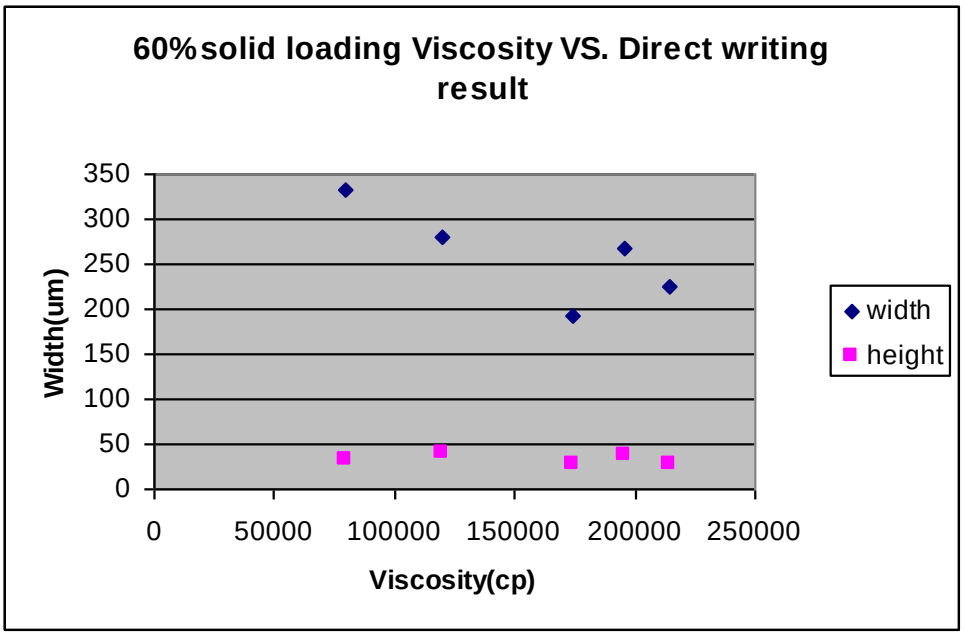

Figure 5.15. 60% solid loading viscosity vs. dimension result

Table 5.2. Slurry's viscosity and line dimension

Slurry Composition	Viscosity (cp)	Pressure (kPa)	Width(μm) before sinter	Height(μm) before sinter	Standard deviations of width	Standard deviations of height
60-1.5-12*	194864.67	200	208.01	19.48	6.75	2.35
60-1-12	173893.82	200	191.51	28.00	12.79	6.63
60-0.6-12	120113.26	200	280.67	40.00	17.51	6.73
60-0.4-12	79787.68	200	332.29	31.54	12.93	10.19
60-0.2-12	195454.62	200	302.34	36.24	4.36	3.73
60-0-12	214329.27	200	225.30	26.67	19.42	6.20
50-1.5-12	37912.92	200	465.79	44.72	22.12	6.34
50-1-12	24548.23	200	669.70	34.71	19.26	3.75
50-0.4-12	22637.61	200	489.48	27.32	3.88	4.70
50-0.2-12	15324.18	200	671.55	101.61	13.44	9.14
50-0-12	44445.96	200	362.79	23.33	14.66	2.37
40-1.5-12	3555.42	100	1185.34	92.50	76.02	0.07
40-1-12	4094.83	100	1073.64	42.25	74.13	2.11
40-0.6-12	4141.69	100	862.04	41.88	39.31	1.46
40-0.4-12	3502.18	100	1246.96	53.67	45.60	2.83
40-0.2-12	3355.53	100	899.69	40.80	68.21	2.55
40-0-12	11122.63	100	555.11	62.08	19.74	17.63

Note: * 60-1.5-12 denotes that the slurry has 60% solid loading, 1.5% dispersant, and 12% binder. The concentration of dispersant and binder are weight percentages of the solid loading

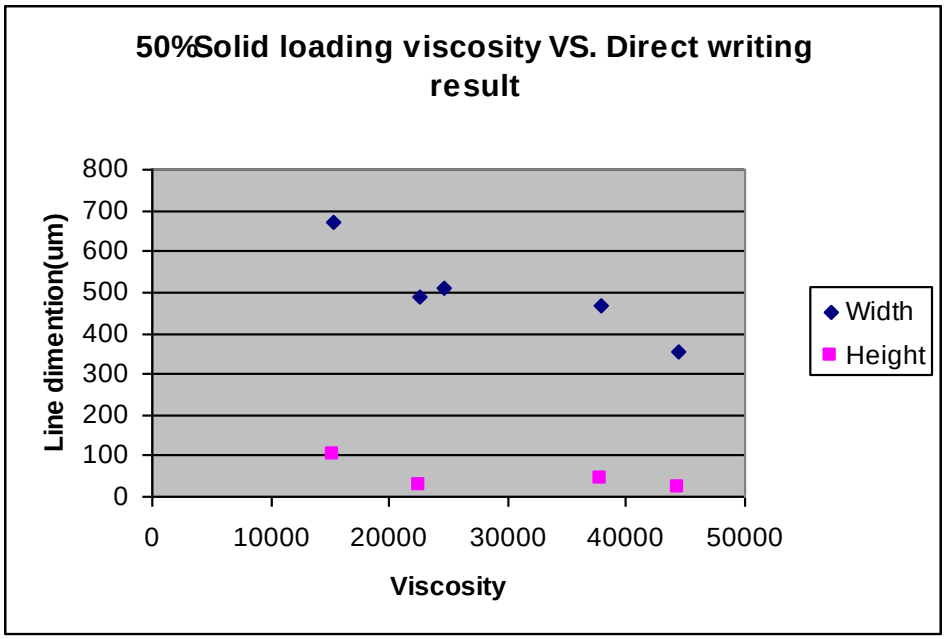

Figure 5.16. 50% solid loading viscosity vs. dimension result

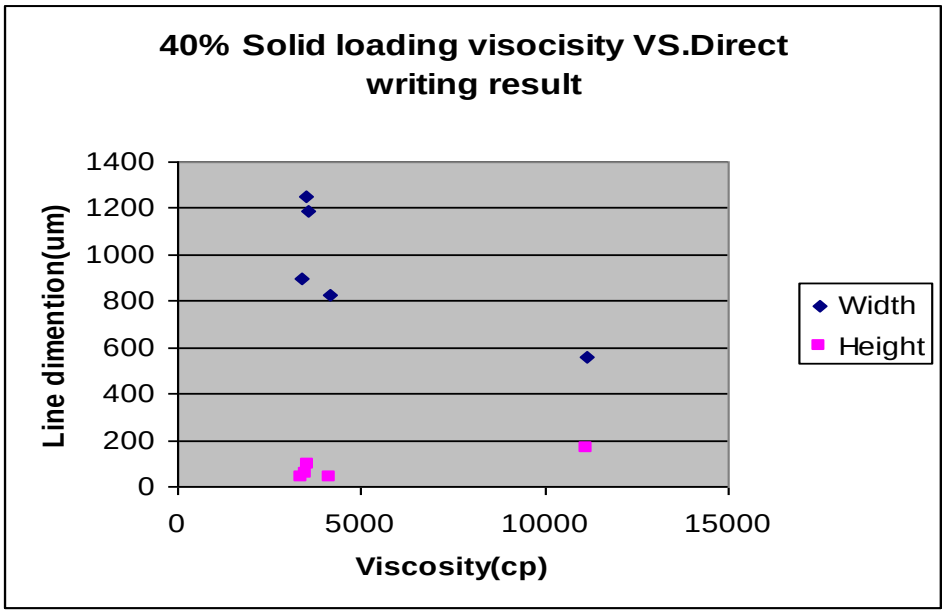

Figure 5.17. 40% solid loading viscosity vs. dimension result

Based on the Table 5.2, the line dimension and viscosity were plotted in 5.15-17. For 60% solid loading slurries, under 200kPa, the range of line width were 190-330μm. For 50% solid loading slurries, under 200kPa, the range of line width were 360-670 μm. For 40% solid loading slurries, under 100kPa, the range of line width were 550-1250 μm. The line width increased as the solid loading significantly. Table 5.3 shows the summary of viscosity and dimension without slurry composition. This summary can be used to choose the direct writing pressure in general, based on the viscosity of slurry.

Table 5.3. Summary of viscosity and line dimension

Pressure (kPa)	Viscosity (kcp)	Line width before sintering (μm)	Line height before sintering (μm)
200	150-220	180-260	20-36
200	80-150	280-330	30-40
200	20-45	360-500	23-40
200	10-20	>600	Around 100
100	10-15	Around 600	Around 190
100	3.2-5	>800	40-100

5.4. Conclusion

Dispersant plays an important role on rheology characterization for the slurry's stability and brakes up the agglomerate into smaller particles. In this study, the effect of Triton X-100 on LSCF slurries was evaluated for their respective rheological characteristics and dimensions of direct written lines. The optimum concentration of Triton X-100 for different slurries was around 0.2- 0.4% of the LSCF solid loading. The effectiveness of this dispersant can be explained based on strong adsorption and

modification of the surface properties of the slurry powder which results in a strong reduction of the hamaker constant.

60% solid loading slurries had high viscosities and attained stability after 300s. Their behaviors resemble those of Viscoplastic and Bingham fluid, with an initial yield stress. 40-50% solid loading slurries had relative lower viscosity and attainted stability after 200s. Their behaviors resemble those of Pseudoplastic and Newtonian. The rheological characterization of slurries with different dispersant loadings provides important flow behavior information to select appropriate direct writing process parameters.

Even though dispersant affects the direct writing line dimensions, the effects of other two composition factors (solid loading and binder) may be significant. They will be discussed in the chapter 6.

CHAPTER 6

Evaluating the Effect of LSCF Slurry Solid Loading and Binder Concentrations

6.1. Introduction

Ceramic powders are inherently difficult to handle and shape into desired components because of their discreet nature and lack of cohesiveness and plasticity. Organic processing aids, such as polymers (binders), plasticizers, dispersants, and solvents are therefore often required to enhance their forming capabilities [44].

Polymer is used as a thickener in commodity and food items such as shampoo and even ice cream. When a polymer is dissolve in a solvent, their long molecular chains makes the solution more viscous [80]. Polymers with higher molecular weights exhibit dominant intermolecular forces resulting in higher viscosity polymer solutions. Polyvinyl butyral (PVB) is employed in various industrial and commercial applications. PVB is widely used as a binder in ceramic processing. Organic binders significantly increase the viscosity of the slurry and also stabilize the slurry. Binder is a term used to collectively describe the additives that remain in the as-formed ceramic body after drying [44]. Binder system and binder removal process play significant role to generate porous ceramic entities.

The cathode electrode material for SC_SOFC should have requisite properties such as stability, electronic conductivity, compatibility and porosity. LSCF material is the

most appropriate choice. In the direct writing process, slurries of cathode material are prepared by mixing LSCF powder, dispersant and binder in a solvent. The slurry can be printed on the substrate in the required pattern design. In this research, the inter-digitized design was chosen. Thus, the line dimensions, microstructure and resistance of cathode lines were studied.

As explained in chapter 5, the dispersant affects the slurry's rheology and plays an important role for homogenization into a stable slurry. Also, solid loading and binder affect the slurry's rheology significantly. Further, slurry rheology has an impact on the parameters of direct writing process and the electrical conductivity of the cathode trace. Higher solid loadings of LSCF powder can result in higher conductivity of LSCF line. Also, porous structure of the cathode line can result in a lower conductivity of LSCF. However, porous microstructure is needed to enhance gas access and to accelerate fuel cell electrochemical reaction.

This chapter will focus on evaluating solid loading and binder concentrations with respect to cathode dimensions, microstructure and electrical resistance.

6.2. Experiments

6.2.1. Materials. The cathode material consisted of LSCF powder (manufacturer: Fuel cell material company). The surface area of powder was $6.3 m^2/g$. To prepare cathode slurry, LSCF powders were mixed with organic solvent α terpineol, dispersant (Triton X-100) and binder (PVB). Based on the prior experiments, 12% and 15% binder concentration achieve acceptable porous lines without cracks, when a 100μm nozzle was

used. A 60% solid loading slurry had a higher viscosity, as compared to the 50% and 40% solid loading. In this study, slurries were studied at three different solid loading levels (40%, 50%, and 60%) and two different binder levels (12% and 15%). Table 6.1 lists the candidate slurry compositions.

Table 6.1. Candidate slurry compositions

Sample number	Solid loading (%)	Dispersant (%)	Binder (%)
1	60	0.2	12
2	60	0.2	15
3	50	0.2	12
4	50	0.2	15
5	40	0.2	12
6	40	0.2	15

6.2.2. Experimental protocol.

1) Evaluate the binder removal process, in order to setup the sintering procedure.

In the direct writing process or ceramic fabrication process, it is important to control the burn-out of the organic additives, to minimize a residual carbon that may inhibit the sintering. The electrodes of fuel cell must maintain a stable porous structure during the sintering process. A typical SC-SOFC is operated at 700-800°C. Therefore, the thermal decomposition and elimination of the binder are important factors to operate the fuel cell reliably. The decomposion reaction mechanism of PVB occurs in stages, because PVB is a copolymer and the decomposed products are very complex.

From the initial experimentation and reported literature (Lewis et al. [44]), PVB initially degrades by side group elimination following a sequence similar to that shown in

the Figure 6.1. Initial PVB degradation involves the loss of water, butanal, and acetic acid, leaving long organic chains containing appreciable unsaturation and conjugation. Such chains subsequently degrade by scission with concurrent cyclization and cross-linking reactions to yield significant amounts of carbon residue. Thus, PVB undergoes multi-step degradation processes, typically from volatile species over a relatively broad temperature range [44]. From Kim's research [76], pure PVB was completely decomposed around 500°C. In the presence of the various metal components, the decomposition temperature of the electrolyte green sheet is lowered to around 200°C.

To validate PVB decomposition results from prior research, Lewis (1997) and Kim (1997), the binder decomposition and removal process was studied. Q600 Simultaneous TGA/DSC (SDT) was used for thermal and mass analysis during the drying process. Experiments were conducted in three steps: (i) initial sample consisted of only the binder (PVB), in order to understand the PVB removal process, (ii) slurry (60wt% solid loading, 12%binder, and 1.5%dispersant) was tested. (iii)LSCF lines were written by slurry (60wt% solid loading, 12% binder, 1.5% dispersant) and tested to understand the organic additives removal process.

2) Prepare slurries and test the viscosity.
3) Direct write the lines and measure the line width and height.

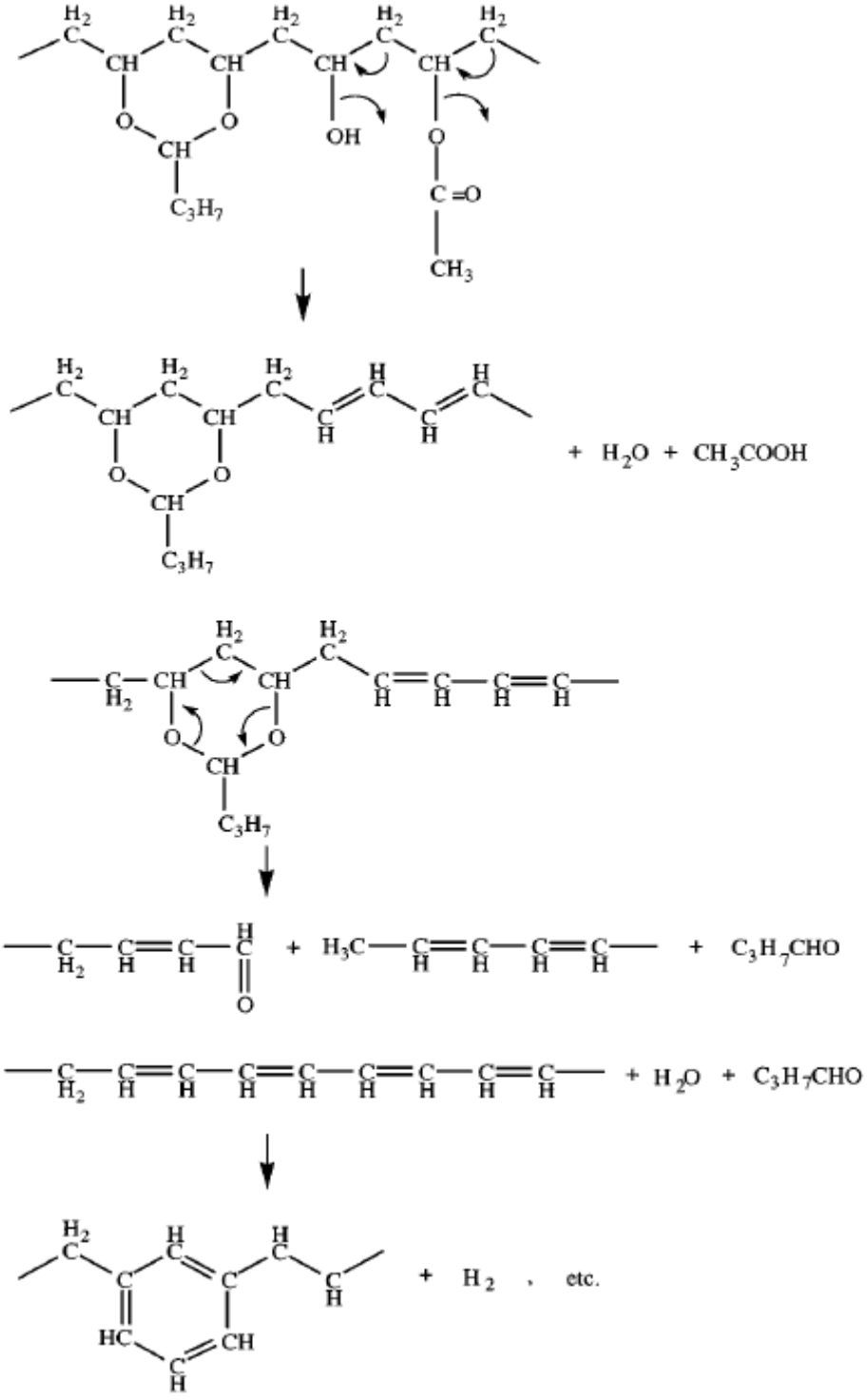

Figure 6.1. Thermal degradation mechanisms of PVB [44]

The cathode slurry was extruded out of the 100μm nozzle. For slurries with different solid loadings, the minimal push-out pressures varied. In the case of 60% solid loading slurry, the minimal extrusion pressure was 200kPa. For a 50% solid loading slurry, the minimal extrusion pressure was around 90kPa. For a 40% solid loading slurry, the minimal extrusion pressure was around 20kPa. Thus different slurries were extruded at respective push-out pressures of 200kPa, 100kPa, and 30kPa. The writing distance between nozzle and substrate was 100μm. The writing speed was 0.5mm/s. Four cathode lines were written on the YSZ substrate under each pressure.

Cathode lines were observed by Zeiss microscope before and after sintering. Four data points per slurry were recorded. Top and profile images of cathode lines were recorded. Image-pro plus software was used to check the width and height of the lines before and after sintering.

4) Testing line's conductivity using a four point probe.

For a micro-solid oxide fuel cell, the resistance of the cathode affects the SOFC's performance. The microstructure of the lines is affected by many factors, including: the composition, the substrate surface properties, and the slurry sintering process. Signatone pro4 and Keithley 2400 series source meter (Figure 6.2) were used to detect the sintered lines' resistance. For each slurry line, two data points were collected. The average of them was recorded as the lines' electrical resistance. The higher resistance means the lower conductivity of the line. By means of testing line's resistance, the conductivity of lines will be estimated and compared.

Figure 6.2. Signatone Pro4 and Keithley 2400 [81]

6.3. Result and Discussion

6.3.1. Binder removal process. Binder removal research was conducted to setup the sintering temperature profile. Figure 6.3 shows TGA & DSC experiment result for drying of PVB material from room temperature to 800°C. The ramp rate is 5°C per minute. Around 87% mass loss occurred at 150-200°C based on an endothermic process. From 200 to 600°C, both endothermic reaction and exothermic reactions occurred during the binder decomposition. During this stage, the balance 10% mass was decomposed leaving no residue. From 600 to 800°C, the mass was stable, and almost all of binder was sintered out. These findings were consistent with results from the Kim's group [76].

Figure 6.4 shows TGA & DSC experiment result for drying of LSCF slurry (60% solid loading, 12% binder and 1.5% dispersant) from room temperature to 800°C. Significant mass loss, around 83% of the total mass loss, occurred between 50-150°C. From 150-350°C, an exothermic reaction occurred with additional mass loss, which was around 20%. After 350°C, the mass was constant with an endothermic reaction.

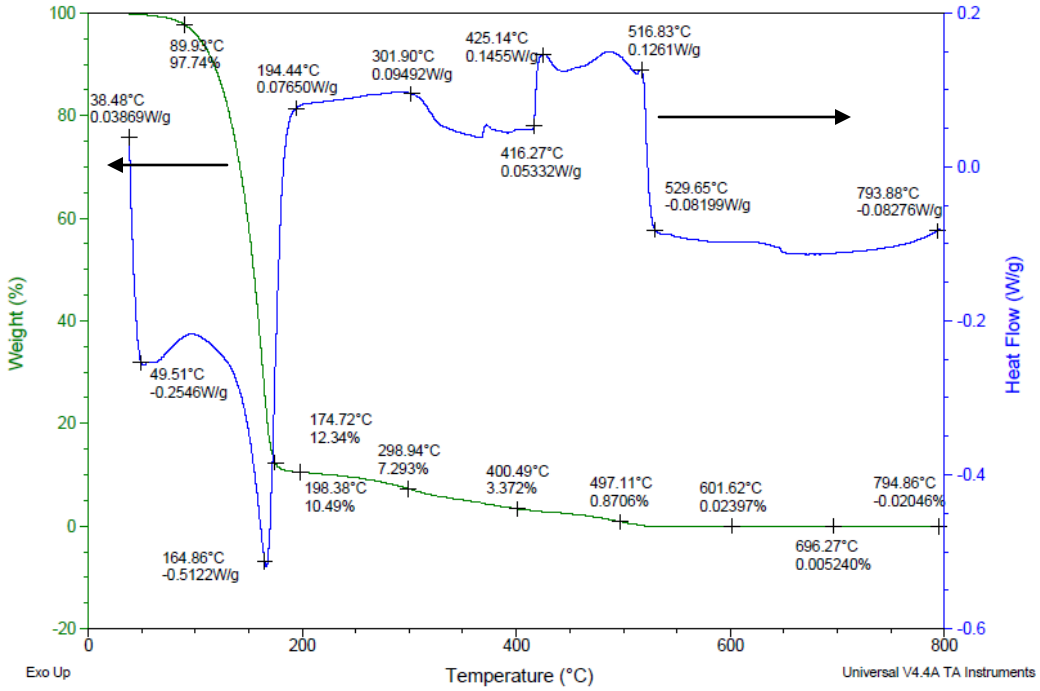

Figure 6.3. Binder decomposition process

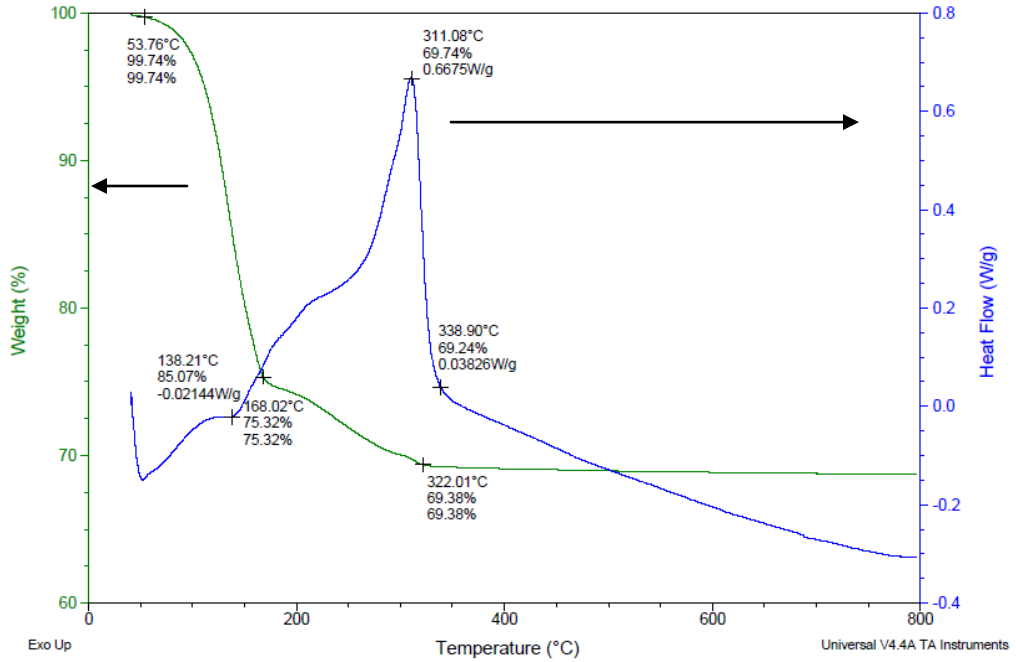

Figure 6.4. Drying process of 60wt% LSCF slurry with 12% PVB, 1.5% Triton

After comparing Figure 6.3 and Figure 6.4, it is evident that differences exist between the binder decomposition processes when combined the LSCF powder. Figure 6.4 shows that at temperature between 150-300°C, the slurry radiated significant heat flux. This may be caused due to the boiling of the solvent (α-terpineol). α-terpineol's boiling point is around 219°C at 100kPa.

However, long cracks were observed on the surface of cathode electrode based on the above mentioned slurry drying temperature profile. This could be attributed to faster drying speeds. To resolve this issue, in the following experiment, the sintering temperature was held constant (dwell at 150°C) for one hour and the ramp rate was reduced to 3°C per minute. The modified mass loss and heat flow profile for adjusted drying process is shown in the Figure 6.5.

At 150°C, an exothermic reaction occurred with additional mass loss. 73% mass loss occurred at 50-150 °C; during dwelling time, there were around 8% mass loss and 17% mass loss occurred at 150-350 °C; at 350-800 °C, the residual mass was stable.

Figure 6.6 shows the drying process of the lines which were written by 60% wt LSCF, 12% PVB, 1.5 % dispersant slurry on the substrate. 46.3% mass loss occurred at 50-150 °C; 7.4% mass loss occurred during dwelling, 20.4% occurred at 150-300 °C. From 300 - 375 °C, the mass was stable, and then 26% mass loss occurred at 375-600 °C; at 600-800 °C, the residual mass was stable. Same as the profile in Figure 6.6, at 150°C, an exothermic reaction occurred with additional mass loss. The other mass loss occurred at 350-400°C. In this case, the drying speed was reduced. There were no long cracks on the surface.

Thus a suitable drying process of LSCF line was attained. Based on the binder decomposition results the sintering profile was determined as following:

- Room temperature to 150°C, rate 3°C/min
- Dwell for 1hour
- Heating to 800°C, rate 3°C/min
- Dwell for 1 hour
- Heating to 1300°C, rate 5°C/min
- Dwell for 3 hour
- Cooling to 50°C, rate 5°C/min.

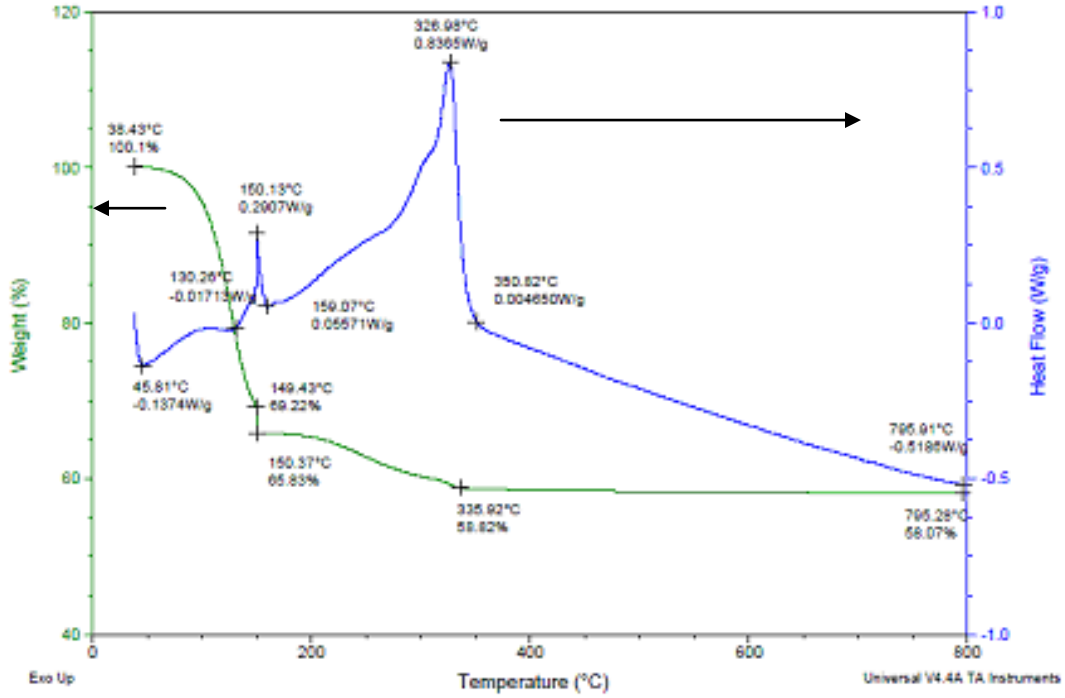

Figure 6.5. Drying process of 60wt% LSCF slurry with 12% PVB, 1.5% Triton; dwelling at 150°C for an hour

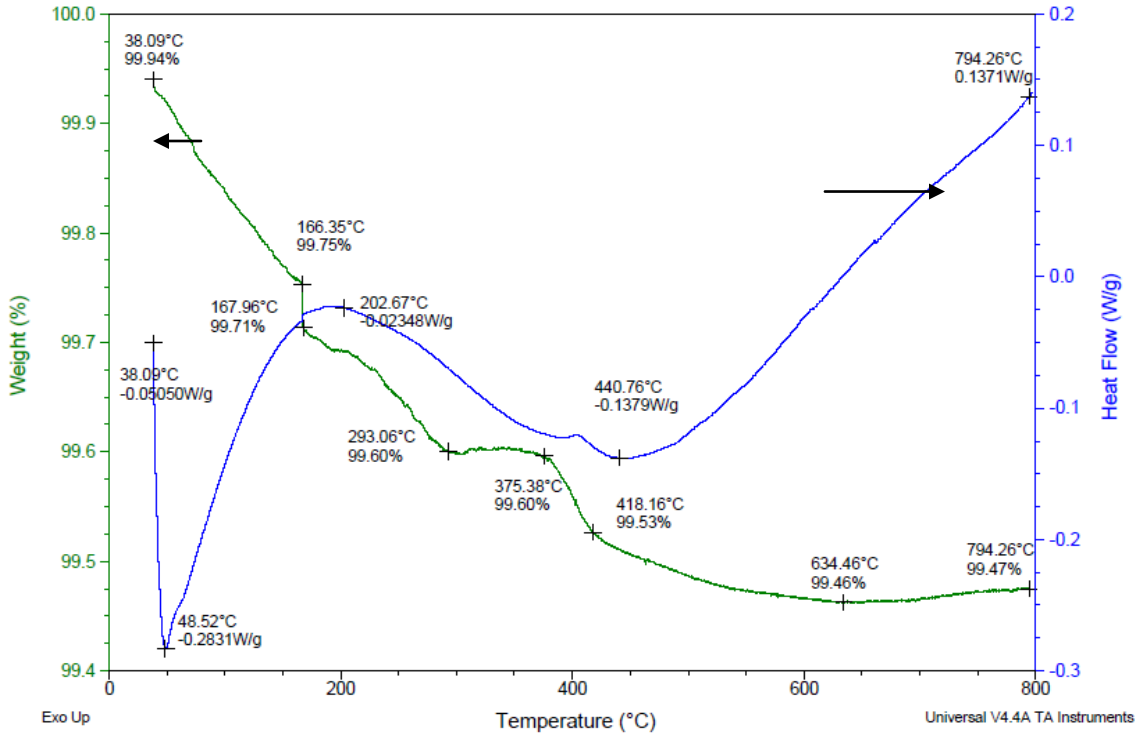

Figure 6.6. Drying process of the lines which written by 60% wt LSCF, 12% PVB, 1.5 % dispersant slurry

6.3.2. Effect on slurry rheology. Rheological characterization of slurries was conducted based on their solid loading and binder concentrations. Table 6.2 shows the analysis parameters based on the Herschel-Bulkley model.

The slurries with 40% solid loading displayed a pseudoplastic fluid behavior as shown in Figure 6.7. The slurries with 50% displayed Newtonian fluid behavior as shown in Figure 6.8. However, slurries with 60% solid loading displayed a viscoplastic fluid behavior as shown in Figure 6.9. In a typical, viscoplastic fluid a yield stress has to be overcomed before the slurry begins to flow.

Table 6.2. Analysis parameters based on Herschel-Bulkley model

Solid loading %	Binder %	Consistency index	Flow index	Yield stress	Coefficiency
40	12	3523	0.97	0.02	100
40	15	9064	0.97	-0.03	100
50	12	22546	1.00	-0.14	100
50	15	55091	1.01	0.67	100
60	12	130794	0.95	-1.90	100
60	15	368680	0.95	2.75	100

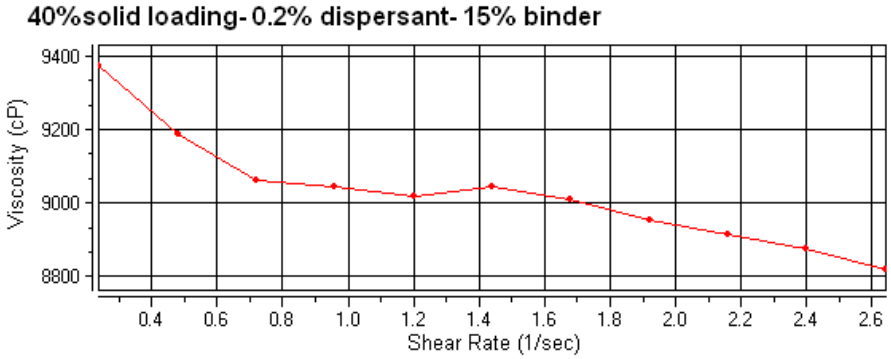

Figure 6.7. Viscosity and share rate plot and for slurry with 40% solid loading, 0.2% dispersant and 15% binder.

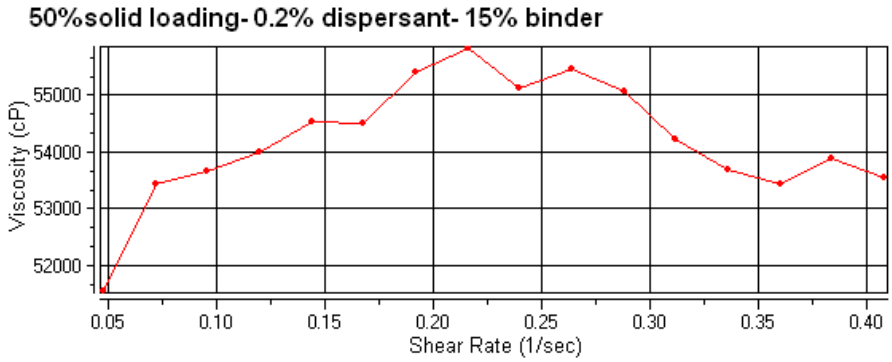

Figure 6.8. Viscosity and share rate plot for slurry with 50% solid loading, 0.2% dispersant and 15% binder.

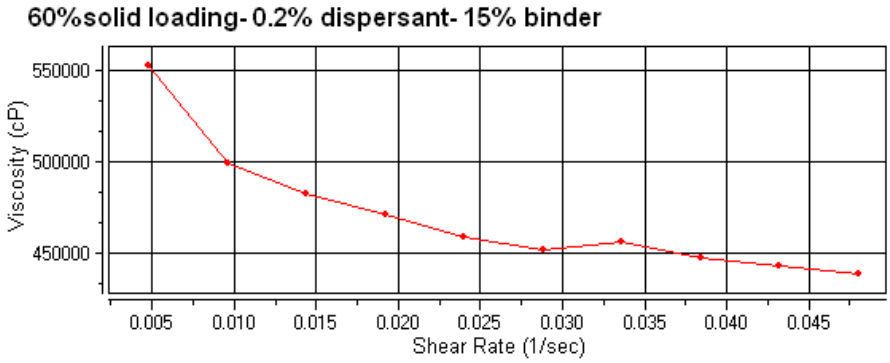

Figure 6.9. Viscosity and share rate plot for slurry with 60% solid loading, 0.2% dispersant and 15% binder.

The viscosities (measured at shear rate $0.08s^{-1}$) of different combinations was shown in Figure 6.10. An increase in the binder or solid loading concentrations results in a significant increase in the slurry viscosity. Between two factors, sold loading has more significant effects, since 20% increase of solid loading concentration results in more increase of viscosity than that caused by 25% increase of binder concentration.

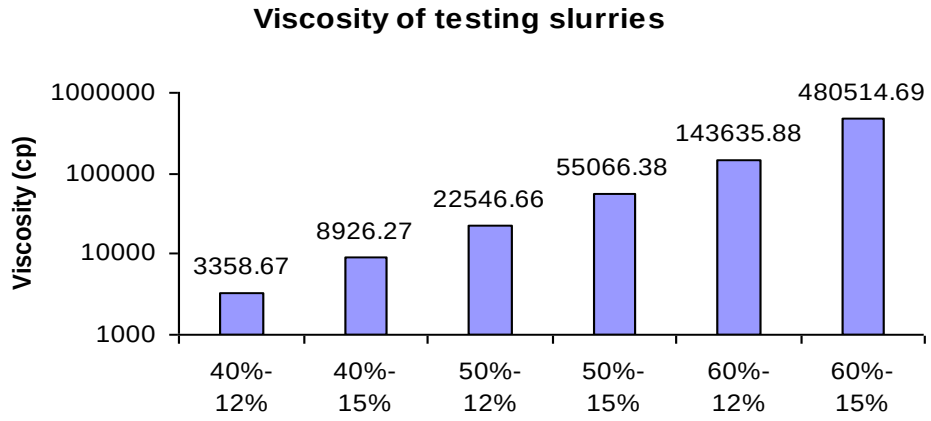

Figure 6.10. Viscosities of testing slurries

Figure 6.11 shows increase in viscosity with increase in the binder concentration from 12% to 15% (25% increases) for different solid loadings. Slurries at 40% and 50% solid loadings have more than twice increases in their viscosities. While a 60% solid loading slurry has up to 335% increase in the slurry viscosity for change of binder from 12 to 15%. The addition of different concentrations of binder media results in changing both the fluid viscosity and its rheological behavior. Comparing the increasing rate of 40% solid loading, the increasing rate of 50% is lower than that of 40%. It might due to their fluid properties different. Figure 6.12 shows the surface plot of viscosity vs. solid loading and binder concentrations to evaluate trend patterns. Slurries with low binder and solid loading concentrations had lower values of viscosity and vice versa. This trend is smooth.

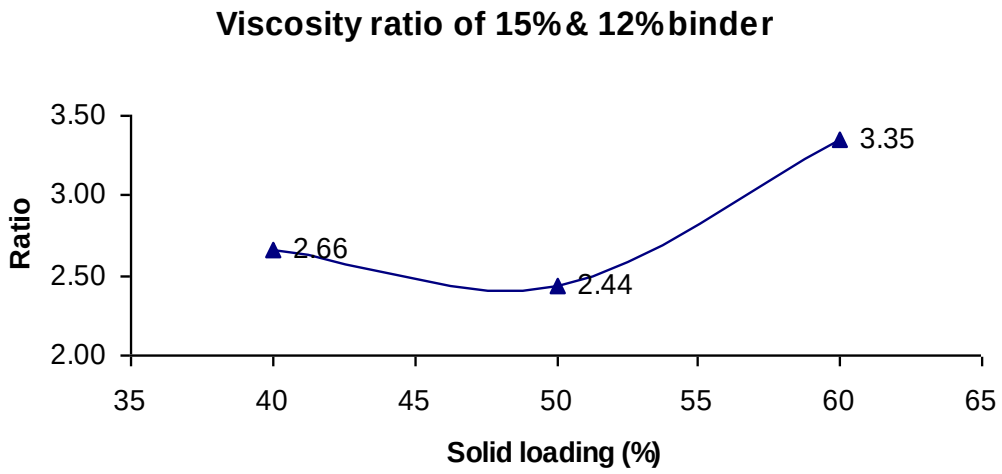

Figure 6.11. Solid loading vs. viscosity ratio of 15%:12% binder

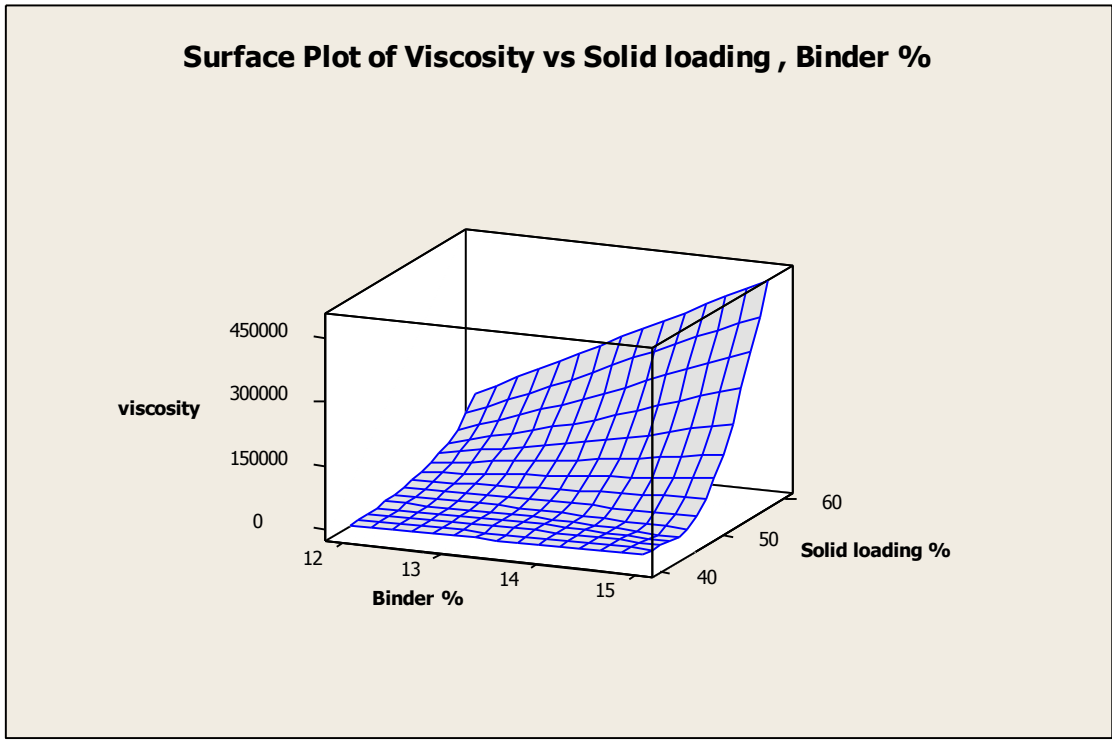

Figure 6.12. Surface plot of viscosity vs. solid loading and binder

An ANOVA analysis ((Table 6.3, Figure 6.13 and Figure 6.14) was conducted to evaluate the effect of solid loading, binder and their interaction effects on viscosity of the slurry. Based on ANOVA results it is evident that solid loading, binder and their interaction effects are statistically significant for the slurry's viscosity. However, solid loading has a higher effect on the slurry viscosity. This conclusion validates Figure 6.10. All slurries with higher solid loading have higher viscosity than those with lower solid loading.

6.3.3. Effect of solid loading and binder concentration on dimensions of LSCF lines. In this section the dimensions of the LSCF lines were studied using the direct write process. Slurries based on their solid loadings were extruded under 200kPa,

100kPa, and 30kPa. The slurries with 40% solid loading were written under 30kPa and 100kPa. However, 40% solid loading slurry was not extruded under 200kPa as the slurry had low viscosity which leads to rapid spreading on the substrate and creating line widths too wide for practical fuel cell designs.

Table 6.3. ANOVA table for solid loading, binder and viscosity

Source	DF	Seq SS	Adj SS	Adj MS	F	p
Solid Loading	2	2.24E+11	2.24E+11	1.12E+11	3.18E+04	0.00E+00
Binder	1	4.78E+10	4.78E+10	4.78E+10	1.35E+04	0.00E+00
Solid loading*Binder	2	6.93E+10	6.93E+10	3.46E+10	9.84E+03	0.00E+00
Error	6	2.11E+07	2.11E+07	3.52E+06		
Total	11	3.41E+11				
S=1875.61	R-sq=99.99%		R-Sq(adj)=99.99%			

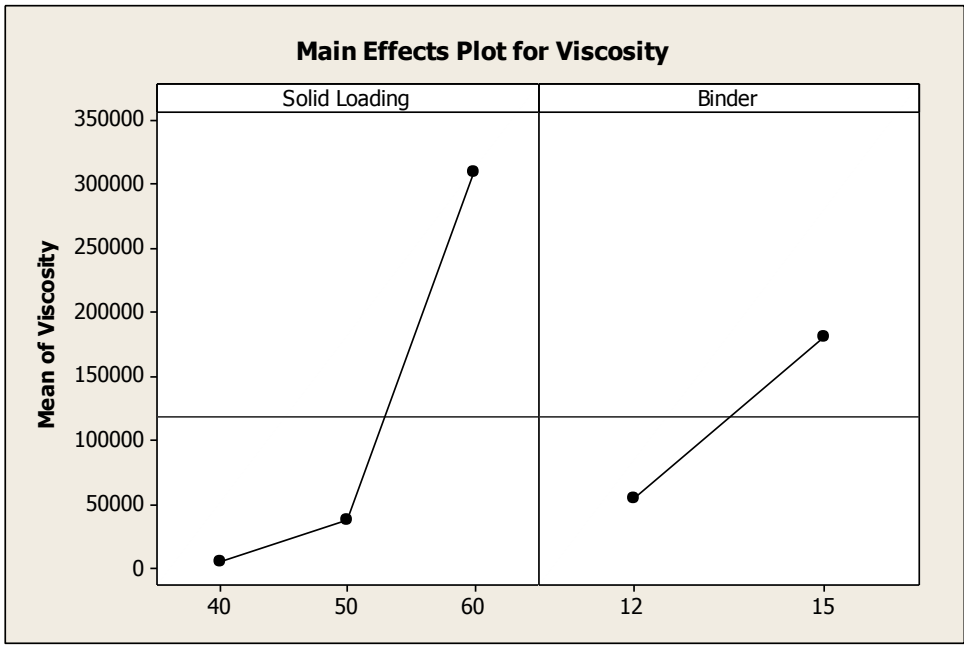

Figure 6.13. Main effects plot for viscosity vs. solid loading and binder

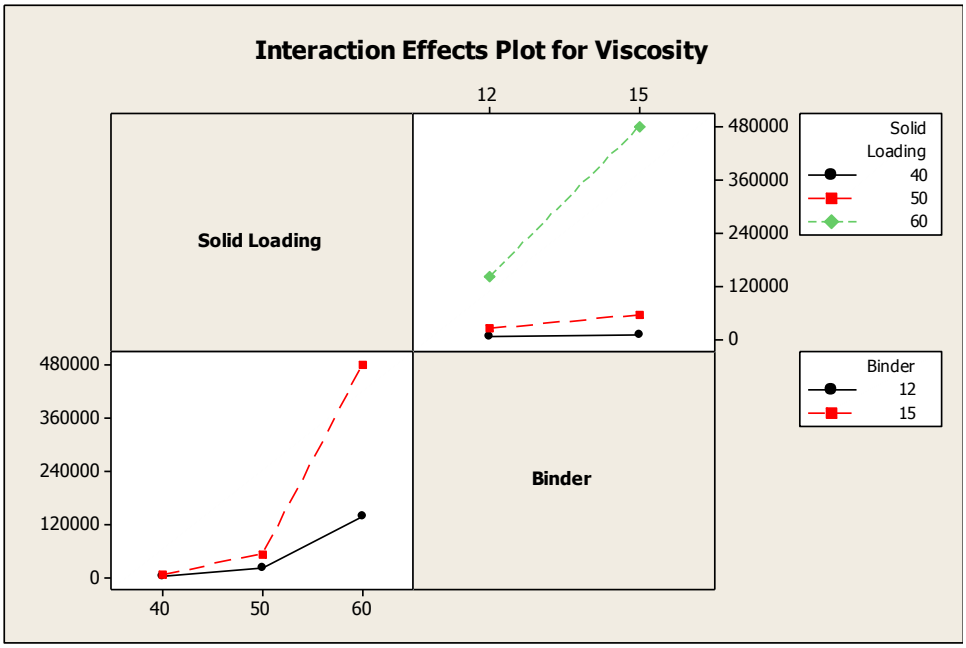

Figure 6.14. Interaction effects plot for viscosity vs. solid loading and binder

Figure 6.15 shows the width before sintering for 50% and 60% solid loading under 200kPa working pressure. Figure 6.16, shows the width before sintering for 40% and 50% solid loading under 100kPa working pressure. From the Figure 6.15 and Figure 6.16 it is evident as the binder and solid loading concentration is increased the line width reduces. However, an increase by 20% solid loading results in a higher width reduction than that caused by an increase in 25% of binder concentration. Thus, it can be concluded that solid loading concentrations affect the written line's width more significantly.

Figures 6.17 and Figure 6.18 show the dimensions of the lines before sintering for different constituent concentrations. It can be seen that the solid loading affects written line's dimensions more significantly. This is because the solid loading affects the viscosity of the slurries which further impacts the dimensions of the line. However, there

is an exception, for the slurry with 40% solid loading and 15% binder, the height is higher than that of 40% solid loading and 12% binder. There is a similar trend for 50% solid loading.

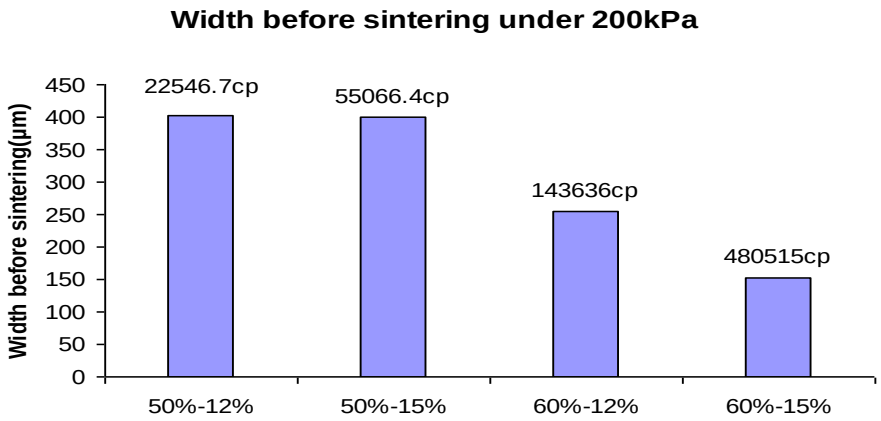

Figure 6.15. Slurry combinations vs. line width before sintering under 200kPa

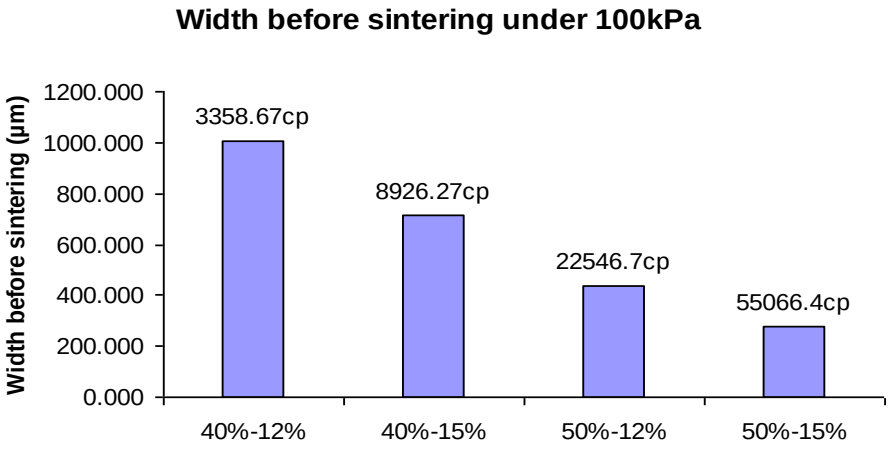

Figure 6.16. Slurry combinations vs. line width before sintering under 100kPa

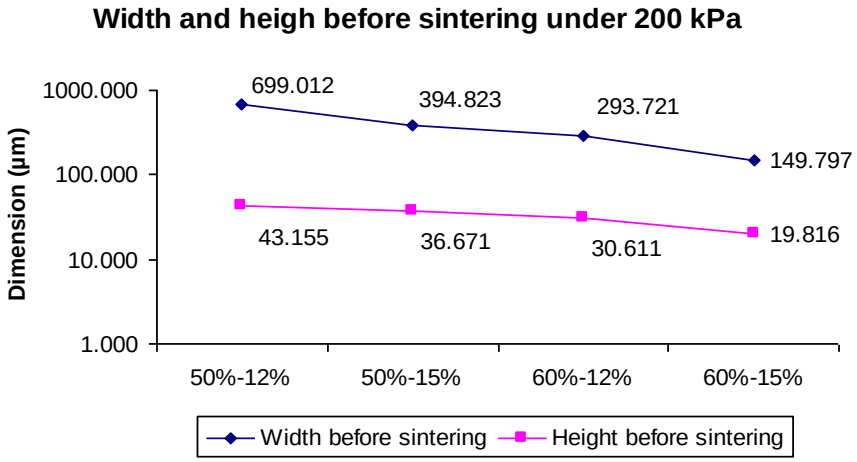

Figure 6.17. Slurry combinations vs. line height before sintering under 200kPa

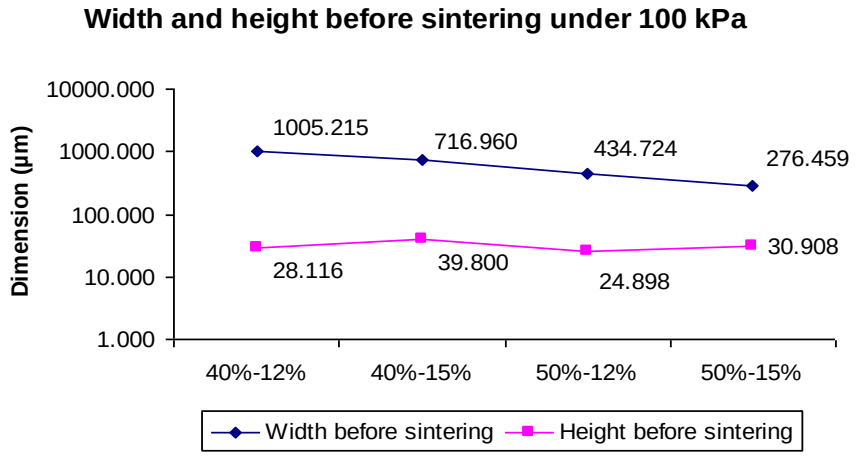

Figure 6.18. Slurry combinations vs. line height before sintering under 100kPa

The dimensional characteristics of the cathode trace can be explained by the aspect ratio of the line. In this case, the aspect ratio equals to width over height. Figure 6.19 and Figure 6.20 show the aspect ratio under 200kPa and 100kPa, respectively. The aspect ratio is affected by the rheological properties of the slurry. An increase in the

viscosity of the slurry leads to a lower aspect ratio and vice versa. An increase in the solid loading and binder leads to reduction in the aspect ratio. This can be attributed to the fact that a slurry with higher solid loading and binder concentration has higher viscosity which further affects the aspect ratio.

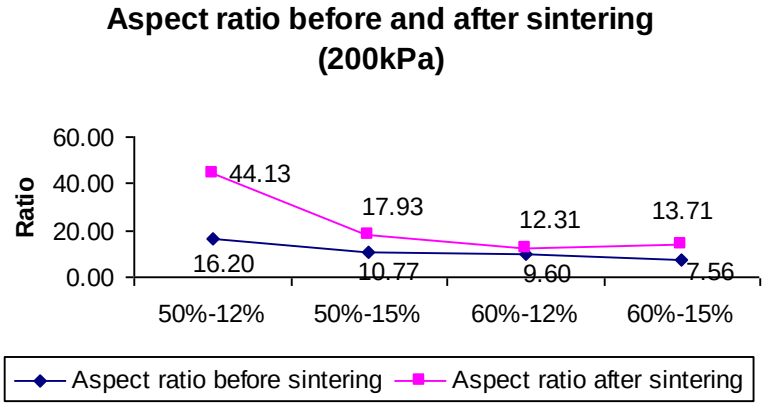

Figure 6.19. Aspect ratio before and after sintering under 200kPa

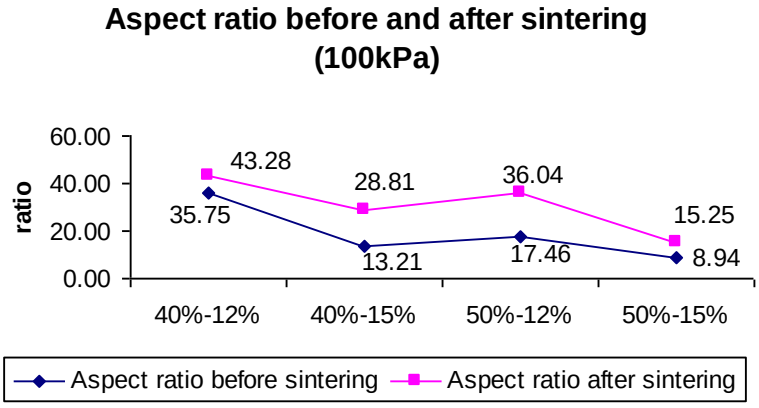

Figure 6.20. Aspect ratio before and after sintering under 100kPa

6.3.4. Evaluation of dimensional shrinkage of the LSCF lines. During the sintering, the additive and solvent are decomposed resulting in line width and height shrinkage. The additive (PVB binder, Triton dispersant) and solvent (α-terpineol) decomposition and removal are a complex process as described in section 6.2.2. The shrinkage in the line's width and height affect its resistance. This section evaluates the concentration of solid loading and binder's effect on shrinkage of slurries, in order to understand how to control the shrinkage of the LSCF.

Figure 6.21 shows the width and height shrinkage of 40% and 50% solid loading slurries under 100kPa. Shrinkage of width reduced when solid loading and binder increased, except for the slurry with 40% solid loading and 12% binder. Figure 6.22 shows the width and height shrinkage of 50% and 60% solid loading slurries under 200 kPa. Shrinkage of width increased when solid loading and binder increased. However, shrinkage of height decreased when binder increased.

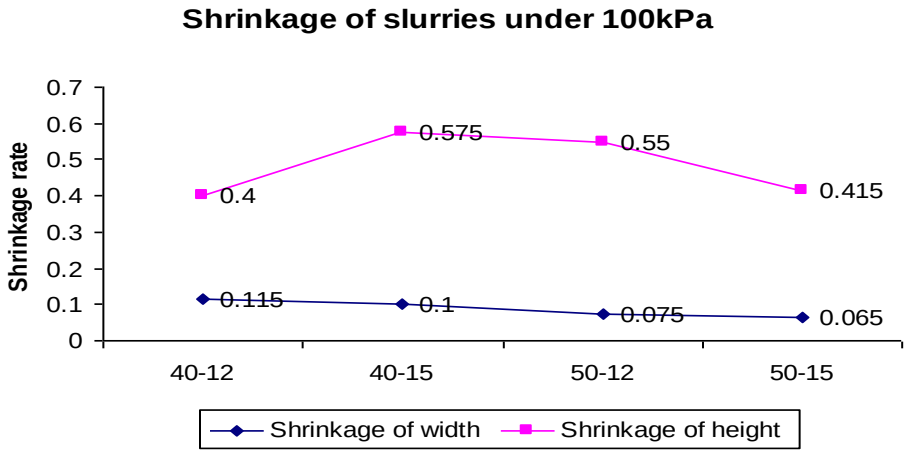

Figure 6.21. Shrinkage of 40%-50% slurries under 100kPa

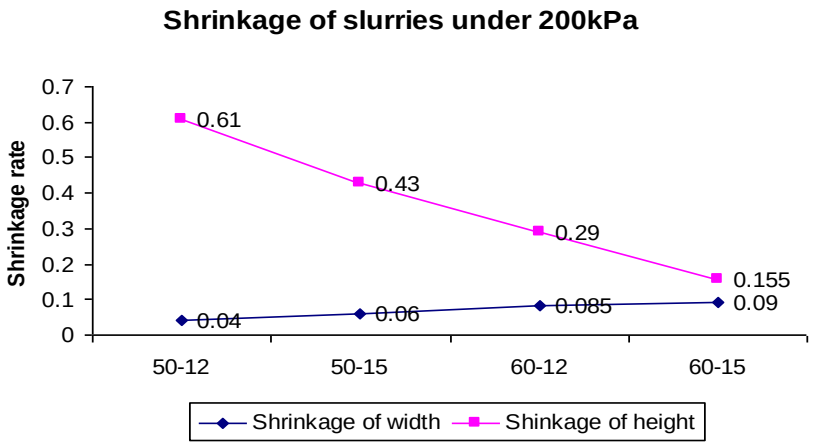

Figure 6.22. Shrinkage of 50%-60% slurries under 200kPa

In order to understand the relationship among shrinkage, solid loading and binder concentration, a DOE was conducted. Table 6.4 shows the ANOVA results for width shrinkage (200kPa). All of the main and interaction effects are statistically significant on the width shrinkage. The concentration of the binder is the most significant factor. As discussed in Chapter 5, the viscosity of slurry is dependent on the concentration of its solid loading.

Table 6.4. ANOVA table for solid loading, binder and width shrinkage (200kPa)

Source	DF	Seq SS	Adj SS	Adj MS	F	P
Solid Loading	1	0.0162	0.0162	0.0162	43.20	0.0030
Binder	1	0.1104	0.1104	0.1104	294.53	0.0000
Solid loading*Binder	1	0.1152	0.1152	0.1152	307.20	0.0000
Error	4	0.0015	0.0015	0.0004		
Total	7	0.2434				
S = 0.0193649	R-sq = 99.38%		R-Sq(adj) = 98.92%			

Figure 6.23 illustrates the surface and interfacial tension, which result in the shrinkages of the line dimensions. The compositions of the slurries directly impact of these two tensions and their ratio. Generally, as sintering out of solvent and other organic components, the lower viscosity slurry will have a larger shrinkage. Table 6.5 shows the ANOVA results for height shrinkage under 200kPa. At a 95% significant level both the solid loading and binder are significant.

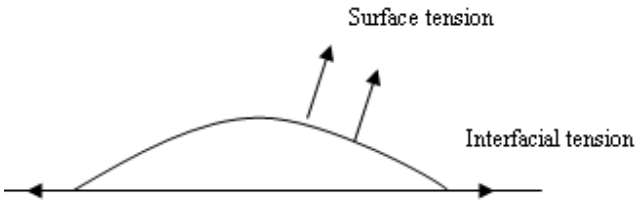

Figure 6.23. Surface tension and interfacial tension

Table 6.5. ANOVA table for solid loading, binder and height shrinkage (200kPa)

Source	DF	Seq SS	Adj SS	Adj MS	F	p
Solid Loading	1	0.1770	0.1770	0.1770	59.7500	0.0020
Binder	1	0.0496	0.0496	0.0496	16.7500	0.0150
Solid loading*Binder	1	0.0010	0.0010	0.0010	0.3400	0.5900
Error	4	0.0119	0.0119	0.0030		
Total	7	0.2395				
S = 0.0544289 R-Sq = 95.05% R-Sq(adj) = 91.34%						

Figure 6.24 shows the main effects and interaction effects for width shrinkage under 200kPa. The concentration of the binder plays an important role on width

shrinkage. This can be explained as the binder's long molecular chains increase the intermolecular forces, which result in higher interfacial tension and surface tension.

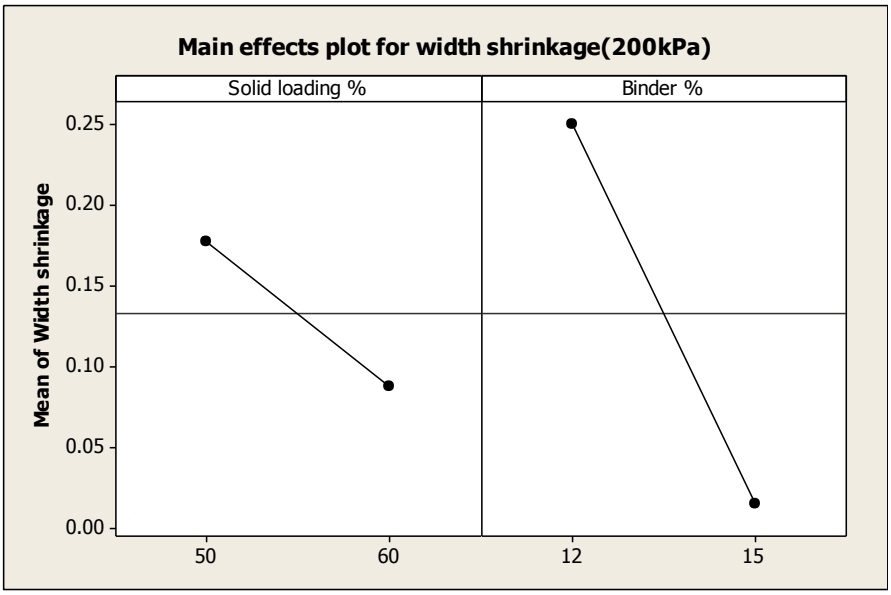

(a)

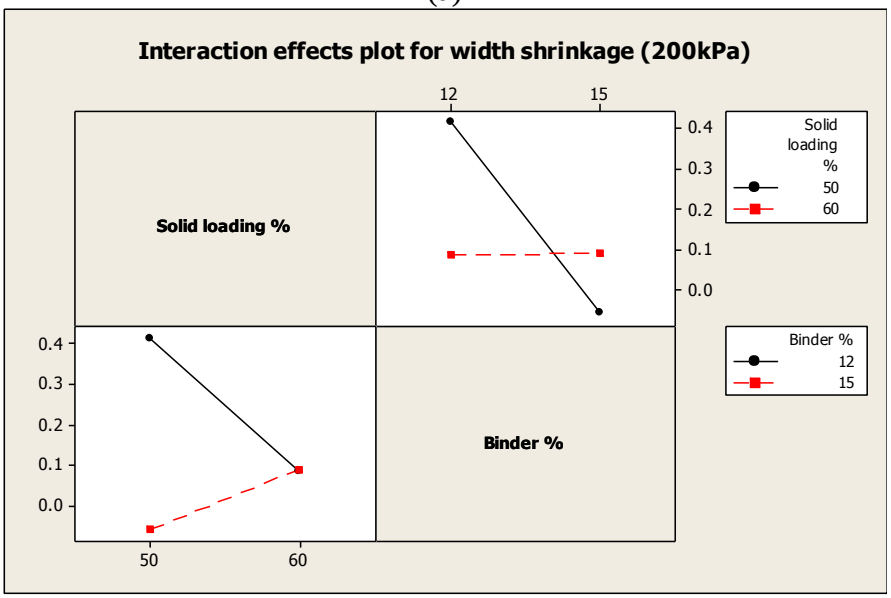

(b)

Figure 6.24. (a) Main effects plot and (b) Interaction effects plot for width shrinkage under 200kPa

Figure 6.25 shows the main effects and interaction effects for height shrinkage under 200kPa. The concentration of the solid loading plays an important role on it. The interaction between solid loading and binder are not significant at 95% level.

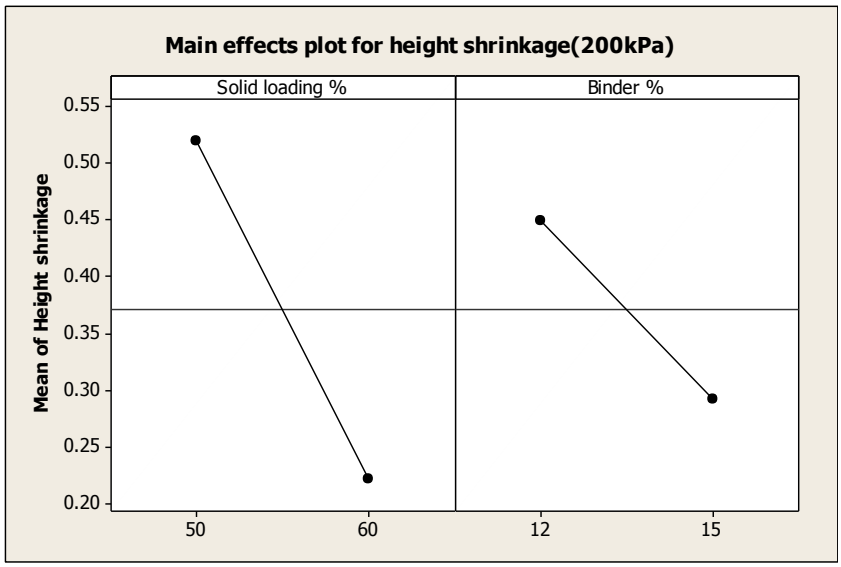

(a)

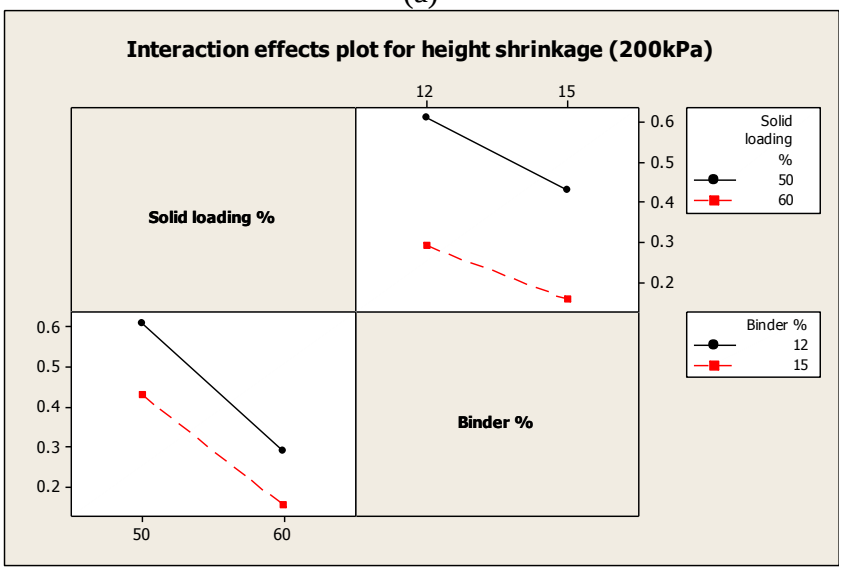

(b)

Figure 6.25. (a) Main effects plot and (b) Interaction effects plot for height shrinkage under 200 kPa

Table 6.6 and Table 6.7 show the ANOVA results for width and height shrinkage under 100kPa, respectively. At a 95% significant level, solid loading and interaction of the solid loading and binder are significant. Binder's effects are not significant for width and height shrinkage.

Table 6.6. ANOVA table for solid loading, binder and width shrinkage (100kPa)

Source	DF	Seq SS	Adj SS	Adj MS	F	P
Solid Loading	1	0.1152	0.1152	0.1152	8.4900	0.0440
Binder	1	0.0085	0.0085	0.0085	0.6200	0.4740
Solid loading*Binder	1	0.1513	0.1513	0.1513	11.1400	0.0290
Error	4	0.0543	0.0543	0.0136		
Total	7	0.3292				
S = 0.116512 R-Sq = 83.51% R-Sq(adj) = 71.13%						

Table 6.7. ANOVA table for solid loading, binder and height shrinkage (100kPa)

Source	DF	Seq SS	Adj SS	Adj MS	F	p
Solid Loading	1	0.0406	0.0406	0.0406	3.1600	0.1500
Binder	1	0.0091	0.0091	0.0091	0.7100	0.4470
Solid loading*Binder	1	0.1830	0.1830	0.1830	14.2600	0.0200
Error	4	0.0514	0.0514	0.0128		
Total	7	0.2841				
S = 0.113303 R-Sq = 81.92% R-Sq(adj) = 68.37%						

Figures 6.26 and Figure 6.27 show that when solid loading was increased, both the width shrinkage and height shrinkage increased significantly under 100kpa. Also, when binder was increased, the width shrinkage reduced and the height shrinkage increased. This can be explained by the fact that for low viscosity slurries, the slurry can

be extruded easier than high viscosity one. This results in a higher aspect ratio. Thus, the interfacial tension plays an important role on the width and height shrinkage. Also, other direct-writing parameters affect shrinkage of the cathode lines.

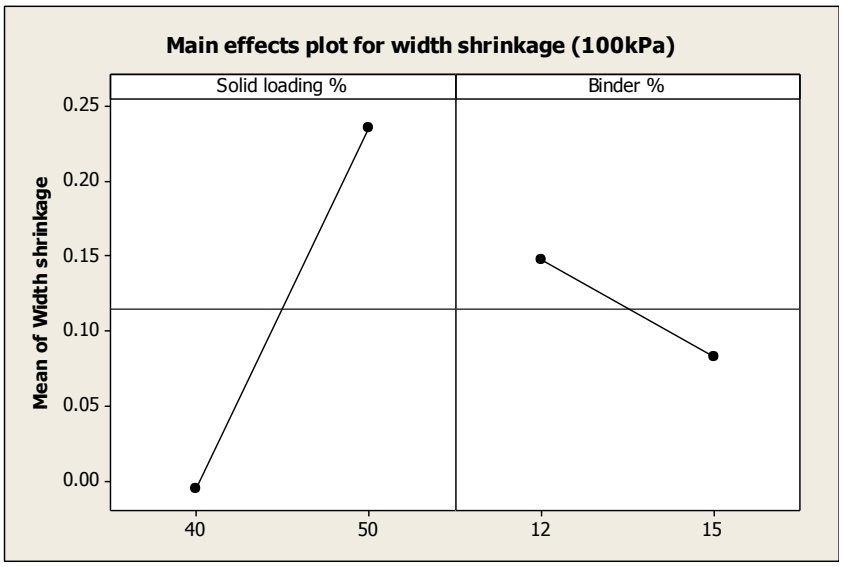

(a)

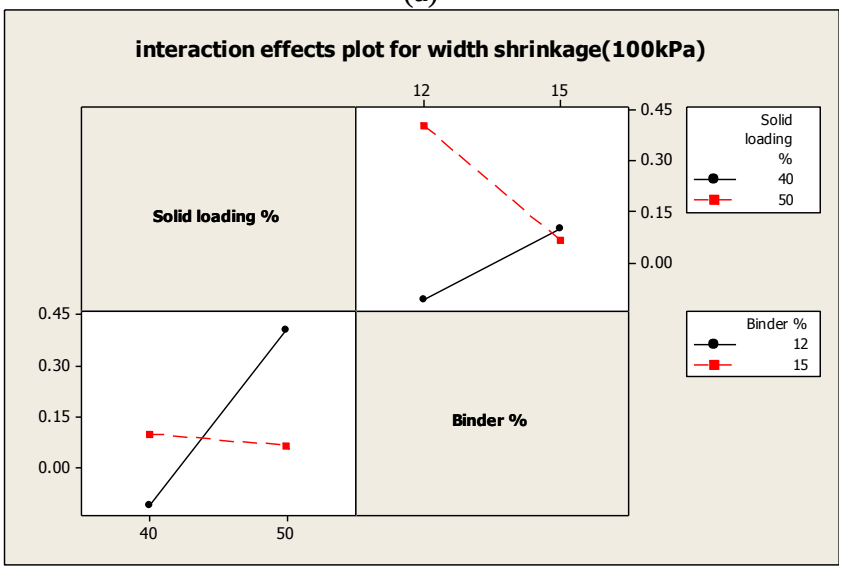

(b)

Figure 6.26. (a) Main effects plot and (b) Interaction effects plot for width shrinkage under 100kPa

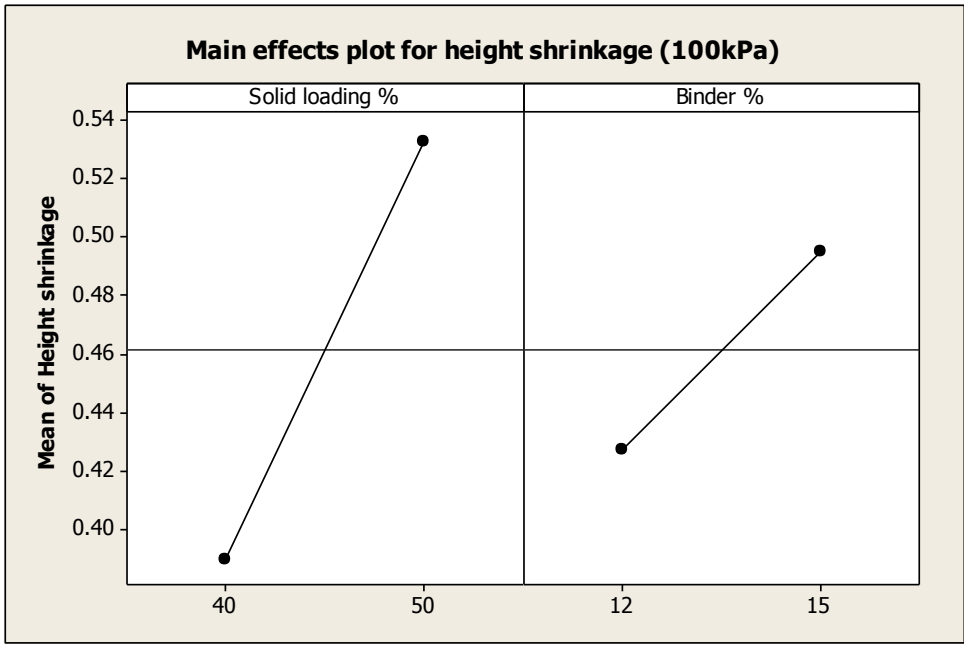

(a)

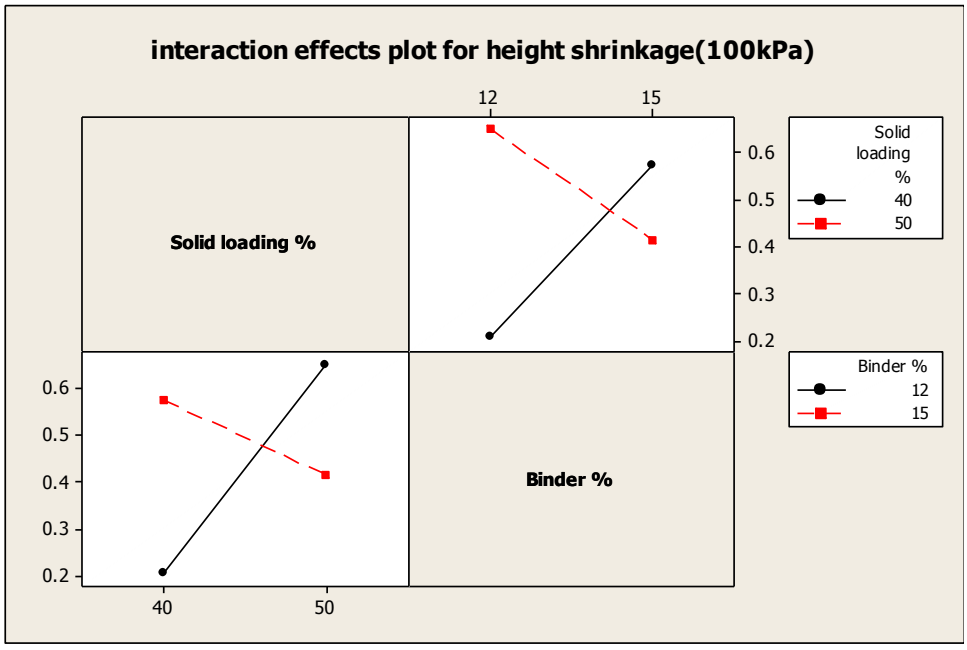

(b)

Figure 6.27. (a)Main effects plot and (b) Interaction effects plot for height shrinkage under 100kPa

6.3.5. Evaluation of electrical resistance of the cathode lines. Generally, the resistance of the cathode lines is dependent on the slurry's solid loading, line's microstructure, and cross-section dimensions. This section will evaluate these factors. Figure 6.28 shows a plot of resistance vs. solid loading and binder concentrations to evaluate trend patterns. Slurries with low binder concentrations had lower values of resistance and vice versa. The lines written by 60% solid loading and 15% binder had the highest resistance and the line with 40% solid loading and 12% binder had the lowest resistance. At lower binder concentrations, the line written by 50% solid loading had relative higher resistance than that written by 60% solid loading. However, for the higher binder concentrations, resistance increased with solid loading concentrations.

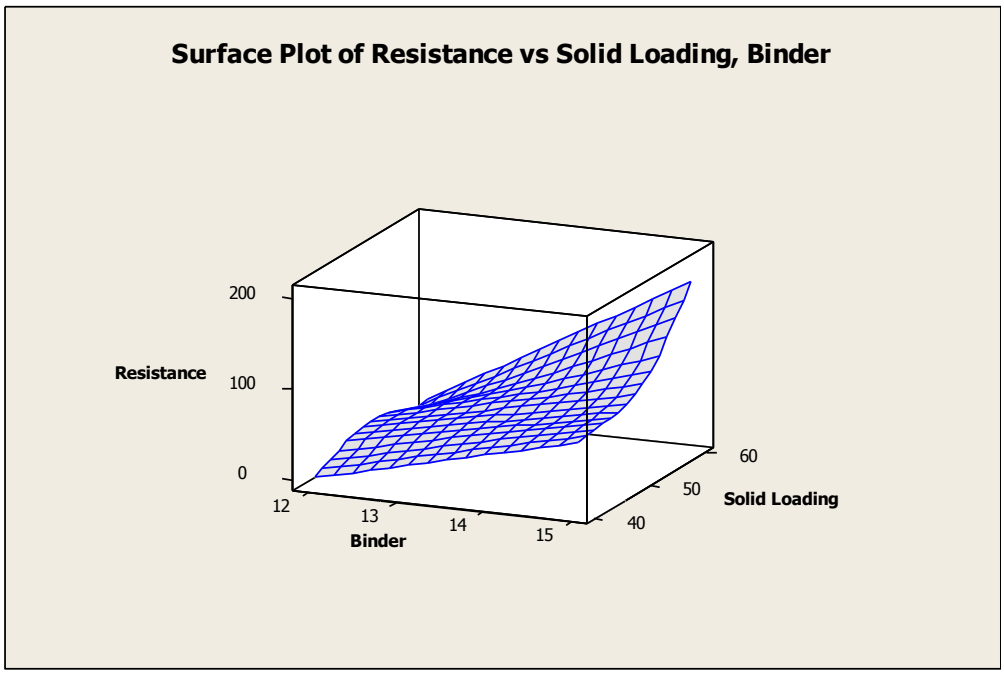

Figure 6.28. Surface plot of resistance vs. solid loading and binder

Table 6.8 and 6.9 show the effect of solid loading and binder concentrations on the resistance of the cathode lines at 200 and 100kPa extrusion pressure respectively. Both binder and solid loading factors have statistically significant effect on the resistance of the cathode trace. Figures 6.33 to 6.36 show that an increase in the concentration of the binder results in an increase of the resistance. A higher concentration of binder results in higher porosity of the microstructure. That results in lower connectivity of the LSFC material thereby increasing the resistance of the line.

Table 6.8. ANOVA table for solid loading, binder and resistance (100kPa)

Source	DF	Seq SS	Adj SS	Adj MS	F	P
Solid Loading	1	846.3	846.3	846.3	24.0100	0.0080
Binder	1	8691.1	8691.1	8691.1	246.5500	0.0000
Solid loading*Binder	1	34.0	34.0	34.0	0.9600	0.3820
Error	4	141.0	141.0	35.3		
Total	7	9712.4				
S = 5.93728 R-Sq = 98.55% R-Sq(adj) = 97.46%						

Table 6.9. ANOVA table for solid loading, binder and resistance (200kPa)

Source	DF	Seq SS	Adj SS	Adj MS	F	P
Solid Loading	1	12335	12335	12335	27.45	0.006
Binder	1	17581	17581	17581	39.12	0.003
Solid loading*Binder	1	8947	8947	8947	19.91	0.011
Error	4	1798	1798	449		
Total	7	40660				
S = 21.1993 R-Sq = 95.58% R-Sq(adj) = 92.26%						

In the case of the solid loading, a higher LSCF concentration should result in lower resistance due to larger number of molecules to transfer the free electrons. However, from Figures 6.29 and 6.30, it can be observed that higher solid loading slurries show higher resistance, which is contrary to the above explanation. This is because at higher solid loading concentrations the viscosity of the slurry increases which results in the extrusion of lower cross-sectional areas for the cathode trace. Thus, though the inherent material conductivity of the LSCF at 60% solid loading is higher than at lower concentrations, the dimensions of the line are much smaller resulting in higher resistance of the cathode trace. Thus, it is important to present the resistance data of cathode lines with respect to cross section area data to make accurate judgments.

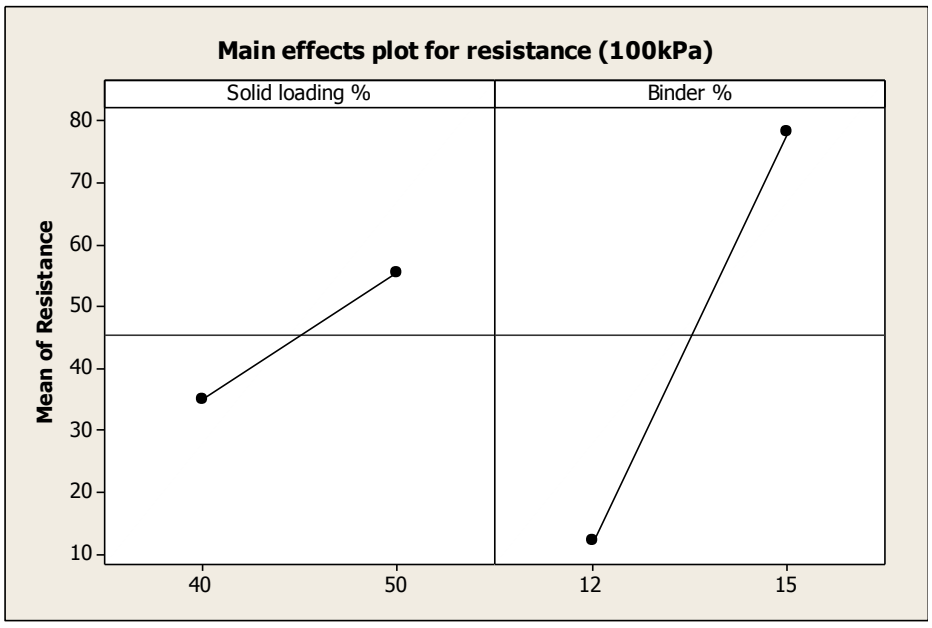

(a)

Figure 6.29. (a) Main effects plot for resistance vs. 40% and 50% solid loading under 100kPa

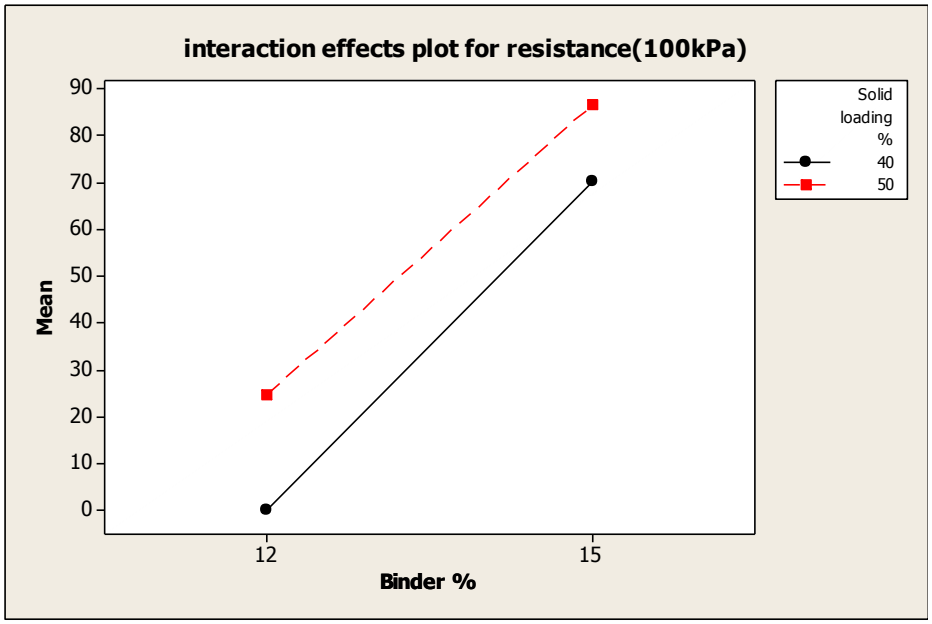

(b)

Figure 6.29. (b) Interaction effects plot for resistance vs. 40% and 50% solid loading under 100kPa

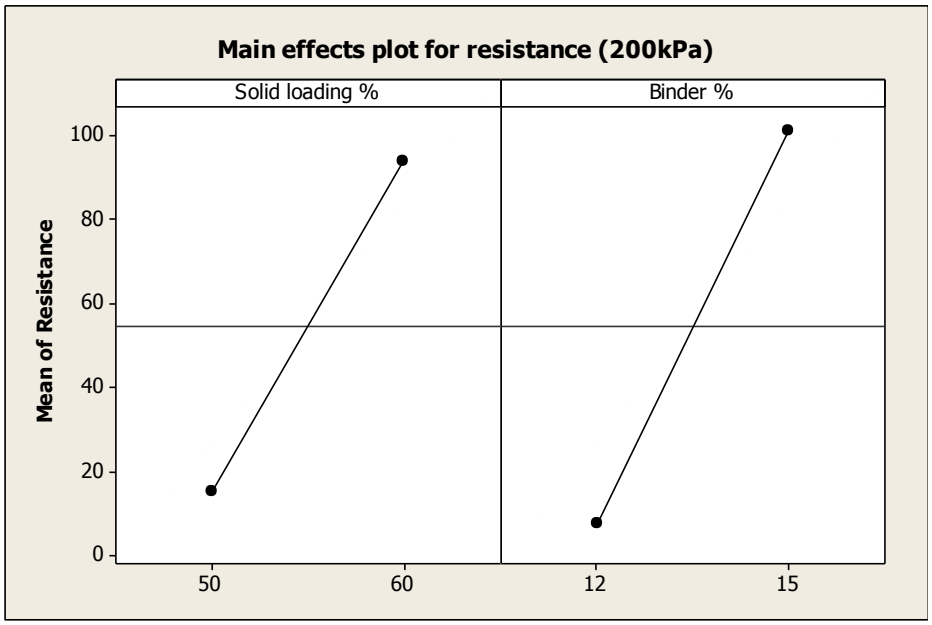

(a)

Figure 6.30. (a) Main effects plot for resistance vs.50% and 60% solid loading under 200kPa

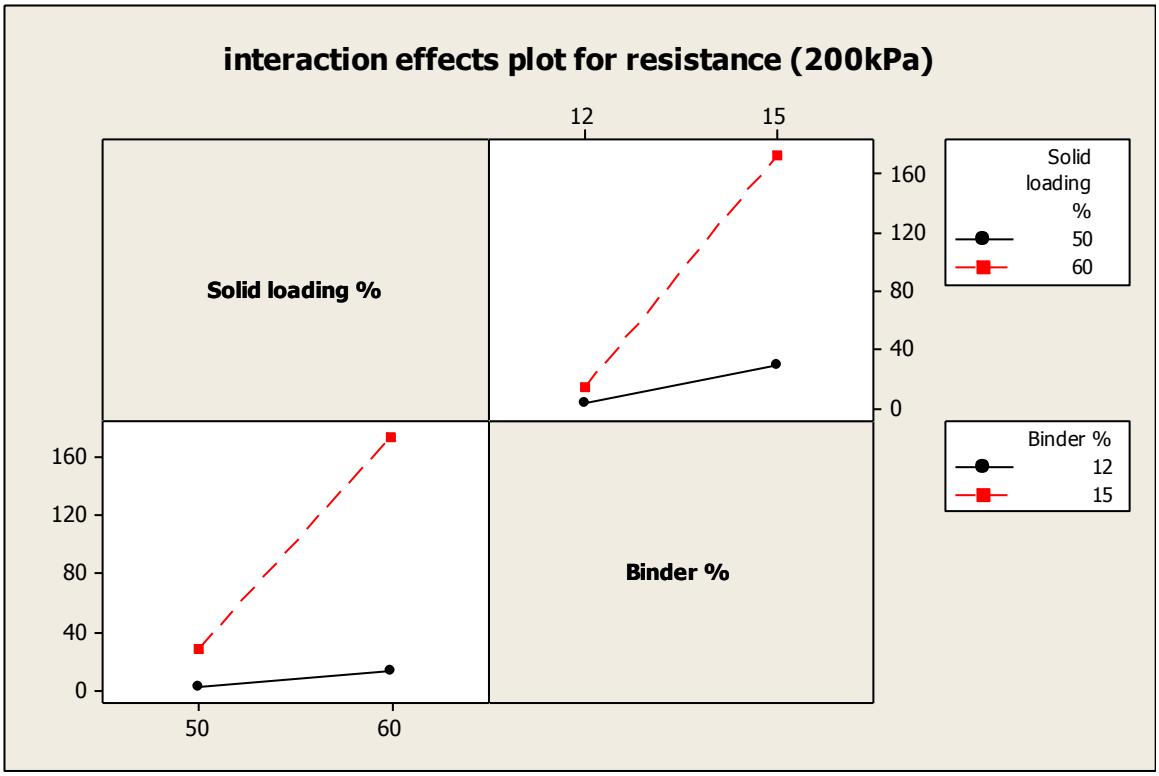

(b)

Figure 6.30. (b) Interaction effects plot for resistance vs.50% and 60% solid loading under 200kPa

Figure 6.31 (a) shows the main effects plot for resistance with respect to solid loading concentration, binder concentration and cross section (CS) area. For the cross-section (CS) area, 1 denotes smaller cross section and 2 denotes larger cross section. As seen from the Figure 6.31(a), a larger cross section results in a lower resistance. Also, from 6.31(b) (interaction effects plot), it can be seen that the cross section area plays an important role for a slurry with high solid loading. For slurry with lower solid loading or lower binder concentration, the effect from cross section area was marginal.

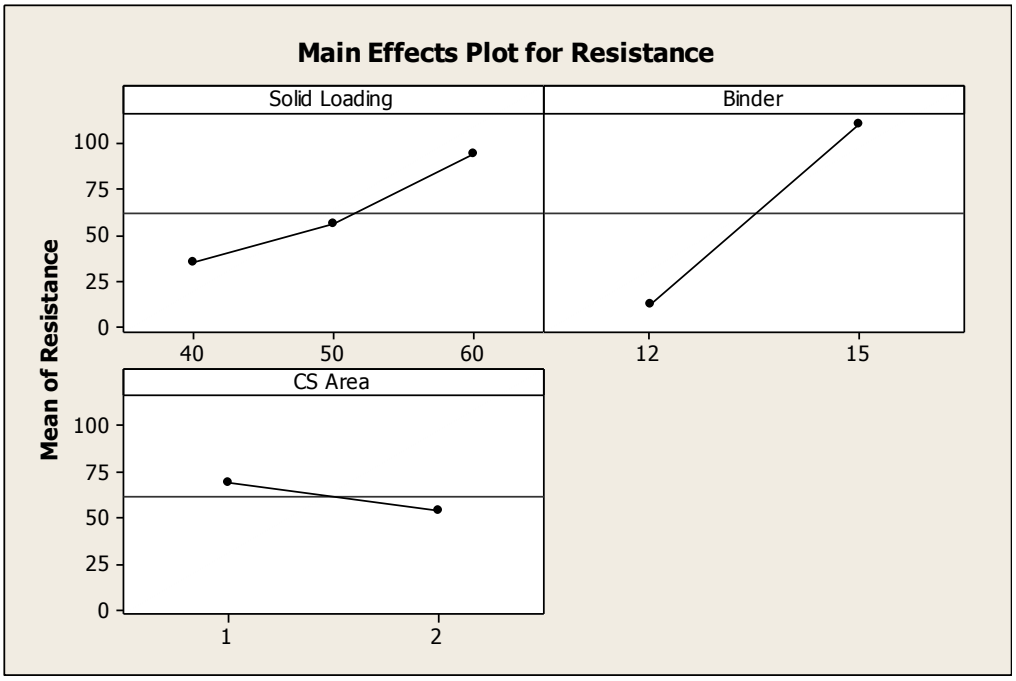

(a)

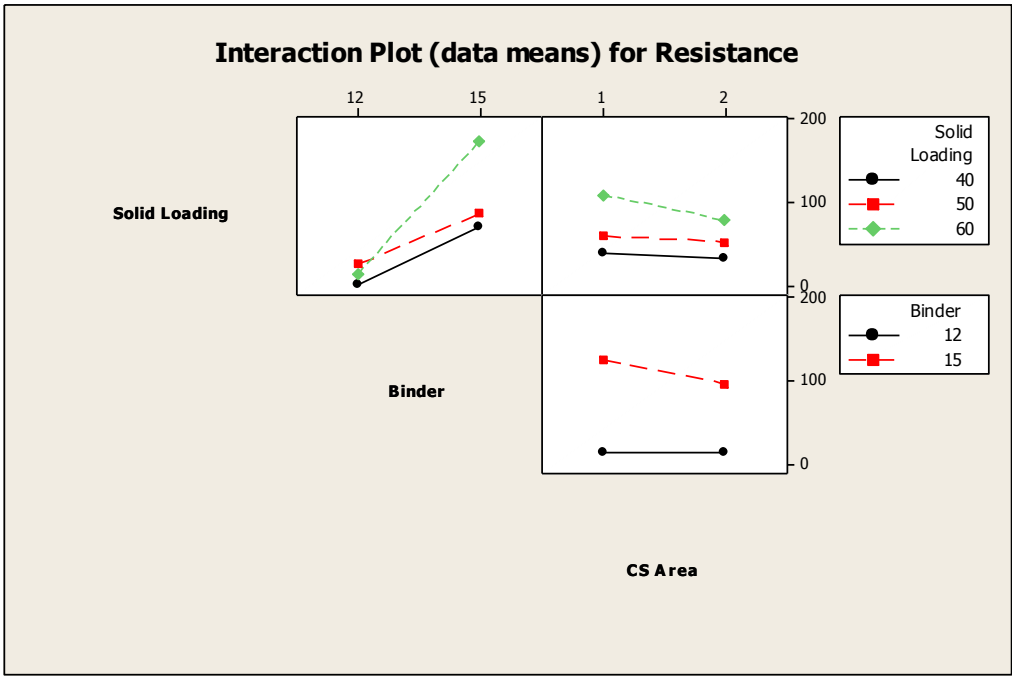

(b)

Figure 6.31. (a) Main effect plot and (b) Interaction effects plot for resistance vs. solid loading, binder and cross section area

6.4. Conclusion

In this study, the effects of solid loading and binder on the cathode line dimensions were evaluated. In addition to optimal dispersant concentration, solid loading and binder are the other two major factors that affect the direct writing process. These two factors are evaluated to observe their effect on cathode line dimension, microstructure and electrical resistance. Solid loading and binder not only affect the slurry's viscosity, but also affect the slurry's rheology behavior. From this study, solid loading plays a more important role on both rheology behavior and line dimension. Further, aspect ratio and dimensional shrinkage were studied which are important for the combined direct writing and photolithography fabrication method. Different slurry composition were evaluated to identify optimal slurry which can generate a lower line width and lower electrical resistance. Based on the findings of this research, a slurry with 50% solid loading, 12% binder and 0.2% dispersant was chosen to conduct direct writing parameters research.

CHAPTER 7

Understanding of Direct Writing Process Parameters

7.1. Introduction

In section 3.4.4, the direct writing technology was introduced. The direct writing process was used to generate the required micro structure of anode and cathode electrodes by controlling different process parameters of interest. These include the pressure, velocity, mixture ratio of the slurry and the nozzle to substrate distance. After annealing, the shapes of the extruded electrodes were retained.

The composition of slurries affected their fluidity that was a critical factor for the extrusion process. In chapter 5, the rheology properties of the slurries with different dispersant compositions were studied. In chapter 6, the effects of LSCF slurry solid loading and binder concentrations on cathode dimensions, microstructure and resistance were evaluated. However, the microstructure of electrode pattern lines is not only affected by the slurry's concentration ratio but also affected by the extrusion parameters, such as nozzle size, nozzle speed, distance between the nozzle and substrate, pressure in the slurry chamber, and the diffusion rate of electrolyte substrate. In this chapter, the effects of extrusion parameters were evaluated and optimized.

7.2. Experimental Design for Direct Writing Process Parameters

In this chapter, three direct writing process parameters were considered: (1) speed of nozzle, (2) distance between nozzle and substrate, and (3) pressure in the slurry chamber. Substrates with consistent surface preparation were prepared. Based on the findings from Chap 6, it is noted that a cathode electrode is desirable for low resistance and lower line width. Based on this reason, a slurry with 50% solid loading, 12% binder and 0.2% dispersant was chosen to conduct direct writing parameters research. For comparison purposes, a slurry with 60% solid loading, 12% binder and 0.2% dispersant was tested. The slurries were tested using a 100μm nozzle.

A full factorial experimental design with three factors (k=3) was considered. Each of the three factors had two levels. The writing speeds were chosen as 0.5 mm/s (-) and 1mm/s (+). The operating pressures were chosen at two levels as shown in Table 7.1. For a slurry with 50% solid loading, the low level was 100kPa (-), and high level was 200kPa (+). For 60% solid loading, the low level was 200 kPa (-), and high level was 300kPa (+). The distance between nozzle and substrate had two levels: 100μm (-) and 200μm (+).The 2^3 (k=3) full factorial experiment design is shown in the Table 7.2.

Table 7.1. Factor level settings

Level	Pressure	Distance	Speed
Low (-)	100kPa (for 50%) 200kPa (for 60%)	100 μm	0.5mm/s
High (+)	200kPa (for 50%) 300kPa (for 60%)	200 μm	1mm/s

Table 7.2. 2^3 full factorial design pattern

Run	Combination	Factors		
		A(Distance)	B(Speed)	C(Pressure)
1	(1)	-	-	-
2	A	+	-	-
3	B	-	+	-
4	AB	+	+	-
5	C	-	-	+
6	AC	+	-	+
7	BC	-	+	+
$8 = 2^3$	ABC	+	+	+

7.3. Experimental Methodology

The cathode slurry was written on the YSZ electrolyte substrate under each combination twice to provide a replicate. Cathode lines were observed by Zeiss microscope before and after sinter. Top and profile images of cathode lines were recorded. Image-pro plus software was used to check the width and height of the lines before and after sinter. Signatone Pro4 and Keithley 2400 series source meter were used to detect the sintered lines' resistance.

7.4. Result and Discussion

7.4.1. Data collection. Based on the Table 7.2 shown, a full factorial design was used to analyze the output responses, which included line width, height and electrical resistance. Table 7.3 shows output responses for the slurry with 50% solid loading, 12% binder and 0.2% dispersant. For the combination: distance = 200μm, speed = 1mm/s and pressure = 100kPa (exp no. 5), the slurry could not be extruded. For the combination:

distance = 200µm, speed = 0.5mm/s and pressure = 100kPa (exp. no. 2), a minimal resistance of around 3.6-5.6KΩ was obtained.

Table 7.4 shows the output responses for the slurry with 60% solid loading, 12% binder and 0.2% dispersant. For the combinations, (1) distance = 100µm, speed = 0.5mm/s and pressure = 300kPa (exp. no. 4) and (2) distance = 200µm, speed = 1mm/s and pressure = 200kPa (exp. no 5), the slurry could not be extruded smoothly. In these experiments dotted lines were written on the substrate. For combinations, exp. no. 3 and exp. no. 8, the extrusion process did not yield stable results. The combination, distance = 200µm, speed = 0.5mm/s and pressure = 300kPa (exp. no. 7) gave the lowest values of resistance

7.4.2. Statistical analysis. Since dimensional data was incomplete for 60% solid loading slurry, the DOE analysis was focused on the 50% solid loading, 12% binder and 0.2% dispersant combination. Also, the 50% solid loading slurry was preferred slurry for investigation as it had the lowest resistance among all slurries studied. Table 7.5 showed that the main effects of distance, pressure and their interaction were statistically significant with respect to resistance. Figure 7.1 showed that an increase in the distance, speed and pressure of the direct writing process results in the increase of the cathode trace resistance.

Table 7.3. Output responses for 50% solid loading, 12% binder and 0.2% dispersant

No.	Direct writing parameters			Before sintering		After sintering		Shrinkage of width	Shrinkage of height	Resistance (KΩ)
	Distance	Speed	Pressure	Width (μm)	Height (μm)	Width (μm)	Height (μm)			
1	-	-	-	503.90	31.5	467.2	25.80	0.07	0.18	22.000
1	-	-	-	394.70	11.2	375.5	20.50	0.05	-0.83	101.900
2	+	-	-	447.60	19.7	475.5	24.70	-0.06	-0.26	5.680
2	+	-	-	441.40	30.5	407.8	23.80	0.08	0.22	3.690
3	-	+	-	298.70	35.9	294.6	20.80	0.01	0.42	57.760
3	-	+	-	289.70	22.6	283.3	20.50	0.02	0.09	69.450
4	-	-	+	614.90	31.8	617.6	27.70	0.00	0.13	22.000
4	-	-	+	697.10	34.7	609.7	28.60	0.13	0.17	235.500
5	+	+	-	000.0*	00.0	000.0	00.0*	1.00	1.00	10000.0**
5	+	+	-	000.00	00.0	000.0	00.00	1.00	1.00	10000.000
6	-	+	+	444.20	29.4	463.1	27.20	-0.04	0.08	3.150
6	-	+	+	407.10	22.9	416.7	28.20	-0.02	-0.23	8.350
7	+	-	+	381.90	26.1	363.9	23.90	0.05	0.08	104.700
7	+	-	+	379.90	24.6	412.9	24.20	-0.09	0.02	236.700
8	+	+	+	348.60	25.7	326.5	16.30	0.06	0.37	1407.000
8	+	+	+	353.40	27.7	331.0	16.70	0.06	0.40	498.500

Nomenclature:

* That width and height equals to 0 denotes that the slurry was not extruded.

** For dotted line and no line written, the resistance was shown as 10000 KΩ.

Table 7.4. Output responses for 60% solid loading, 12% binder and 0.2% dispersant

No.	Direct writing parameters			Before sintering		After sintering		Shrinkage of width	Shrinkage of height	Resistance (KΩ)
	Distance	Speed	Pressure	Width (μm)	Height (μm)	Width (μm)	Height (μm)			
1	-	-	-	262.60	24.6	252.1	16.7	0.04	0.32	15.040
1	-	-	-	270.80	24.6	245.9	15.3	0.09	0.38	5.910
2	+	-	-	255.10	22.5	243.8	19.9	0.04	0.12	4.740
2	+	-	-	262.60	23.8	239.6	18.1	0.09	0.24	9.010
3	-	+	-	201.00	12.4	197.3	14.6	0.02	-0.18	20.650
3	-	+	-	0.5*	0.5	0.5	0.5	1.00	1.00	10000.0**
4	-	-	+	0.50	0.5	0.5	0.5	1.00	1.00	10000.00
4	-	-	+	0.50	0.5	0.5	0.5	1.00	1.00	10000.00
5	+	+	-	0.50	0.5	0.5	0.5	1.00	1.00	10000.00
5	+	+	-	0.50	0.5	0.5	0.5	1.00	1.00	10000.00
6	-	+	+	239.40	21.9	230.7	23.9	0.04	-0.10	5.28
6	-	+	+	226.70	22.6	220.5	15.9	0.03	0.30	6.60
7	+	-	+	325.10	29.7	312.0	20.8	0.04	0.30	1.21
7	+	-	+	325.20	20.3	310.5	20.3	0.05	0.00	1.06
8	+	+	+	0.50	0.5	0.5	0.5	1.00	1.00	10000.00
8	+	+	+	217.90	17.6	217.2	13.5	0.00	0.23	0.91

Nomenclature:

* That width and height equals to 0.5 denotes that the slurry could not be extruded smoothly, (dotted line was written).

** For dotted line and no line written, the resistance was shown as 100000 MΩ.

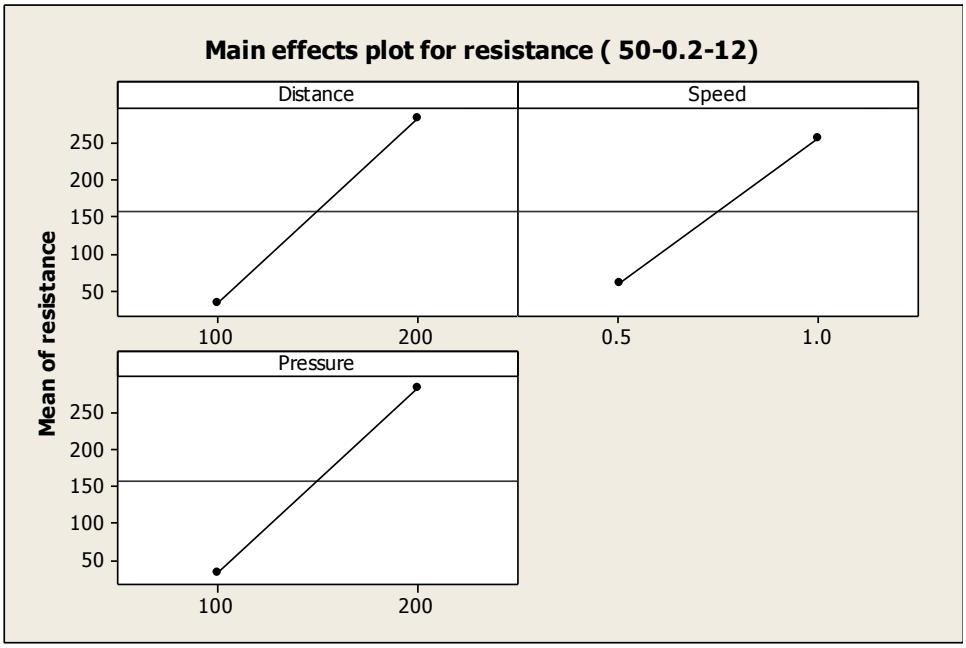

(a)

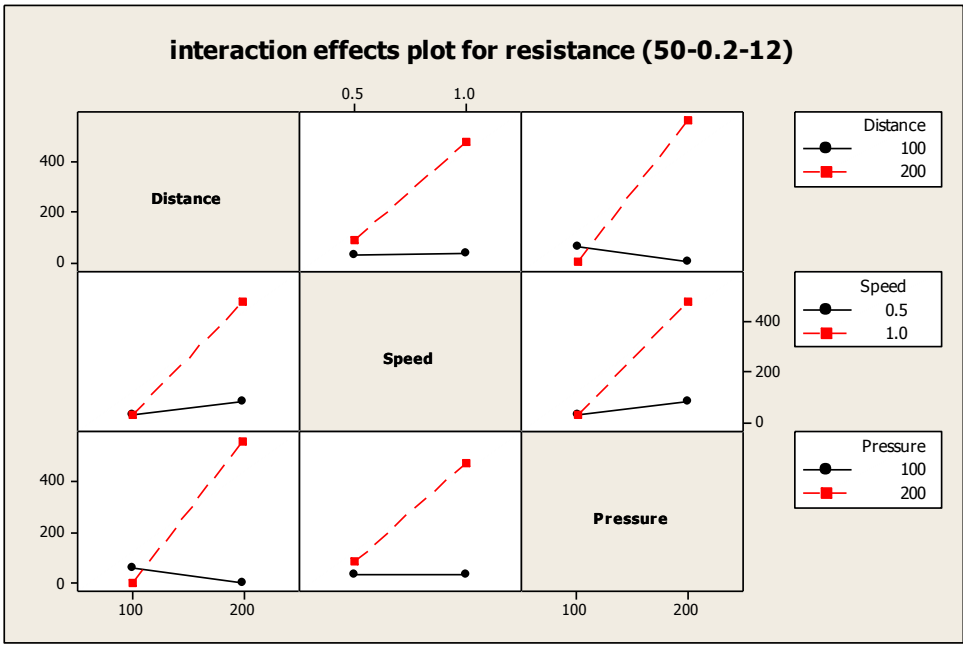

(b)

Figure 7.1. (a) Main effects plot and (b) Interaction effects plot for resistance (50-0.2-12)

Table 7.5. ANOVA table for resistance

Source	DF	Seq SS	Adj SS	Adj MS	F	p
Distance	1	248339	248339	248339	4.68	0.06
Speed	1	153914	153914	153914	2.90	0.13
Pressure	1	249551	249551	249551	4.70	0.06
Distance*Speed	1	148272	148272	148272	2.79	0.13
Distance * Pressure	1	383419	383419	383419	7.22	0.03
Speed*Pressure	1	156298	156298	156298	2.94	0.13
Distance*Speed*Pressure	1	153189	153189	153189	2.89	0.13
Error	8	424671	424671	53084		
Total	15	1917655				
S = 230.399 R-Sq = 77.85% R-Sq(adj) = 58.48%						

Tables 7.6 and 7.7 show the ANOVA results for the shrinkage of width and height. Both the main and interaction effects for width and height shrinkage are insignificant. This indicates that the shrinkages of width and height were not affected by direct writing process parameters significantly. It is implied that the shrinkage of width and height may be affected by other reasons, such as slurry composition and substrate surface properties.

Table 7.6. ANOVA for shrinkage of width

Source	DF	Seq SS	Adj SS	Adj MS	F	P
Distance	1	0.0009	0.0009	0.0009	0.250	0.629
Speed	1	0.0012	0.0012	0.0012	0.340	0.574
Pressure	1	0.0000	0.0000	0.0000	0.010	0.935
Distance*Speed	1	0.0110	0.0110	0.0110	3.090	0.117
Distance * Pressure	1	0.0012	0.0012	0.0012	0.340	0.574
Speed*Pressure	1	0.0004	0.0004	0.0004	0.110	0.746
Distance*Speed*Pressure	1	0.0049	0.0049	0.0049	1.380	0.275
Error	8	0.0285	0.0285	0.0036		
Total	15	0.0482				
S = 0.0596867 R-Sq = 40.87% R-Sq(adj) = 0.00%						

Table 7.7. ANOVA for shrinkage of height

Source	DF	Seq SS	Adj SS	Adj MS	F	P
Distance	1	0.0420	0.0420	0.0420	0.460	0.517
Speed	1	0.1260	0.1260	0.1260	1.380	0.274
Pressure	1	0.0900	0.0900	0.0900	0.990	0.350
Distance*Speed	1	0.0000	0.0000	0.0000	0.000	1.000
Distance * Pressure	1	0.0240	0.0240	0.0240	0.260	0.622
Speed*Pressure	1	0.0600	0.0600	0.0600	0.660	0.441
Distance*Speed*Pressure	1	0.3136	0.3136	0.3136	3.430	0.101
Error	8	0.7308	0.7308	0.0914		
Total	15	1.3865				
S = 0.302242 R-Sq = 47.29% R-Sq(adj) = 1.17%						

Table 7.8 and Table 7.9 show the ANOVA results for effect of different parameters on the width and height of the line after sintering, respectively. Both the main and interaction effects are significant for the width and height after sintering. However, the interaction between speed and pressure is not significant for width after sintering and the interaction between distance and pressure is not significant for height after sintering.

Table 7.8. ANOVA for width after sintering

Source	DF	Seq SS	Adj SS	Adj MS	F	P
Distance	1	91502	91502	91502	82.44	0.000
Speed	1	163020	163020	163020	146.88	0.000
Pressure	1	95730	95730	95730	86.25	0.000
Distance*Speed	1	9522	9522	9522	8.58	0.019
Distance * Pressure	1	1145	1145	1145	1.03	0.400
Speed*Pressure	1	29003	29003	29003	26.13	0.001
Distance*Speed*Pressure	1	44803	44803	44803	40.37	0.000
Error	8	8879	8879	1110		
Total	15	443604				
S = 33.3148 R-Sq = 98.0% R-Sq(adj) = 96.25%						

Table 7.9. ANOVA for height after sintering

Source	DF	Seq SS	Adj SS	Adj MS	F	P
Distance	1	228.98	228.98	228.98	16.69	0.003
Speed	1	227.47	227.47	227.47	16.68	0.004
Pressure	1	272.84	272.84	272.84	20.01	0.002
Distance*Speed	1	280.82	280.82	280.82	20.59	0.002
Distance * Pressure	1	0.05	0.05	0.05	0.00	0.952
Speed*Pressure	1	49.17	49.17	49.17	3.61	0.094
Distance*Speed*Pressure	1	92.89	92.89	92.89	6.81	0.031
Error	8	109.11	109.11	13.64		
Total	15	1261.33				
S = 3.69298 R-Sq = 91.35% R-Sq(adj) = 83.78%						

7.4.3. Evaluation of extrusion pressure, line dimensions and resistance. From section 7.4.2., all of three parameters are significant for the line dimensions. However, pressure and distance are significant for the line resistance. Thus, in this section, the extrusion pressure, line dimensions and resistance are evaluated. The width of the cathode line is dependent on the extrusion pressure when all other direct writing parameters are kept constant. In order to predict the width of the line before sintering, a regression analysis was performed. The pressure and width before sintering had linear relationship. Figure 7.2-left plot shows the scatter plot of them and including the regression line.

The regression analysis width before sinter versus pressure is shown in Table 7.10. Further, to predict the width of the line after sinter, a regression analysis was performed. Pressure and width after sinter had a linear relationship as shown in Figure 7.2. . The regression analysis width before sinter versus pressure is shown in Table 7.11. The

Equation (7.1) and Equation (7.2) are the regression equations for before and after sintering width.

$$\text{Before sintering width } (\mu m) = 393 + 0.988 \text{ pressure(kPa)} \quad (7.1)$$

$$\text{After sintering width } (\mu m) = 358 + 0.955 \text{ pressure(kPa)} \quad (7.2)$$

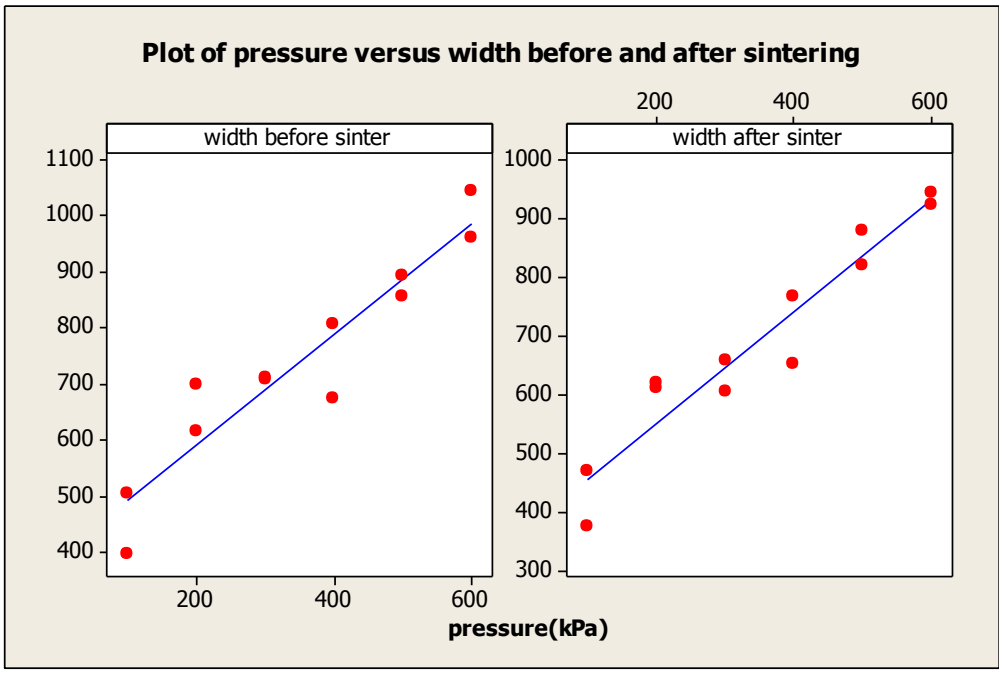

Figure 7.2. Plot of pressure vs. width before & after sintering

Table 7.10. Regression Analysis: width (µm) before sintering vs. pressure (kPa)

Predictor	Coef	SE Coef	T	p
Constant	393.25	42.15	9.33	0
Pressure(kPa)	0.99	0.11	9.13	0
S=64.0232	R-sq=89.30%		R-Sq(adj)= 88.20%	

Table 7.11. Regression Analysis: width (µm) after sintering vs. pressure (kPa)

Predictor	Coef	SE Coef	T	p
constant	358.28	34.48	10.39	0
Pressure(kPa)	0.96	0.09	10.79	0
S=52.3727	R-sq=92.10%		R-Sq(adj)=91.30%	

The plot of height line before and after sintering vs. pressure (Figure7.3), shows a random distribution with respect to the extrusion pressure. Figure 7.4 shows the plot of resistance vs. cross section before & after sintering, the cross section shows random distribution versus resistance. Figure 7.5 shows the plot of pressure vs. cross section before & after sintering, the cross section shows random distribution versus resistance. Figure 7.6 shows the plot of resistance vs. width & height after sintering. An increase in the width results in lower resistance. However, an increase in the height shows random effect on the resistance.

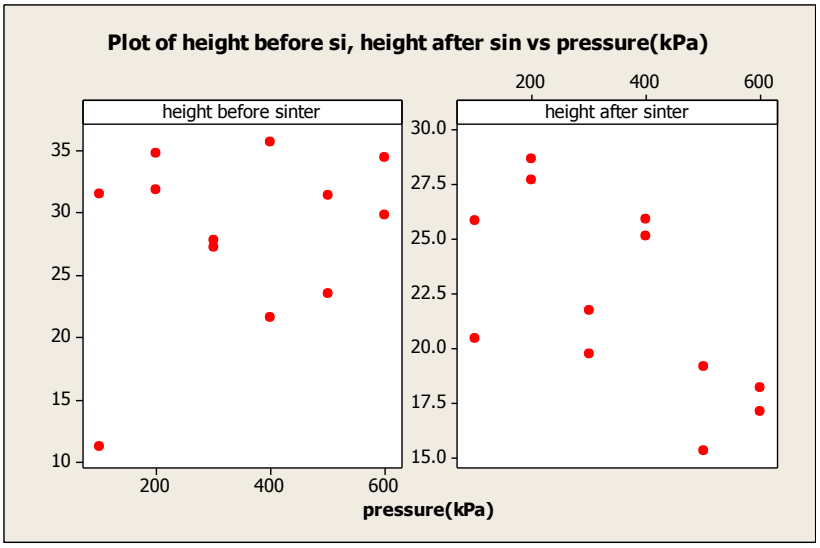

Figure 7.3. Plot of pressure vs. height before & after sintering

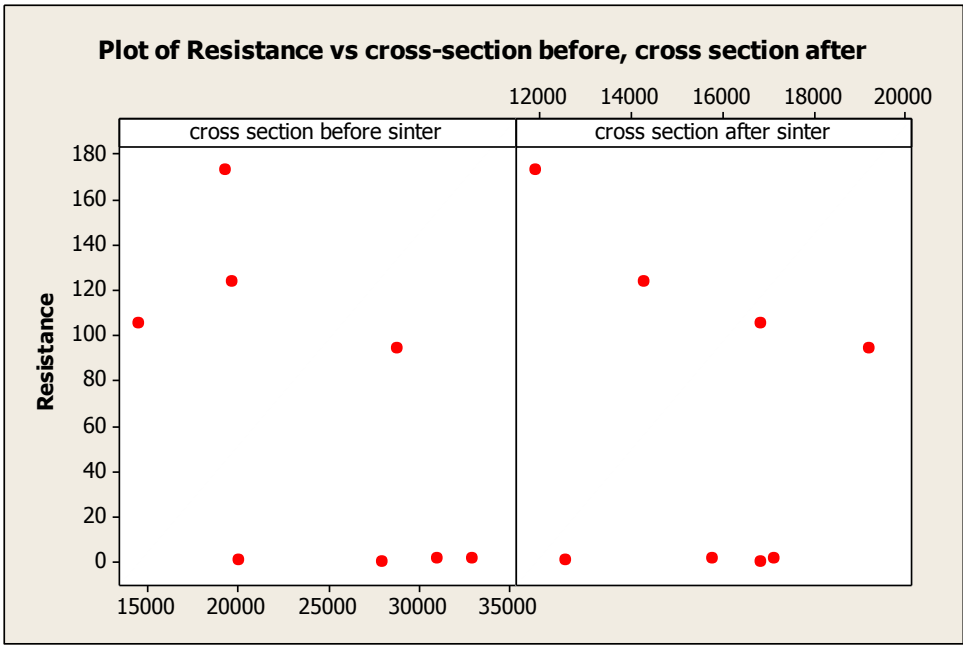

Figure 7.4. Plot of cross section before & after sintering vs. resistance

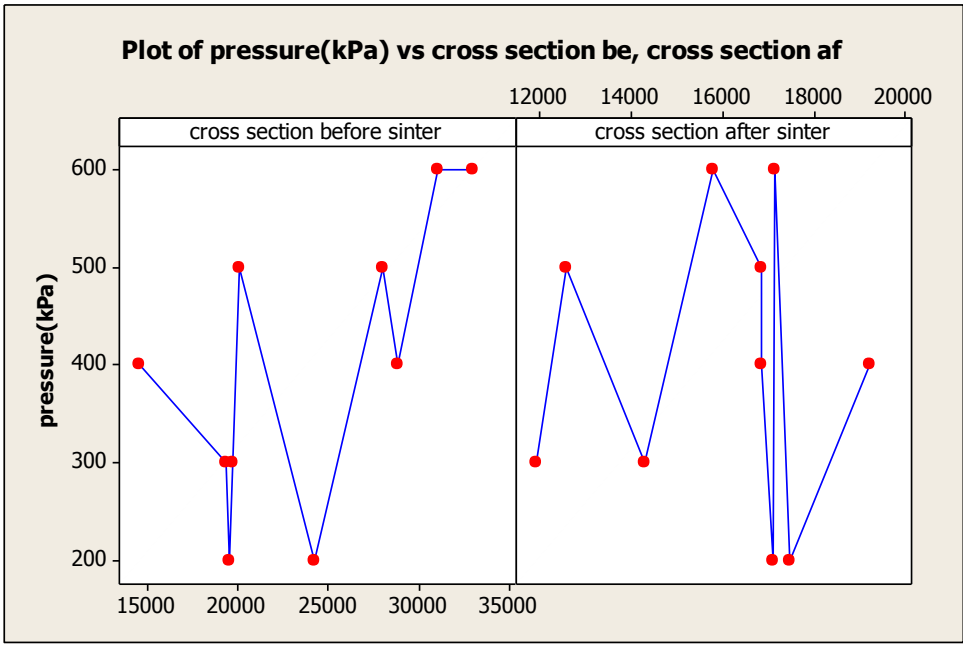

Figure 7.5. Plot of cross section before & after sintering vs. pressure

Figure 7.6. Plot of resistance vs. width & height after sintering

7.5. Conclusion

The microstructure of electrode pattern lines is not only affected by the slurry's composition but also affected by the direct writing process parameters. These process parameters include nozzle size, nozzle speed, distance between the nozzle and substrate, pressure in the slurry chamber, and the diffusion rate of electrolyte substrate.

In this study, the effects of extrusion parameters were evaluated and optimized. A 2^3 (k=3) full factorial experimental design was used to evaluated the parameters of interest. Further, a statistical analysis was used to evaluate their effects on resistance, dimension and shrinkage of dimension. Based on an ANOVA, distance and pressure have significant effect on the resistance of the cathode electrode. A linear regression equation gave relationship between extrusion pressure and line width of the electrodes.

CHAPTER 8

Conclusions

8.1. Research on Fabrication Technologies

In this research, several approaches to fabricate the μ-SC-SOFC were studied and evaluated.

- Electron Beam Lithography

EBL is a reliable technique to create the nano-sized features directly on the substrate. However, the stitching and overlay error were magnified, during the fabrication of micro-size features.

- Soft lithography + Photolithography

This method had very low repeatability. Making the precise PDMS mold was a challenge. In addition, soft lithography is suitable for the low viscosity slurry. Slurry having good fluidity (low viscosity and surface tension) makes it easy to move into the very thin mold channels. However, after sintering, the shrinkage rate was high with crack formations, the crack are difficult to avoid.

- PLD + Photolithography

This approach is a suitable for generating high accuracy features on the substrate. The effects of the deposition pressure, annealing temperature and time on the electrode fabrication need further research. In addition, the optimization of the photolithography process needs further investigation.

- Direct writing

This approach is amenable for the design and rapid fabrication of ceramic materials in complex 3D shapes without the need for expensive tooling, dies or lithographic masks. However, a major limitation of the direct-writing method is the difficulty in reducing the gap between the electrodes to less than 10μm.

- Direct writing + Photolithography

This approach was first proposed in SOFC fabrication field. The approach includes restraining the flow of the slurry by building constraining structures using photolithography that prevent the slurry diffusion in order to improve the accuracy of direct writing approach. Also, using this approach it is possible to deposit multilayer electrodes within a single electrode trace.

8.2. Direct Writing Slurry Rheology Research

Slurries to direct-write the cathode electrodes were evaluated for their respective rheological characteristics.

- Time Period

In the slurry rheology research, the time period for slurry stabilization was measured. The slurry with 60% solid loading was highly viscous and attained a stable reading after 300s. The slurries with 50% and 40% solid loading had lower viscosities as compared to 60% solid loading. These slurries attained stability after 200s.

- Effects of dispersant

To study the effect of dispersant (Triton) on LSCF slurry, different dispersant concentration slurries' were evaluated. Slurries with 60% solid loading had high viscosity. Their behaviors resemble those of Viscoplastic and Bingham fluid, with initial yield stress. Slurries with 50% solid loading have comparative lower viscosity to that of 60% solid loading. However, their fluid behaviors resemble those of psedoplastic and shear thickening fluid. Slurries with 40% solid loading have the lowest viscosity among the candidate slurries. Most of the 40% solid loading slurries display a Newtonian and pseudoplastic fluid behavior.

The optimum concentration of Triton for different slurries is around 0.2-0.4% of the LSCF solid loading. Triton was identified as a good dispersant for the cathode slurries.

8.3. Effects of Solid Loading and Binder Concentrations on Cathode Dimensions, Microstructure and Resistance

The slurries viscosity plays a major role on the cathode electrode dimension. However, viscosity is dependent on the solid loading and binder concentration of the slurry. The effect of slurry solid loading and binder concentration on cathode dimensions, microstructure and resistance was studied.

- Binder removal process

In the initial stages, the binder removal process was studied, since this process has a major impact on the fuel cell microstructure. Around 80% PVB mass loss occurred at 150-200°C; from 200-600°C, the mass loss reduced gradually, after 600°C, the residual mass was constant. These findings were validated by results from Dr. Kim's group [3]. The drying processes of slurry and the LSCF traces on the substrate were evaluated. The

mass loss and heat flux kinetics of the LSCF slurry was different from the pure binder decomposition process. For the decomposition the mass loss was significant at 100-150°C, followed by a secondary stage mass loss around 400°C. Based on the above described slurry decomposition mechanism the sintering profile and resultant microstructure of lines were determined.. The optimized sintering profile was used in further research.

- Solid loading and binder vs. viscosity

Solid loading and binder concentration are major factors that affect the slurry's viscosity. Their increase results in an increase in the slurry viscosity. Especially, for 60% solid loading, the increase in viscosity is significant. Between these two factors, solid loading has more significant effect. However increase in viscosity and the binder concentration, different solid loading results different ratio. It may be affected by slurries' rheological behavior.

- Line dimension vs. solid loading and binder

With an increase in the binder and solid loading concentration, there is a reduction in the line width reduces. Solid loading concentrations affect the written line's width more significantly. However for the slurry's height, the trend is not very stable and clear. For higher viscosity slurries under higher extrusion pressure, an increase of solid loading or binder results in the height reduction. Solid loading affects more significantly. For lower viscosity slurries under lower extrusion pressure, the height of 50% solid loading is less that that of 40% solid loading when their binder concentrations are same.

- Aspect ratio

Aspect ratios are important for direct writing + photolithography method. Based on the experiments, aspect ratio is reduced as the binder concentration increase. But an increase of solid loading doesn't always result of aspect ratio reduction.

- Dimensional shrinkage vs. solid loading and binder

In the combined direct writing + photolithography method, the width and height shrinkage of electrode lines will affect the design of the photolithography mask. Based on ANOVA results for width shrinkage for high solid loading and high extrusion pressure, all of the main and interaction effects are statistically significant on the width shrinkage. The concentration of the binder is the most significant factor. Even though solid loading is more significant for slurry's viscosity, the binder plays an important role on width shrinkage. Besides, solid loading plays more important role on height shrinkage. It implies that when height shrinkage is concerned, solid loading is the major factor. For low viscosity and low extrusion pressure, this conclusion may not be always correct. In this case the pressure and writing parameters will have a significant effect.

- Electrical resistance vs. solid loading and binder

Electrical resistance was evaluated character. Based on the experiments, generally, low solid loading and low binder concentrations had lower resistance. For higher binder concentration, the resistance increased with solid loading concentration. This is an important finding from this research.

- Electrical resistance vs. cross section

A larger cross section results in a lower resistance. The cross section area plays an important role for a slurry with high solid loading. For slurry with lower solid loading and lower binder concentration, the effect from cross section area was marginal.

8.4. Understanding of Direct Writing Process

The microstructure of electrode pattern lines is not only affected by the slurry's concentration ratio but also affected by the extrusion parameters, such as nozzle size, nozzle speed, distance between the nozzle and substrate, pressure in the slurry chamber, and the diffusion rate of electrolyte substrate.

- Resistance vs. Parameters

According to ANOVA results, all of three extrusion parameters are significant for the line electrical resistance. An increase in the distance, speed or pressure of the direct writing process results in the increase of the resistance.

- Shrinkage vs. Parameters

Parameters are insignificant for width and height shrinkage. It implied the shrinkage of width and height may be affected by other reasons, such as substrate surface properties.

- Width before and after sintering vs. pressure

To predict the line width, the regression equations for width before and after sintering versus pressure were obtained. The basic trend is that as the extrusion pressure increased, the width increased.

- Height before and after sintering vs. pressure

Heights are a random distribution with respect to the extrusion pressure.

- Cross section before and after sinter show random distribution versus pressure.
- Cross section before and after sinter show random distribution versus resistance
- Height after sinter vs. resistance

The highest resistances occurred when width after sintered was low but the height after sintered was high, the lowest resistances occurred when height after sinter was low and width after sinter was high.

BIBLIOGRAPHY

[1] Misereor. (2009). Energy is scarce. Retrieved Sep. 1, 2009, from http://www.misereor.org/issues-themes/energy-for-the-poor/energy-is-scarce.html

[2] Ningbo Institute of Material Technology & Engineering (China Acadmy of Sciences). (2009). *High energy efficiency by SOFC single fuel cells*. Retrieved Aug. 5, 2009, from http://www.sofc.com.cn/news/2009051401.html

[3] Baidu. (2009). Green energy. Retrieved Sep. 1, 2009, from http://baike.baidu.com/view/295338.htm

[4] Grove, W. R. (1893). On voltaic series and the combination of gases by platinum. *Philosophical Magazine and Journal of Science, 14*, 127-130.

[5] Bacon, F. T. (1969). Fuel cell, past, present and future. *Electrochimica Acta, 14*, 569-585.

[6] Choi, W. (2004). *New approaches to improve the performance of the PEM based fuel cell power systems.* Unpublished Doctoral Dissertation. Available from ProQuest Dissertations & Theses database., Texas A&M University.

[7] Fuel Cell Today. (2009). Frequently asked questions. Retrieved Sep. 1, 2009, from http://www.fuelcelltoday.com/reference/faq

[8] La O, G. J., In, H. J., Crumlin, E., Barbastathis, G., & Shao-Horn, Y. (2007). Recent advances in microdevices for electrochemical energy conversion and storage. [review]. *International Journal of Energy Research, 31*(31), 548-575.

[9] Wikipedia. (2009). Fuel cell. Retrieved Sep. 1, 2009, from *http://en.wikipedia.org/wiki/Fuel cell*

[10] Mench, M. M. (2008). *Fuel cell engines*. Hoboken, NJ: John Wiley &Sons. Inc.

[11] Koeneman, P. B., Busch-Vishniac, I. J., & Wood, K. L. (1997). Feasibility of micro power supplies for MEMS. *Journal of Microelectromechanical systems, 6*(4), 355-362.

[12] US Department of Energy -- Energy Efficiency and Renewable Energy (EERE). (2009). *Comparison of fuel Cell technologies*. Retrieved Aug. 5, 2009., from http://www.eere.energy.gov/hydrogenandfuelcells/fuelcells/pdfs/fc_comparison_chart.pdf

[13] Singhal, S. C., & Kendall, K. (2003). *High temperature solid oxide fuel cells : fundamentals, design and applications*. Oxford, UK: Elsevier.

[14] Hibino, T., Hashimoto, A., Inoue, T., Tokuno, J., Yoshida, S., & Sano, M. (2000). A low-operating-temperature solid oxide fuel cell in hydrocarbon air mixtures. *Science, 288*(5473), 2031-2033.

[15] Goff, P. L. (2009). Fuel cell. *High Temperature Systems SOFC and MCFC.* Retrieved Sep. 7, 2009, from http://pl.legoff.free.fr/docs/chimie/us/usfcfram.htm

[16] Graziani, M., & Fornasiero, P. (2007). *Renew able resources and renewable energy: A global Challenge.* Boca Raton, FL: Taylor and Francis

[17] Guindet, A. H. a. J. (1997). *The CRC Handbook of Solid State Electrochemistry*. New York CRC Press Inc.

[18] Singhal, S. C. (2000). Advances in solid oxide fuel cell technology. *Solid State Ionics,, 135*, 305-310.

[19] De Guire, E. J. (2003). Solid Oxide Fuel Cells. Retrieved Aug. 10, 2009, from http://www.csa.com/discoveryguides/fuecel/overview.php

[20] Kawamoto, H. (2007). Research and development trends in solid oxide fuel cell materials from the viewpoint of electrolyte-related R&D as key. *Science & Technology Trends, 82*, 10-22.

[21] Van Gool, W. (1965). *Philips Research Report, 20*, 81.

[22] Louis, G. A., Hartford, W., Lee, J. M., Maricle, D. L., & Trocciola, J. C. (1981). US Patent.

[23] Dyer, C. K. (1990). A novel Thin-film electrochemical device for engergy conversionCuo. *Nature, 343*, 547-548.

[24] Hibino, T., & Iwahara, H. (1993). Simplification of solid oxide fuel cell system using partial oxidation of methane. *Chemistry letters, 7*, 1131-1134.

[25] Cavalca, C. A., Larsen, G., Vayenas, C. G., & Haller, G. L. (1993). Electrochemical modification of methanol oxidation selectivity and activity on a platinum single-pellet catalytic reactor. *J. Phys. Chem., 97*(23), 6115-6119.

[26] Riess, I., van der Put, P. J., & Schoonman, J. (1995). Solid oxide fuel cells operating on mixtures of fuel and air. *Solid State Ionics, 82*(1), 1-4.

[27] Jasinski, P. (2008). Micro solid oxide fuel cells and their fabrication methods. *microelectronics internaional, 25*(2), 42-48.

[28] Suzuki, T., Jasinski, P., Petrovsky, V., Anderson, H. U., & Dogan, F. (2005). Performance of a porous electrolyte in single-chamber SOFCs. *Journal of Electrochemical Society, 152*, A527-531.

[29] Yano, M., Tomita, A., Sano, M., & Hibino, T. (2006). Recent advances in single-chamber solid oxide fuel cells: a review. *Solid State Soince, 177*(39-40), 3351-3359.

[30] Napporn, T. W., Morin, F., & Meunier, M. (2004). Evaluation of the actual working temperature of a single chamber SOFC. *Electrochemical and Solid-State Letters, 7*(3), A60-63.

[31] Buergler, B. E., & Gauckler, L. J. (2007). From macro- to micro-single chamber solid oxide fuel cells. *Journal of Power Sources, 171*(2), 310-340.

[32] Ahn, S.-J., Lee, J.-H., Kim, J., & Moon, J. (2006). Single- chamber solid oxide fuel cell with micropatterned interdigitated electrodes. *Electrochemical and Solid-State Letters, 9*(5), 4.

[33] Hoogers, G. (2002). *Fuel Cell Technology Handbook*. Boca Raton,FL: The CRC Press.

[34] Yu, J., Cheng, P., Ma, Z., & Yi, B. (2003). Fabrication of miniature silicon wafer fuel cells with improved performance *Journal of Power Sources, 124*(1), 40-46.

[35] Shaffer, S. (2004). *Development update on Delphi's solid oxide fuel cell system*. Paper presented at the SECA Review Meeting.

[36] Jankowski, A. F., Hayes, J. P., Graff, R. T., & Morse, J. D. (2002). Micro-fabricated thin-film fuel cells for portable power requirements. *Materials research society, 730*, 93-98.

[37] Hahn, R., Wagner, S., Schmitz, A., & Reichl, H. (2004). Development of planar microfuel ell with thin film and micro patterning technologies. *Journal of Power Sources, 131*(1-2), 73-78.

[38] Hibino, T., Ushiki, k., & Kuwahara, Y. (1996). New concept for simplifying SOFC system. *Solid State Ionics, 91*(1-2), 69-75.

[39] Chung, C.-Y., & Chung, Y.-C. (2006). Performance Characteristics of micro single- chamber solid oxide fuel cell: Computational analysis. *Journal of Power Sources, 154*(1), 35-41.

[40] Hibino, T., Hashimoto, A., Inoue, T., Tokuno, J., Yoshida, S., & Sano, M. (2000). Single-Chamber Solid Oxide Fuel Cells at Intermediate Temperatures with

Various Hydrocarbon-Air Mixtures. *Journal of Electrochem. Soc., 147*(8), 2888-2892.

[41] Shao, Z., Mederos, J., Chueh, W. C., & Haile, M. (2006). High power-density single-chamber fuel cells operated on methane. *Journal of Power Sources, 162*(1), 589-596.

[42] Lewis, J. A., Smay, J. E., Stuecker, J., & Cesarano III, J. (2006). Direct Ink Writing of Three-Dimensional Ceramic Structures. [Article]. *Journal of the American Ceramic Society, 89*(12), 3599-3609.

[43] Ahn, S.-J., Kim, Y.-B., Moon, J., Lee, J.-H., & Kim, J. (2006). Co-planar type single chamber solid oxide fuel cell with micro-patterned electrodes. *Journal of Electroceramics, 17*, 689-693.

[44] Lewis, J. A. (1997). Binder removeal from ceramics. *Annual review of material science, 27*(1), 147-174.

[45] Kim, Y., S.Ahn, Moon, J., Kim, J., & Lee, H. (2006). Direct write fabrication of integrated planar solid oxide fuel cells. *Journal of Electroceramics, 17*, 683-687.

[46] Kuhn, M., Napporn, T., Meunier, M., Therriault, D., & Vengallatore, S. (2008). Fabrication and testing of coplanar single_chamber micro solid oxide fuel cells with geometrically complex electrodes. *Journal of Power Sources, 177*(1), 148-153.

[47] Minh, N. Q., & Takahashi, T. (1995). *Science and Technology of Ceramic Fuel Cells.* Amsterdam, The Netherlands: Elsevier.

[48] Beckel, D., Bieberie-Hutter, A., Harvey, A., Infortuna, A., Muecke, U. P., Prestat, M., et al. (2007). Thin films for micro solid oxide fuel cells [review]. *Journal of Power Sources, 173*, 325-344.

[49] Xin, X., Lu, Z., Huang, X., Sha, X., Zhang, Y., Chen, K., et al. (2006). Solid oxide fuel cells with dense yttria-stabilized zirconia electrolyte membranes fabricated by a dry pressing process. *Journal of Power Sources, 160*(2), 1221-1224.

[50] Will J, M. A., Kleinlogel C, Perednis D, Gauckler LJ. (2000). fabrication of thin electrolytes of second generation solid oxide fuel cells *Solid State Ionics, 131*(1-2), 18.

[51] Baertsch, C. D., Jensen, K. F., Hertz, J. L., Tulller, H. L., Vengallatore, S. T., Spearing, S. M., et al. (2004). Fabrication and structural characterizaiton of self-supporting electrolyte membrances for a micro solid oxide fuel cell. *Journal of Materials Research, 19*, 2604-2612.

[52] Hertz, J. L., Lappalainen, J., & Tuller, H. L. (2002). *Progress towards an all thin film fuel cell for portable power generation.* Paper presented at the Materials for fuel cells and fuel processors symposium.

[53] Optics Manufacture. (2009). Fiber optics manufacture. Retrieved Sep. 1, 2009, from http://www.opticsmanufacturing.net/index.php?id=22

[54] Silicon Far East. (2009). Electron Beam Lithography. Retrieved Sep. 1, 2009, from http://www.siliconfareast.com/lith_electron.htm

[55] Whitesides, G. M. (1998). Soft lithography. *Angewandte Chemie International Edition, 37*(5), 550-575.

[56] Rogers, J. A., Paul, K. E., Jackman, R. J., & Whitesides, G. M. (1997). Using an elastomeric phase mask for sub-100 nm photolithography in the optical near field. *Application physic letter, 70*, 2658-2660.

[57] Xia, Y., Kim, E., & Whitesides, G. M. (1996). Micromolding in capillaries: Applications in material science. *Journal American Chemial Society, 118*, 5722-5731.

[58] Kim, E., Xia, Y., & Whitesides, G. M. (1995). Polymer microstructures formed by moulding in capillaries. *Nature, 376*, 581-585.

[59] Zhao, X. M., Xia, Y., & Whitesides, G. M. (1996). Fabrication of three-dimensional micro-structures: Microtransfer molding. *Advance material, 8*, 420-424.

[60] Kumar, A., & Whitesides, G. M. (1993). Features of gold having micrometer to centimeter dimensions can be formed through a combination of stamping with an elastomeric stamp and an alkanethiol ink followed by chemical etching. *Applied Physics Letters, 63*, 2002-2004.

[61] Chou, S. Y., Krauss, P. R., & Renstrom, P. J. (1996). Imprint lithography with 25-nanometer resolution. *Science, 272*, 85-87.

[62] Barron, A. R. (2009). Composition and Photochemical Mechanisms of Photoresists. Retrieved 9/9, 2009, from http://cnx.org/content/m25525/latest/

[63] Pulsed Laser Deposition. (2001). PLD, pulsed laser deposition. Retrieved Sep. 1, 2009, from http://pulsedlaser.net/pld/PLD_schem.jpg

[64] Melanie Kuhn, T. N., Michel Meunier, S. Vengallatore, D. Therriault. Direct-write microfabrication of single -chamber micro solid oxide fuel cells.

[65] Kuhn, M., Napporn, T., Meunier, M., Vengallatore, S., & Therriault, D. (2008). Direct-write microfabrication of single-chamber micro solid oxide fuel cells. *J. Micromech. Microeng., 18*, 015005-015011.

[66] Shared Materials Instrumentation Facility--Duke University. (2009). EBL description. Retrieved Sep. 1, 2009, from http://smif.lab.duke.edu/Description.asp?ID=55

[67] Shared Materials Instrumentation Facility--Duke University. (2009). EBL guidelines. Retrieved Sep. 1, 2009, from http://smif.lab.duke.edu/pdf/EBL%20Guidelines.pdf

[68] Shared Materials Instrumentation Facility--Duke University. (2009). EBL resister processes. Retrieved Sep. 1, 2009, from http://smif.lab.duke.edu/pdf/EBL%20processes.pdf

[69] Futurrex. (2008). Negative resist NR9-8000 Technical information. In Futurrex (Ed.).

[70] Renger, C., Kuschel, P., Kristoffersson, A., Clauss, B., Oppermann, W., & Sigmund, W. (2007). rheology studies on highly filled nano-zirconia suspensions. *Journal of the European Ceramic Society, 27*(6), 2361-2367.

[71] Loh, N. H., Tor, S. B., Tay, B. Y., Murakoshi, Y., & Maeda, R. (2007). Fabrication of micro gear by micro powder injection molding. *Microsystem Technologies, 14*, 43-49.

[72] Cetinel, F. A., Bauer, W., Muller, M., Knitter, R., & Haubelt, J. (2010). Influence of dispersant, storage time and termperature on the rheological properties of zirconia-paraffin feedstocks for LPIM. *Journal of the European Ceramic Society, 30*, 1391-1400.

[73] Tsetsekou, A., Agrafiotis, C., & Milias, A. (2001). Optimization of the rheological properties of alumina slurries for ceramic processing applications Part I: Slip-casting. *Journal of the European Ceramic Society, 21*, 363-372.

[74] Paik, U., Hackley, V. A., & Lee, H.-W. (1999). Dispersant-binder interactions in aqueous silicon nitride suspensions. *Journal of the American Ceramic Society, 82*(4), 833-840.

[75] Zucher, S., & Graule, T. (2005). Influence of dispersant structure on the rheological properties of highly-concentrated zirconia dispersions. *Journal of the European Ceramic Society, 25*(6), 863-873.

[76] Seo, J. J., Kuk, S. T., & Kim, K. (1997). Thermal decomposition of PVB binder in teh matrix and electrolyte of molten carbonate fuel cells. *Journal of Power Sources, 69*(1-2), 61-68.

[77] Brookfield. (2010). Why measure viscosity? Retrieved Sep. 8, 2009, from www.brookfieldenginerring.com/education/viscosity_whymeasure.asp

[78] Subramanian, R. S. (2010). Non-Newtonian Flows. Retrieved May 05, 2010, from http://web2.clarkson.edu/projects/subramanian/ch301/notes/nonnewtonian.pdf

[79] Habdas, P. (2010). Rheology is a study of the change in form and flow of matter, embracing , elasticity, viscosity, and plasticity. Retrieved 07/16, 2010, from http://www.sju.edu/~phabdas/physics/rheo.html

[80] Department of Polymer Science The University of Southern Mississippi. (2009). Dilute solution -viscometry. Retrieved Jun. 1, 2010, from http://pslc.ws/macrog/vis.htm

[81] Signatone. (2009). Pro-4 Four Point Resistivity Systems. Retrieved Sep. 1, 2009, from http://www.signatone.com/applications/pro_4.asp